Department of Physics and Astronomy
Heidelberg University

Master Thesis in Physics
submitted by

Thomas Kerschenbauer

born in Luxembourg (Luxembourg)

2026

Development of 3D-Printed SQUID Sample Holders for Weakly Magnetic Samples and Magnetisation Studies of Fe(I) Sandwich Complexes

This Master Thesis has been carried out by
Thomas Kerschenbauer
at the
Kirchhoff-Institute for Physics
under the supervision of
Prof. Dr. Rüdiger Klingeler

Abstract

Superconducting Quantum Interference Device (SQUID) magnetometry is among the most sensitive techniques for measuring magnetic moments, making it well suited to probe systems with small magnetic moments and weak magnetic interactions. This thesis pursues two objectives that are united by their reliance on SQUID magnetometry. In the first part, three samples containing the Fe(I)-based sandwich complex $[Fe(HMB)_2]^+$, with different counterions, are investigated. Combined SQUID magnetometry and X-band EPR spectroscopy confirm a low-spin $S = 1/2$ ground state for all studied complexes. The magnetometry data indicate a vanishing Weiss temperature for the $[Al(OR^F)_4]^-$ and $[B(Ar^F)_4]^-$ samples, while an antiferromagnetic $\Theta_W = 6.5(7)\,\mathrm{K}$ was found for the $[PF_6]^-$ sample. The stonger magnetic coupling is rationalised by the smaller size of the counterions, which allows for intermolecular magnetic interactions. Moreover, the isothermal magnetisation exhibits plateau-like features that are attributed to geometric magnetic frustration on the triangular Fe(I) lattice. The second part of the thesis presents the development of a custom low-background sample holder for magnetisation measurements in the Quantum Design MPMS3, fabricated by stereolithography (SLA) 3D-printing. The iterative design process results in a compression-based holder with a well reproducible background. Its accuracy is established through validation against different reference samples spanning a broad range of magnetic susceptibilities. The designed sample holder is used for magnetisation measurements on the metal-centred aromaticity candidate sample Re_3Cl_9 and its non-aromatic reference $ReCl_3$. The measurements resolve features in susceptibility ranges that were not yet accessible with conventional sample-mounting techniques, demonstrating the improvement offered by the 3D-printed sample holder.

Kurzzusammenfassung

Die SQUID-Magnetometrie zählt zu den genauesten Methoden zur Messung magnetischer Momente und eignet sich daher insbesondere für die Untersuchung von Systemen mit kleinen magnetischen Momenten und schwachen magnetischen Wechselwirkungen. Diese Arbeit verfolgt zwei Ziele, die beide auf dem Einsatz der SQUID-Magnetometrie beruhen. Im ersten Teil werden drei Proben mit dem Fe(I)-basierten Sandwichkomplex $[Fe(HMB)_2]^+$, mit unterschiedlichen Anionen untersucht. Die Kombination aus SQUID-Magnetometrie und X-Band-EPR-Spektroskopie bestätigt für alle untersuchten Komplexe den Grundzustand mit Spin $S = 1/2$. Die Magnetometriedaten weisen auf eine verschwindende Weiss-Temperatur für die Proben $[Al(OR^F)_4]^-$ und $[B(Ar^F)_4]^-$ hin, während für die $[PF_6]^-$-Probe ein antiferromagnetischer Wert von $\Theta_W = 6.5(7)\,\mathrm{K}$ festgestellt wurde. Die stärkere magnetische Kopplung lässt sich durch die geringere Größe der Anionen erklären, welche intermolekulare magnetische Wechselwirkungen ermöglicht. Darüber hinaus weist die isotherme Magnetisierung plateauartige Merkmale auf, die auf geometrische magnetische Frustration im dreieckigen Fe(I)-Gitter zurückgeführt werden. Der zweite Teil der Arbeit befasst sich mit der Entwicklung eines individuell angefertigten Probenhalters mit geringem Hintergrund für Magnetisierungsmessungen im Quantum Design MPMS3, der mittels SLA-3D-Druck hergestellt wurde. Der iterative Konstruktionsprozess führte zu einem auf Kompression basierenden Probenhalter mit reproduzierbarem Hintergrund. Seine Genauigkeit wurde durch Validierung anhand verschiedener Referenzproben über einen breiten Bereich magnetischer Suszeptibilitäten nachgewiesen. Der entwickelte Probenhalter wird für Magnetisierungsmessungen der metallaromatischen Probe Re_3Cl_9 und deren nicht-aromatischer Referenzprobe $ReCl_3$ verwendet. Die Messungen erfassen Merkmale in Suszeptibilitätsbereichen, die mit herkömmlichen Probenhaltern nicht zugänglich waren, was die Überlegenheit des 3D-gedruckten Probenhalters verdeutlicht.

Contents

1 Introduction **1**

2 Theoretical Background **3**
2.1 Magnetic Response of Matter 3
2.2 Para- and Diamagnetism 5
2.2.1 Paramagnetism 5
2.2.2 Diamagnetism 9
2.3 Magnetic Interactions 11
2.3.1 Interacting Spins 11
2.3.2 Mean-Field Model 11
2.3.3 Curie–Weiss Law 11
2.4 Magnetic Order 13
2.4.1 Spin Chains 13
2.4.2 Magnetic Frustration 13
2.5 Aromaticity and All-Metal Aromaticity 14

3 Experimental Methods **17**
3.1 SQUID Magnetometry 17
3.1.1 Measurement Concept 17
3.1.2 Experimental Setup 19
3.1.3 Data Analysis 23
3.2 X-band EPR Spectroscopy 25
3.2.1 Measurement Concept 25
3.2.2 Experimental Setup 26
3.2.3 Data Analysis 27
3.3 Additive Manufacturing 27
3.3.1 Printing Technology 27
3.3.2 Fabrication and Post-processing 28

4 Probing Distance-Dependent Coupling in Fe(I) Sandwich Complexes **31**
4.1 Overview of Fe(I) Systems 31
4.1.1 Structure and Electronic Configuration 31
4.1.2 Investigated Samples 33
4.1.3 Sample Preparation 34
4.2 $[Fe(HMB)_2][PF_6]$ 35

4.3 $[Fe(HMB)_2][Al(OR^F)_4]$ . . . 41
4.4 $[Fe(HMB)_2][B(Ar^F)_4]$ . . . 43
4.5 Comparative Analysis and Discussion . . . 45

5 Development, Characterisation and Application of Custom Low-Background 3D-Printed Sample Holders 49
5.1 Design Process and Magnetic Characterisation of the Custom Sample Holder . . . 49
5.1.1 Evaluation of Current Options . . . 49
5.1.2 Design Considerations . . . 51
5.1.3 Design Process . . . 53
5.1.4 Comparative Analysis . . . 63
5.2 Numerical Simulation . . . 64
5.3 Experimental Validation . . . 69
5.3.1 Reproducibility of the Background Signal . . . 69
5.3.2 Comparison with Brass Holder and Plastic Capsule . . . 72
5.3.3 Accuracy Assessment Using Reference Samples . . . 74
5.3.4 Comparative Analysis . . . 79
5.4 Diamagnetic Response of Rhenium(III) Chloride Complexes . . . 80
5.4.1 Sample Preparation and Measurement Protocol . . . 81
5.4.2 Isothermal Magnetisation of the Monomer $ReCl_3$ . . . 82
5.4.3 Temperature Dependent Magnetisation of the Monomer $ReCl_3$ 84
5.4.4 Isothermal Magnetisation of the Trimer Re_3Cl_9 . . . 85
5.4.5 Temperature Dependent Magnetisation of the Trimer Re_3Cl_9 . 86
5.4.6 Comparative Analysis . . . 87

6 Conclusion and Outlook 91
6.1 Fe(I) Complexes . . . 91
6.2 Sample Holder Development and Aromaticity . . . 92

A Appendix 95
A.1 Practical Guidelines for Use of the 3D-Printed Sample Holder . . . 95
A.2 Pictures of the 3D-Printed Sample Holder . . . 96
A.3 Detailed Plots of the Reproducability assesment . . . 97

List of Acronyms

AC alternating current

CAD computer-aided design

CASSCF complete active space self-consistent field

CIF Crystallographic Information File

DFB difluorobenzene

DFT density functional theory

DC direct current

EPR Electron Paramagnetic Resonance

ESR Electron Spin Resonance

GGG gadolinium gallium garnet

HOMO highest occupied molecular orbital

IUPAC International Union of Pure and Applied Chemistry

LFS low force stereolithography

MRI magnetic resonance imaging

NMR nuclear magnetic resonance

RMS root-mean-square

SLA stereolithography

SOMO singly occupied molecular orbital

SQUID Superconducting Quantum Interference Device

UV ultraviolet

VSM vibrating sample magnetometry

WCA weakly coordinating anion

XRD x-ray diffraction

1 Introduction

Magnetometry is essential for characterising the magnetic properties of materials, leading to the determination of the electronic structure and magnetic interactions. This makes it indispensable in condensed matter physics. Among the available experimental techniques, superconducting quantum interference device (SQUID) magnetometry proves to be one of the most sensitive methods for measuring magnetic moments, with a moment sensitivity of $10^{-8}\,\mathrm{erg\,G^{-1}}$ [1]. This renders it applicable across a wide range of systems. It offers a sensitive probe of the weak diamagnetic contributions associated with ring-current delocalisation in metal clusters, and is also well suited to examining the exchange interactions and magnetic order in more strongly magnetic systems.

The reliability of the data obtained through SQUID magnetometry depends not only on the performance of the instrument used, but also on the sample preparation and mounting setup. For strongly magnetic samples, the magnetic response of the sample typically dominates any contribution from the sample holder, leading to reliable data without further processing steps. For weakly magnetic samples, however, the sample holder background can become comparable to, or even exceed, the sample signal. In such cases, errors or uncertainties in the background correction process significantly affect the accuracy of the extracted magnetic susceptibility. Consequently, extending SQUID magnetometry to these weakly magnetic samples requires not only careful instrument calibration but also the development of sample holders that combine precise sample positioning, for accurate background subtraction, with a minimal magnetic background.

This thesis addresses two distinct topics that share SQUID magnetometry as the primary experimental technique. The first part concerns the magnetic characterisation of a series of samples containing the same Fe(I) sandwich complex with different anions of varying sizes. Low-valent iron chemistry has attracted sustained interest due to the challenge of stabilising unusual electronic configurations in well-defined coordination environments [2]. The Fe(I) sandwich compound presented in the this part is a rare example of a stabilised Fe(I) oxidation state. It is stabilised by arene ligands and is used to study the dependence of the magnetic interactions of the Fe(I) ions on their spatial separation. To assess this, characterisation by SQUID magnetometry and Electron Paramagnetic Resonance (EPR) spectroscopy was performed.

The second part of this work focuses on the development of a custom low-background sample holder for the Quantum Design MPMS3 SQUID magnetometer. 3D-printing is chosen as the most promising approach due to the geometric flexibility and high precision it provides. This enables accurate control of the magnetic background of the sample holder and precise sample positioning. The developed sample holder is systematically evaluated to determine its magnetic background contribution and measurement reproducibility. The newly developed sample holders is then used to investigate Re_3Cl_9, a system which exhibits all-metal aromaticity [3]. To achieve this, measurements and analyses are performed on this trinuclear compound and its mononuclear analogue, $ReCl_3$, which is used as a reference. The presence of a ring current in Re_3Cl_9 would manifest as enhanced diamagnetic susceptibility relative to $ReCl_3$. As the sample is only weakly magnetic, these measurements demonstrate the effectiveness of the 3D-printed, low-background sample holder and the associated background correction procedure.

2 Theoretical Background

Magnetometry measures the total magnetic moment of a system, which arises from several microscopic contributions. The magnetisation reflects contributions from both spin and orbital angular momentum, modified by spin–orbit coupling and by exchange interactions between magnetic moments. These give rise to the characteristic temperature and field dependence of the material, which often deviates from simple idealised behaviour. Interpreting this dependence requires the models of the electronic structure and magnetic interactions introduced in the following sections.

2.1 Magnetic Response of Matter

Magnetic susceptibility is one of the first properties measured on a newly synthesised material, since it reflects the electronic structure of a sample directly [4]. SQUID magnetometry is sensitive enough to measure not only paramagnetic moments but also the much weaker diamagnetic and weakly paramagnetic responses relevant to this work. Bulk susceptibility alone, however, averages over all magnetic centres. EPR spectroscopy resolves the properties of the individual unpaired electrons, which are obscured by this averaging.

At the microscopic level, magnetism originates from the angular momentum of electrons, with both spin and orbital contributions. These moments are conveniently expressed in units of the Bohr magneton

$$\mu_B = \frac{e\hbar}{2m_e} = 9.274 \times 10^{-21}\,\mathrm{erg\,G^{-1}}, \tag{2.1}$$

which sets the natural scale for atomic magnetic moments, with e denoting the elementary charge, $\hbar$ the reduced Planck constant, and m_e the electron mass. The spin and orbital contributions to the electron's magnetic moment are given by

$$\boldsymbol{\mu}_s = -g_s \mu_B \frac{\mathbf{S}}{\hbar}, \tag{2.2}$$

$$\boldsymbol{\mu}_l = -\mu_B \frac{\mathbf{L}}{\hbar}, \tag{2.3}$$

where $g_s \approx 2$ is the electron g-factor and $\mathbf{S}$, $\mathbf{L}$ are the spin and orbital angular momenta, respectively. The total magnetic moment is the sum of both contributions

$$\boldsymbol{\mu} = \boldsymbol{\mu}_s + \boldsymbol{\mu}_l = -\mu_B \left(g_s \frac{\mathbf{S}}{\hbar} + \frac{\mathbf{L}}{\hbar} \right). \tag{2.4}$$

In systems where spin–orbit coupling is present, $\mathbf{S}$ and $\mathbf{L}$ are no longer conserved individually, rendering the total angular momentum $\mathbf{J} = \mathbf{L} + \mathbf{S}$, with the corresponding quantum number J, a conserved quantity. The magnetic moment can then be expressed as

$$\boldsymbol{\mu} = -g_J \mu_B \frac{\mathbf{J}}{\hbar} \quad \text{with} \quad g_J = 1 + \frac{J(J+1) + S(S+1) - L(L+1)}{2J(J+1)}, \tag{2.5}$$

where the Landé g-factor g_J encodes the relative spin and orbital contributions with respect to the spin–orbit coupling. Under the influence of a ligand environment, the orbital angular momentum of the d electrons may be partially or fully quenched by the electrostatic crystal field, reducing their contribution to $\mathbf{J}$. This approximation breaks down for heavier transition-metal ions, for which spin–orbit coupling is significant and both orbital and spin degrees of freedom must be considered when analysing the magnetic behaviour of the system.

From an experimental perspective, SQUID magnetometry measures the macroscopic magnetic moment of an ensemble of spins, captured by the magnetisation

$$\mathbf{M} = \frac{1}{V} \sum_i \boldsymbol{\mu}_i, \tag{2.6}$$

being the total magnetic moment per unit volume V, where $\boldsymbol{\mu}_i$ are the individual magnetic moments in the system. The magnetic susceptibility χ, which quantifies how the magnetisation responds to the applied field, is defined as

$$\chi = \frac{\partial M}{\partial H}, \tag{2.7}$$

where M and H are the projections of $\mathbf{M}$ and $\mathbf{H}$ onto the applied field direction. This relation is the general differential magnetic susceptibility. In systems where the magnetisation depends linearly on the applied field, Equation (2.7) simplifies to

$$\chi = \frac{M}{H}. \tag{2.8}$$

A positive magnetic susceptibility is exhibited by paramagnetic materials, which enhances the applied magnetic field inside the material. In contrast, a negative magnetic susceptibility corresponds to diamagnetism, where the induced magnetic response opposes and, thereby, reduces the internal magnetic field.

2.2 Para- and Diamagnetism

The magnetic response of materials is generally described in terms of paramagnetic and diamagnetic contributions. These determine the behaviour observed in field- and temperature-dependent magnetisation, as measured by SQUID magnetometers.

2.2.1 Paramagnetism

Paramagnetism arises from unpaired electrons whose magnetic moments tend to align with an applied external magnetic field. This leads to a characteristic dependence of the magnetisation on both field and temperature.

Zeeman effect

At a microscopic level, the coupling between magnetic moments and an external magnetic field is known as the Zeeman effect. This is defined as the splitting of magnetic energy levels by the applied field. For paired electrons, these contributions cancel each other. However, for unpaired electron spins, the field-induced splitting of the energy levels results in a net difference in the populations of the Zeeman-split levels. In a magnetic field $\mathbf{B}$, a magnetic moment $\boldsymbol{\mu}$ experiences an interaction energy

$$E = -\boldsymbol{\mu} \cdot \mathbf{B}. \tag{2.9}$$

For an isolated paramagnetic centre, this leads to a lifting of the degeneracy of the magnetic sublevels characterised by the quantum number m_J. Using Equation (2.5), this results in a splitting of the energy levels along the quantisation axis given by

$$E_m = g_J \mu_B B \, m_J, \tag{2.10}$$

where B denotes the magnitude of the magnetic field. Transitions between energy levels split by the Zeeman effect form the basis of electron paramagnetic resonance spectroscopy.

Brillouin Function

The field and temperature dependence of the magnetisation for an ideal paramagnet, consisting of non-interacting, localised magnetic moments, follows from Equation (2.10) combined with a thermal Boltzmann population of the resulting sublevels. The magnetisation is then expressed as

$$M = N g \mu_B J \, B_J(x), \tag{2.11}$$

where N is the number of magnetic ions and $B_J(x)$ is the Brillouin function. The argument

$$x = \frac{g_J \mu_B J B}{k_B T} \tag{2.12}$$

quantifies the ratio of Zeeman energy to thermal energy and, therefore, governs the degree of magnetic-moment-alignment in an external field. $B_J(x)$ characterises the gradual alignment of magnetic moments with varying field strength or temperature. In the limit of weak fields or high temperatures, where $x \ll 1$, the Brillouin function reduces to $B_J(x) \sim x$, such that the magnetisation varies linearly in field and inversely with temperature, yielding the $M \sim B/T$ dependence characteristic of the Curie law. In contrast, for $x \gg 1$, the magnetic moments approach full alignment with the field, leading to saturation of the magnetisation at

$$M_{\text{sat}} = N g_J \mu_B J. \tag{2.13}$$

This also shows that larger values of J lead to a higher saturation magnetisation. The dependence of the Brillouin function on J, is illustrated in Figure 2.1.Larger values of J lead to a slower approach to saturation as a function of the applied magnetic field. In contrast, systems with small J saturate more rapidly. The temperature dependence enters solely through the ratio B/T, such that magnetisation curves measured at different temperatures collapse onto a universal curve when plotted as a function of B/T, provided the system is well described by non-interacting moments. Deviations from ideal Brillouin behaviour are particularly interesting, as this can indicate the presence of magnetic interactions, anisotropy or crystal-field effects.

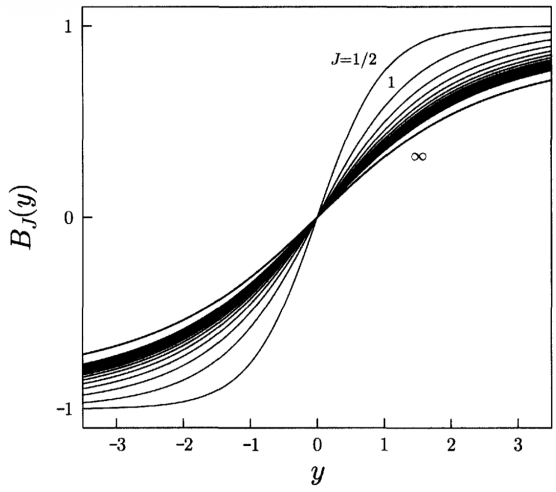


Figure 2.1: Magnetisation of an ensemble of non-interacting paramagnets as described by the Brillouin function for different total angular momentum quantum numbers J. Taken from [5].

Curie Law

In the high-temperature, low-field limit, i.e. $x \ll 1$, the magnetic moments are not strongly aligned, and the Brillouin function reduces to $B_J(x) \sim x$, yielding $M \sim B/T$ since $x \sim B/T$. In this regime, the magnetic susceptibility of an ideal paramagnet behaves according to the Curie law

$$\chi = \frac{C}{T}, \tag{2.14}$$

where C is the Curie constant, defined as

$$C = \frac{N\mu_B^2 g_J^2 J(J+1)}{3k_B}. \tag{2.15}$$

This behaviour arises because thermal fluctuations continuously randomise the orientations of non-interacting magnetic moments, such that the net magnetisation is determined by the competition between field-induced alignment and thermal disorder. With increasing temperature, thermal fluctuations randomise the moment orientations, reducing the net magnetisation induced by the external field. The Curie constant is directly related to the mean-square magnetic moment of the paramagnetic centres and can be expressed in terms of the effective magnetic moment μ_{eff} as

$$\mu_{\text{eff}} = \sqrt{\frac{3k_B C}{N_A}} \quad \text{(in units of } \mu_B\text{)}. \tag{2.16}$$

For ions with well-defined total angular momentum J, the effective moment can be written as

$$\mu_{\text{eff}} = g_J \sqrt{J(J+1)}\, \mu_B. \tag{2.17}$$

Combining the Curie law (Equation (2.14)) with the definition of μ_{eff} yields

$$\mu_{\text{eff}} = \sqrt{\frac{3k_B \chi T}{N_A}}, \tag{2.18}$$

which is particularly useful for analysing experimental magnetic susceptibility data in the high-temperature, low-field limit.

The temperature dependence of χ in the limit of $x \ll 1$, i.e. Equation 2.14, is shown in Figure 2.2. Plotted as $\chi(T)$ (Figure 2.2(a)), χ follows a hyperbolic decrease with increasing temperature. Plotting $1/\chi$ as a function of T (Figure 2.2(b)) yields a linear relationship, which is commonly used to extract the Curie constant from experimental data. The product χT (Figure 2.2(c)) remains constant in the high-temperature, low-field limit, providing a convenient criterion for identifying deviations from Curie behaviour.

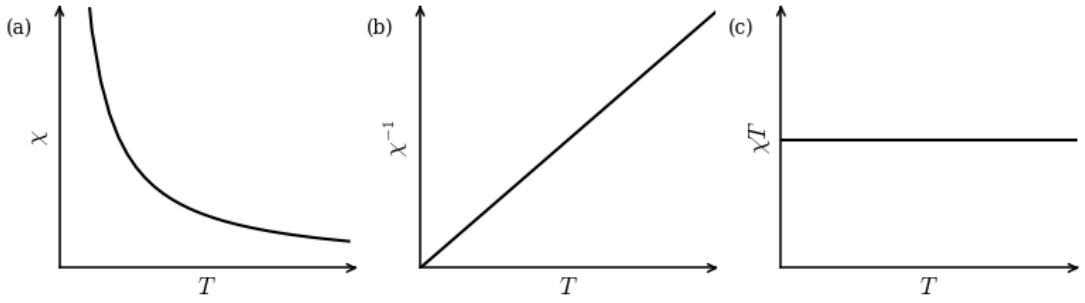


Figure 2.2: Temperature dependence of the susceptibility of an ensemble of non-interacting paramagnets described by the Curie law, shown as (a) χ vs. T, (b) $1/\chi$ vs. T, and (c) χT vs. T. Adapted from [5].

Van Vleck Paramagnetism

Another contribution to the magnetic susceptibility originates from mixing of the ground state with excited states induced by the Zeeman interaction, resulting in a temperature-independent paramagnetic contribution. This mechanism, known as Van Vleck paramagnetism, is described within second-order perturbation theory and contributes an additive, field-independent term χ_{VV} to the magnetic susceptibility. Provided that the population of excited states is negligible, this contribution remains temperature independent.

Van Vleck paramagnetism is particularly significant in systems with a weakly or non-magnetic electronic ground state and low-lying excited states of different symmetry or spin multiplicity. Examples of such systems are second- and third-row transition metal complexes. Strong spin–orbit coupling and large crystal field splittings in these systems can produce a non-magnetic singlet ground state with excited states at moderate energies [6]. In such cases, the Van Vleck contribution may constitute the dominant or even sole paramagnetic response of the system at low temperatures, and its inclusion is essential for a physically meaningful analysis of the measured magnetic susceptibility data [5]. In practice, χ_{VV} is incorporated into the total susceptibility χ as a temperature-independent offset,

$$\chi = \chi_{CW}(T) + \chi_{VV} + \chi_0, \tag{2.19}$$

where $\chi_{CW}(T)$ is the Curie–Weiss susceptibilty, which is discussed in Section 2.3.3, and χ_0 collects any remaining temperature-independent contributions, such as the diamagnetic corrections discussed in the following. The separation of χ_{VV} from χ_0 in experimental data is not trivial and typically requires a reliable theoretical estimate of the energy splitting between the ground state and low-lying excited states.

2.2.2 Diamagnetism

Whereas paramagnetism is associated with unpaired electrons, diamagnetism arises from the field-induced orbital precession of all electrons around the nucleus. Diamagnetism is defined by a weak, temperature-independent negative magnetic susceptibility that contributes a universal background to magnetic measurements. In some systems, delocalised orbitals can support ring currents that enhance the diamagnetic response. The experimentally measured molar magnetic susceptibility χ_{ex} can be expressed as the sum of the magnetic contributions

$$\chi_{\text{ex}} = \chi_P + \chi_D, \tag{2.20}$$

where χ_P denotes the paramagnetic contribution and χ_D is the negative, temperature-independent diamagnetic contribution [7]. In practice, χ_D arises from all electrons within a system and cannot be decomposed exactly into independent contributions. However, it can be approximated using semi-empirical formulas originally introduced by Pascal and were further developed in classical magnetochemistry [8].

Order-of-Magnitude Estimate

As an initial estimate, the diamagnetic susceptibility of a molecular system can be approximated from its molecular weight M_W as [9]

$$\chi_D \approx -\frac{M_W}{2} \times 10^{-6}\,\text{erg G}^{-2}\,\text{mol}^{-1}. \tag{2.21}$$

This relation provides only an order-of-magnitude estimate, which is primarily useful to quickly check experimental values. The overall accuracy of this estimate does not depend an the absolute strength of the diamagnetic response but for weakly paramagnetic systems the relative error in χ_D translates into increasingly significant uncertainties.

Pascal's Constants

For a quantitative analysis, diamagnetic corrections must instead be determined using tabulated Pascal constants, which account for atomic and bond-type contributions to the molecular susceptibility.

A more accurate approach to determine χ_D is the additive scheme introduced by Pascal [7], in which the diamagnetic susceptibility is expressed as

$$\chi_D = \sum_i \chi_{D,i} + \sum_j \lambda_j, \tag{2.22}$$

where $\chi_{D,i}$ are the individual atomic contributions and λ_j are constitutive corrections accounting for bonding effects, including multiple bonds and aromatic π-delocalisation.

An oveview of the Pascal constants and calculated diamagnetic susceptibilities of the compounds analysed in this thesis is shown in Table 2.1. To leading order, the diamagnetic contribution to the magnetic susceptibility scales with the number of electrons and the spatial extent of their occupied orbitals, which justifies the transferability of atomic contributions between different molecules. Deviations arise from differences in bonding and electronic structure effects, which are empirically captured by the constitutive correction terms.

Table 2.1: Pascal's constants and representative diamagnetic susceptibilities of the compounds analysed in this thesis. Adapted from [7].

Contribution	χ_D $(10^{-6}\,\mathrm{erg\,G^{-2}\,mol^{-1}})$
Atomic Pascal Constants $\chi_{D,i}$	
Carbon (C)	-6.0
Hydrogen (H)	-2.9
Chlorine (Cl)	-23.0
Rhenium (Re)	-30.0
Constitutive Corrections λ	
C=C double bond	-1.7
C≡C triple bond	-2.6
Aromatic ring (π-delocalisation)	-6.0 to -10.0
Molecular Diamagnetic Susceptibility χ_D	
Naphthalene ($C_{10}H_8$)	-83.4
Anthracene ($C_{14}H_{10}$)	-113.3
Rhenium(III) chloride monomer ($ReCl_3$)	-99.0
Rhenium(III) chloride trimer (Re_3Cl_9)	-297.0

Pascal's constants provide a reliable estimate of the diamagnetic contribution to the magnetic susceptibility for a wide range of compounds and represent the standard approach in magnetochemical analysis [7, 8]. However, they remain empirical parameters, and deviations from these susceptibilities can occur in systems with strong electron delocalisation, heavy elements, or non-standard bonding environments. This deviation becomes particularly relevant when χ_P and χ_D are of comparable magnitude. In this case, even small systematic errors in the estimated diamagnetic contribution may significantly affect the extracted paramagnetic susceptibility [7]. In such cases, an experimental determination of the diamagnetic susceptibility using an appropriate reference compound is the most reliable approach.

From an experimental perspective, an accurate determination of the diamagnetic contribution to the magnetic susceptibility is particularly important in SQUID measurements, where small systematic offsets can dominate the signal of weakly paramagnetic samples [10].

2.3 Magnetic Interactions

The preceding discussion assumed that magnetic moments were non-interacting. In real systems, however, magnetic interactions are often present, which modify the magnetic response. This leads to deviations from ideal behaviour, which is most clearly observable in the temperature dependence of the magnetic susceptibility. These interactions can be broadly classified as either ferromagnetic, favouring the parallel alignment of moments, or antiferromagnetic, favouring the antiparallel alignment of moments.

2.3.1 Interacting Spins

The dominant mechanism responsible for the magnetic interaction of localised spins is known as the exchange interaction. It results from the combined effects of Coulomb repulsion and the Pauli exclusion principle. The strength and nature of the exchange interaction is determined by the sign and value of the coupling constant J. A positive value ($J > 0$) favours parallel alignment of the spins and therefore ferromagnetic order, while a negative value ($J < 0$) favours antiparallel alignment and therefore antiferromagnetism.

2.3.2 Mean-Field Model

A practical approach to address an ensemble of interacting spins is the mean-field approximation. This substitutes the individual effects of all neighbouring magnetic moments by an effective molecular field $\mathbf{B}_{\mathrm{MF}} = \lambda\mathbf{M}$, described by the macroscopic magnetisation $\mathbf{M}$ and the Weiss constant λ. With the external magnetic field $\mathbf{B}$ taken into account, each moment then experiences an effective field

$$\mathbf{B}_{\mathrm{eff}} = \mathbf{B} + \lambda\mathbf{M}. \tag{2.23}$$

2.3.3 Curie–Weiss Law

The Curie–Weiss law accounts for magnetic exchange interactions based on the mean-field approximation. These interactions modify the temperature dependence of the

magnetic susceptibility paramagnetic moments, which is shown in Figure 2.3(a). The resulting magnetic susceptibility is given by

$$\chi = \frac{C}{T - \Theta}, \tag{2.24}$$

which is valid for $T > \Theta$, where the Weiss temperature Θ is the weighted sum of all magnetic couplings in the system, with its sign and magnitude reflecting the dominant interaction type and overall coupling strength. Positive values of Θ indicate predominantly ferromagnetic interactions, leading to an enhanced susceptibility upon cooling, while negative values correspond to predominantly antiferromagnetic interactions, which suppress the magnetic response at low temperatures (Figure 2.3). To extract the parameters C and Θ, the Curie–Weiss law is typically analysed by plotting the inverse magnetic susceptibility $1/\chi$ (Figure 2.3(b)). In this representation, $1/\chi$ varies linearly with temperature, allowing C (slope) and Θ (T-axis intercept) to be easily determined. In practice, this linear behavior, i.e. the whole validity of Equation (2.14), is only observed at sufficiently high temperatures, where thermal fluctuations dominate over both the field-induced alignment and intersite exchange interactions. Additionally, the product χT (Figure 2.3(c)) provides a complementary perspective. It approaches a constant value at high temperatures and deviates upon cooling depending on the sign of Θ. For predominantly ferromagnetic interactions, χT increases towards low temperatures, while decreasing for antiferromagnetic interactions.

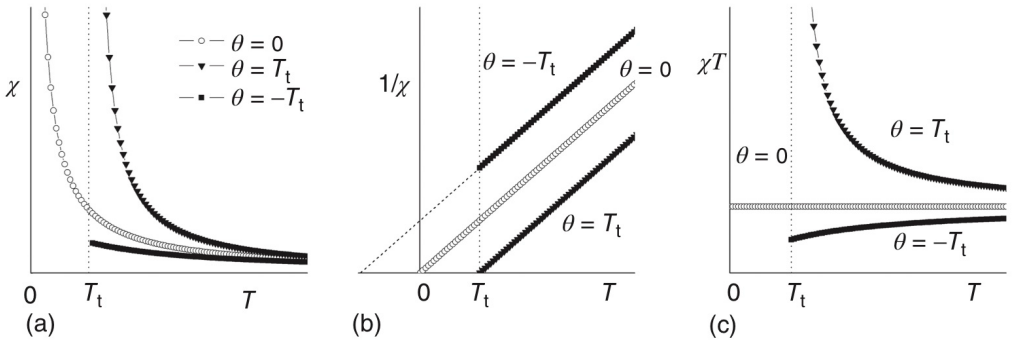


Figure 2.3: Temperature dependence of the magnetic susceptibility of an ensemble of interacting magnetic moments according to the Curie–Weiss law (Equation (2.24)) represented as (a) magnetic susceptibility χ, (b) reciprocal susceptibility $1/\chi$, (c) susceptibility–temperature product χT. Taken from [11].

2.4 Magnetic Order

A magnetic system that is stabilised by exchange interactions and exhibits coherent order throughout below a specific temperature is considered to have long-range order. For ferromagnets, this temperature is known as the Curie temperature (T_C), while for antiferromagnets it is known as the Néel temperature (T_N). If long-range order is obstructed by the geometry of the interactions or the dimensionality of the magnetic lattice, other distinct phenomena can occur. Two examples that are especially important for this thesis are discussed in the following sections.

2.4.1 Spin Chains

When the exchange interactions of a system are anisotropic, the effective dimensionality of the magnetic lattice can be reduced below that of the crystal structure. In the case where interactions along one crystallographic direction significantly exceed those in the the other directions, the system behaves as a collection of weakly coupled spin chains. This leads to the magnetic correlations developing predominantly along the chain direction. As a result quantum fluctuations are strongly enhanced, which suppresses the formation of long-range magnetic order [12].

The reduced dimensionality of the spin chains leads to distinct experimental signatures in the magnetic response. The magnetic susceptibility deviates from a Curie–Weiss behaviour (Equation (2.24)) well above the ordering temperature and often exhibits a broad maximum at temperatures where intra-chain correlations are strong but long-range order has not yet been established [13]. This broad maximum reflects the gradual development of short-range antiferromagnetic correlations along the chains, where spins become increasingly correlated upon cooling but these correlations remain one-dimensional and do not immediately lead to long-range ordering.

2.4.2 Magnetic Frustration

Certain lattice geometries prevent the simultaneous satisfaction of all magnetic interactions. This phenomenon is known as geometric magnetic frustration. This effect is clearly illustrated by considering three spins with $S = 1/2$ arranged on a triangle with antiferromagnetic coupling between each pair. While two spins can easily adopt the antiparallel configuration to minimise their interaction energy, the third spin cannot simultaneously be antiparallel to both of its neighbours. Therefore there is no configuration that fully satisfies all interactions and the system is, therefore, geometrically frustrated. This situation, illustrated schematically in Figure 2.4, gives rise to a large number of degenerate ground states.

In general, frustration arises if the topology of the magnetic lattice is incompatible with the preferred spin alignment. Examples of this are triangular, kagomé, and

pyrochlore lattices. These have geometries that inherently produce frustration for antiferromagnetically coupled moments [14]. A useful quantitative measure of frustration is the frustration parameter

$$f = \frac{|\Theta|}{T_N}, \tag{2.25}$$

where Θ is the Weiss temperature obtained from a Curie–Weiss analysis at sufficiently high temperatures, and T_N is the magnetic ordering temperature. In an unfrustrated system, the ordering temperature is comparable to the interaction strength, and $f \approx 1$. In frustrated systems, the competing magnetic interactions suppress the long-range magnetic order to temperatures well below $|\Theta|$, or prevent it entirely, such that $T_N < |\Theta|$. This leads to a frustration parameter of $f > 1$, with values of $f > 10$ commonly taken as indication of strong frustration [14].

The experimental signatures of magnetic frustration are the suppression of long-range magnetic order and via characteristic anomalies in $M(B)$ measurements. Geometrically frustrated systems have highly degenerate ground states, which significantly enhance quantum fluctuations. This leads to magnetisation plateaus at fractional values of the saturation moment M_sat (Equation (2.13)) [14].

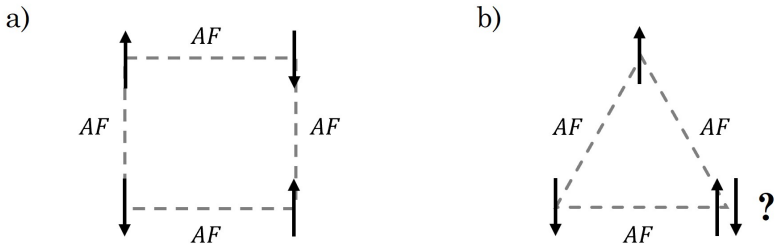


Figure 2.4: Schematic illustration of antiferromagnetically coupled spins on an unfrustrated square lattice (a) and a geometrically frustrated triangular lattice (b). Adapted from [5].

2.5 Aromaticity and All-Metal Aromaticity

Aromaticity describes the stabilisation of cyclic electronic systems due to electron delocalisation, formally defined by the International Union of Pure and Applied Chemistry (IUPAC) as "the enhanced thermodynamic stability [of cyclic molecular systems] relative to acyclic structural analogues" [15]. In its original formulation, aromaticity is defined for planar, cyclic π-conjugated molecules satisfying Hückel's rule, which states that systems with $4n + 2$ π-electrons exhibit enhanced thermodynamic stability and delocalisation [16]. However, this criterion that makes predictions from solely

the number of electrons is insufficient for a full characterisation of aromaticity, as aromaticity arises from the collective electronic structure of the system rather than electron count alone [17]. More generally, aromaticity leads to the lowering of the total energy of the system through delocalisation and also shows structural features such as bond length equalisation and increased rigidity.

This concept extends beyond organic molecules, providing a general description of cyclic delocalisation across various molecular systems. All-metal aromaticity is defined as the cyclic delocalisation of electrons across purely metallic clusters, giving rise to aromatic stabilisation analogous to that in organic systems but also involving σ-, and δ-bond interactions rather than only π-bonds [18, 19]. The aromaticity of metal clusters depends on the geometry, electron count, and chemical stabilisation. These systems are primarily identified as aromatic based on electronic structure analysis and magnetic behaviour. Additionally, current density analysis is frequently employed to predict aromatic character in candidate metallic clusters [20, 21, 22, 23].

The magnetic response is the clearest and most widely used indicator of aromaticity. Aromatic systems exhibit enhanced diamagnetism, since cyclic electron motion generates diatropic ring-currents [17]. These currents induce a magnetic field opposing the applied field, as shown in Figure 2.5. Experimental techniques such as magnetic susceptibility measurements and nuclear magnetic resonance (NMR) spectroscopy offer practical methods for assessing aromaticity. While NMR spectroscopy is among the most widely applied approaches in all-metal aromaticity research [18, 21, 23, 24], magnetic susceptibility measurements represent the approach adopted in this thesis.

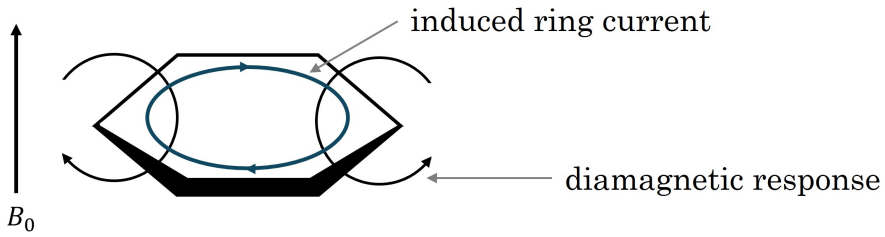


Figure 2.5: Schematic illustration of an induced ring current in an aromatic system in the presence of an applied magnetic field B_0. The applied field induces a circulation of π-electrons around the ring, resulting in a diamagnetic response. Adapted from [25].

3 Experimental Methods

3.1 SQUID Magnetometry

All magnetisation measurements in this thesis were performed using a Quantum Design Magnetic Property Measurement System (MPMS3, Quantum Design Inc.), which is a Superconducting Quantum Interference Device-based magnetometer that enables the determination of macroscopic magnetic moments with high precision. This instrument contains a highly sensitive superconducting detection circuit, a superconducting magnet, and a precise sample transport system while operating in an automated cryogenic environment.

3.1.1 Measurement Concept

The MPMS3 operates by converting the variation in magnetic flux through the detection coils into an electrical signal using a dc-SQUID. The dc-SQUID combines the discoveries of flux quantisation and Josephson tunneling by incorporating them into an exceptionally sensitive sensor capable of detecting magnetic moments on the order of $1 \times 10^{-8}\,\mathrm{erg\,G^{-1}}$ [1]. The basic working mechanism of a dc-SQUID is briefly introduced in the remainder of this section.

To understand the operation principle of a SQUID, it is first necessary to consider the quantisation of magnetic flux in a superconducting loop. The enclosed flux is quantised in units of the flux quantum

$$\Phi_0 = \frac{h}{2e}, \tag{3.1}$$

where h is Planck's constant. In the absence of applied magnetic fields or currents, the phase ϕ of the macroscopic wave function Ψ in the superconducting loop,

$$\Psi(\mathbf{r}) = |\Psi(\mathbf{r})|e^{i\phi(\mathbf{r})}, \tag{3.2}$$

is spatially uniform. However, in the presence of a magnetic flux penetrating the loop, the phase undergoes continuous evolution along the loop with

$$\oint \nabla\phi \cdot d\mathbf{l} = 2\pi n \quad n \in \mathbb{Z}, \tag{3.3}$$

i.e. the total phase change is an integer multiple of 2π, where n is the number of enclosed flux quanta.

The second key element of SQUID operation is the Josephson junction. It is formed by two superconducting electrodes separated by a thin insulating layer. The current I flowing through a single junction of this type is described by

$$I = I_c \sin(\delta), \tag{3.4}$$

where $\delta = \phi_1 - \phi_2$ is the phase difference between the superconducting wavefunctions in the two electrodes and I_c is the critical current. This describes the DC Josephson effect, in which a dissipationless supercurrent flows across the junction, as long as it remains below I_c [26].

A direct connection between flux quantisation and the Josephson effect is realised in a dc-SQUID. This device consists of two Josephson junctions connected in parallel on a superconducting loop (Figure 3.1(a)). When a bias current I_B is applied to the device, it splits between the two parallel paths, leading to the Josephson junctions. The total current through the device then depends on the two phase differences δ_1 and δ_2 across the two junctions. These phase differences are not independent but are determined by the magnetic flux threading the loop Φ_a

$$\delta_2 - \delta_1 = \frac{2\pi}{\Phi_0}\Phi_a, \tag{3.5}$$

leading to a flux-dependent interference of the currents. As a result, the total critical current of the SQUID becomes a periodic function of the applied magnetic flux Φ_a with period Φ_0. Assuming identical junctions and negligible loop inductance, the total current can be written as

$$I(\Phi_a) = 2I_c \cos\left(\frac{\pi\Phi_a}{\Phi_0}\right) \sin\left(\delta_1 + \pi\frac{\Phi_a}{\Phi_0}\right). \tag{3.6}$$

For a more realistic model accounting for junction resistance and the conversion of excess current into a measurable voltage, the critical current modulation translates directly into a periodic voltage response $V(\Phi_a)$, forming the basis of SQUID magnetometry.

In the MPMS3, the SQUID is operated in a flux-locked loop configuration, where flux deviations are continuously compensated for and converted into a proportional voltage signal. This feedback loop linearises the response and enables the detection of magnetic moments in the range of $1 \times 10^{-8}\,\mathrm{erg\,G^{-1}}$ [1]. Therefore, the instrument does not directly measure magnetic moments but rather the change in magnetic flux coupled into the SQUID detection circuit. This is subsequently reconstructed into an equivalent magnetic moment. This reconstruction is accurate provided that the system has been properly calibrated using a reference sample.

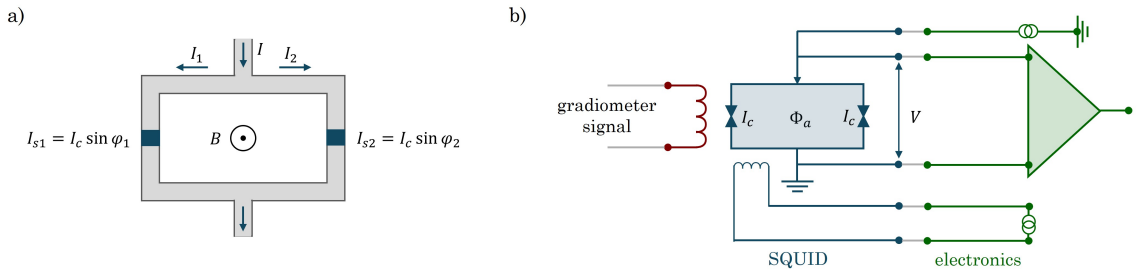


Figure 3.1: Illustration showing (a) a dc-SQUID with the superconducting loop containing two Josephson junctions, (b) the flux-locked loop feedback circuit for the dc-SQUID. Adapted from [27].

3.1.2 Experimental Setup

Measurement Setup

Magnetic flux from the movement of the sample is coupled into the SQUID via a second-order gradiometer consisting of superconducting detection coils arranged symmetrically along the vertical scan axis of the MPMS3 (Figure 3.2). The purpose of this geometry is to reduce contributions from external fields and homogeneous parts. These have a uniform contribution to all coil windings and are therefore cancelled by the alternating winding configuration. Consequently, the signal is primarily sensitive to the localised sample that moves through the gradiometer.

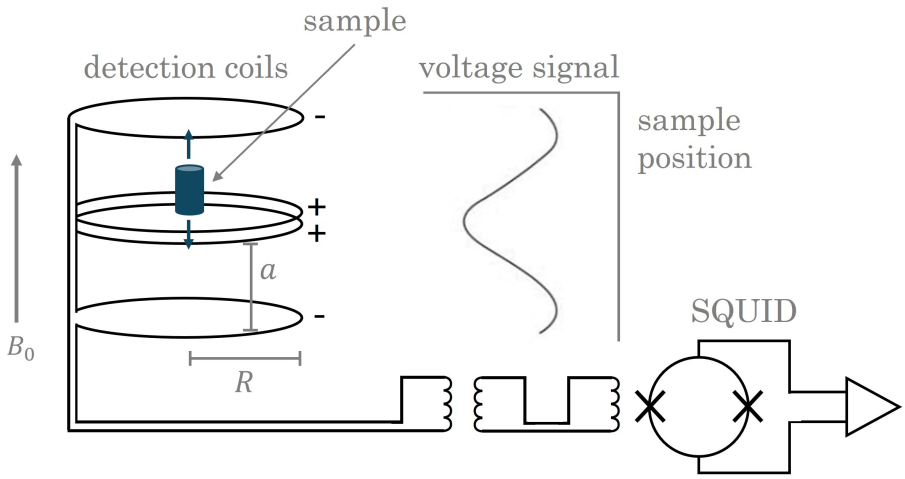


Figure 3.2: Schematic illustration of the SQUID signal generation in an MPMS3, showing the second order gradiometer with a sample moving through it, the connection to the SQUID and the generated Signal. Adapted from [1].

This is essential for measurements in the MPMS3, as this reduces contributions from environmental magnetic fields and signals from sample holders that are uniform throughout the length of the gradiometer (16 mm plus scan length), while maintaining sensitivity to localised fields generated by the sample. As a result, employing the second order gradiometer improves the signal-to-background ratio, which is particularly important for samples with small magnetic moments.

Magnetic measurements performed with the MPMS3 produce signals that correspond to the convolution of the sample's magnetic response with the response function of the gradiometer coils. Consequently, the measured signal corresponds to a spatially weighted integral of the magnetic moment distribution along the scan axis. For a point-like magnetic moment, the response of the MPMS3 to a point like magnetic moment can be approximated by the coil response function

$$V(z) = A\left[\frac{2}{[(z-z_0)^2+R^2]^{3/2}} - \frac{1}{[(z-z_0-a)^2+R^2]^{3/2}} - \frac{1}{[(z-z_0+a)^2+R^2]^{3/2}}\right] + Bz + C \tag{3.7}$$

where A is a scaling factor proportional to the magnetic moment, z_0 is the sample centre position, a ist the distance between the central coils and the outer coils, R is the coil radius and $Bz + C$ represent linear and constant background contributions [1]. A fit of this function to a static field scan of a reference sample measured with the MPMS3 is shown in Figure 3.3. From the fit, the sample position along the scan axis and the magnetic moment are extracted.

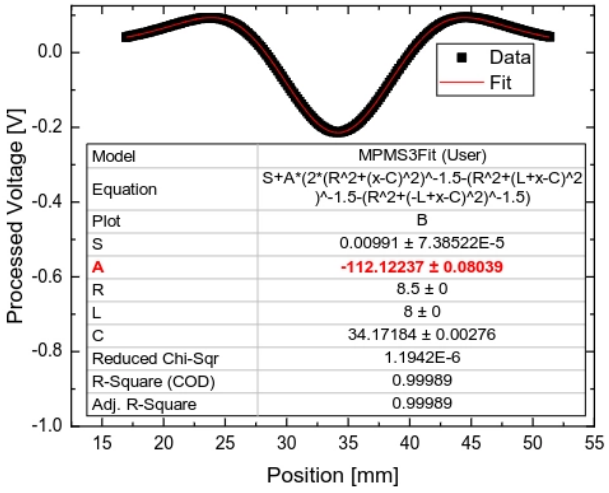


Figure 3.3: Representative static field SQUID scan measured using a MPMS3, together with a fit based on the dipole transfer function. The model accounts for the pickup coil geometry and sample position along the scan axis, enabling extraction of the magnetic moment. Taken from [28].

Cooling

The temperature control in the MPMS3 is based on the use of liquid ^{4}He and, where required, an additional ^{3}He insert (iQuantum ^{3}He option, Quantum Design Inc.) for sub-Kelvin measurements. The MPMS3 contains a liquid helium bath, in which the SQUID is submerged for cooling. The superconducting magnet gets cooled by the helium vapour to keep it in its superconducting state. Most importantly, the temperature regulation of the sample chamber is automated and realised by controlled exchange of the helium vapour. The temperature of the sample chamber can be continuously varied between 1.8 K to 400 K in the standard configuration, and down to 400 mK using the ^{3}He insert [1].

Measurement modes

The range of measurement modes of the MPMS3 includes direct current (DC) magnetometry, alternating current (AC) magnetometry, and vibrating sample magnetometry (VSM). Each mode provides information about different aspects of a sample's magnetic behaviour, allowing a comprehensive analysis of the electronic configuration and magnetic interactions. As only DC measurements were performed in this thesis, the following discussion focuses on this measurement mode in more detail.

DC magnetometry forms the basis for the magnetic characterisation of a sample. In this mode, the MPMS3 records repeated scans of the sample with a static magnetic field and fixed temperature. The DC mode offers exceptional sensitivity (in the range of $1 \times 10^{-8}\,\mathrm{erg\,G^{-1}}$) and is therefore particularly well suited for weakly magnetic systems [1]. In this mode, two main measurement protocols, both measuring the magnetic moment, are usually performed: isothermal magnetisation measurements $M(B)$, in which the applied field is varied while the temperature stays constant, and constant-field magnetisation measurements $M(T)$, where a static field is applied with varying temperatures. Together, these enable the identification of various magnetic contributions, e.g. paramagnetic behaviour by fitting the Brillouin function to $M(B)$ data, and the characterisation of magnetic interactions, e.g. through combined analysis of deviations from Brillouin behaviour in $M(B)$ and fitting the Curie–Weiss law to $M(T)$.

The accuracy of these measurements is critically influenced by the chosen experimental parameters of the device. The scan length determines the spatial range over which the SQUID voltage profile is recorded and must be chosen to fully capture the dipole response while minimising contributions from the sample holder. The number of scans averaged per measurement point directly reduces statistical noise, and is particularly important at low temperatures where the signal-to-noise ratio is otherwise limited by instrumental noise. The precise control of these parameters gets especially important for the characterisation of weakly magnetic systems.

Conventional Sample Mounting Techniques

Both, accurate sample positioning and minimisation of extrinsic magnetic contributions, are essential for reliable extraction of the true magnetic moment of the sample. Even weak contributions from sample holders, adhesives or impurities can introduce systematic offsets comparable to the intrinsic signal of weakly magnetic materials [1]. These effects enter additively into the measured magnetisation and must therefore be carefully controlled or subtracted.

Figure 3.4 shows sample mounting configurations from Quantum Design, including quartz holders, brass holders, and straw-based assemblies. These differ in sample compatibility, mechanical stability, and magnetic background. Quartz holders are preferred for low-moment samples due to their minimal and temperature-independent diamagnetic response, whereas brass provides greater rigidity but is often used with plastic capsules (Figure 3.4), which introduces a measurable magnetic background requiring correction if the capsules moment is not insignificant against the moment of the sample. Straw-based mounts are convenient but more prone to thermal contraction which can affect centring accuracy and reproducibility [1].

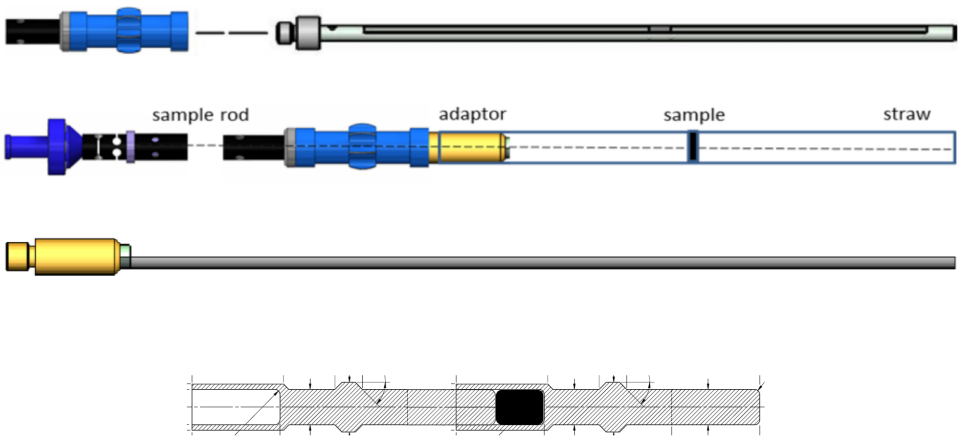


Figure 3.4: Sample mounting options for the MPMS3. From top to bottom: brass sample holder (Quantum Design MPMS 3 Brass Trough Sample Holder, QDC-4500-608), plastic straw (Quantum Design Standard Sample Holder, QDC-8000-001) with straw adapter (Quantum Design ACMS II straw adapter assembly, QDC-4084-814), quartz sample holder (MPMS 3 Quartz Paddle Sample Holder, QDC-4500-604), and plastic capsule (Quantum Design VSM powder sample holder, 4096-388) used with the brass sample holder. Taken from [1, 29].

A critical requirement for reliable measurements is precise centring of the sample within the SQUID gradiometer coils. This is important as deviations introduce asymmetric distortions in the measured signal, which propagate into systematic errors in the fitted magnetic moment. The Quantum Design mounting and positioning tool (Figure 3.5) is used to reproducibly place the sample at the intended position for the MPMS3. This reduces user-dependent errors and improves consistency between experiments. It is also recommended to maintain a consistent rotational orientation of the sample and sample holder between measurements to minimise uncertainties [28].

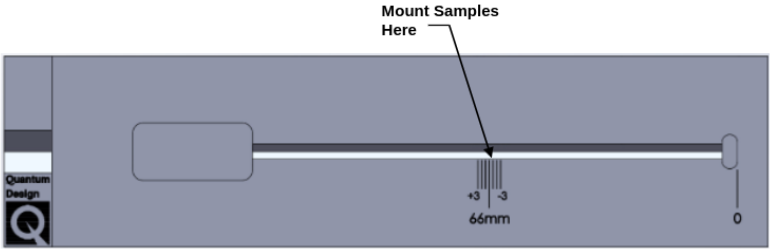


Figure 3.5: Sample mounting and positioning tool supplied with the MPMS3, used for aligning samples for measurements. Taken from [1].

Beyond geometric considerations, magnetic cleanliness is an important experimental factor in SQUID magnetometry. Any ferromagnetic contamination, even at the level of microscopic particles or trace residues (e.g. from metallic dust or tweezers), produces field-dependent contributions [29]. Similarly, contributions from paramagnetic impurities may become significant at low temperatures. To mitigate these effects, all sample handling must be performed using non-magnetic tools, and all mounting materials are required to have a low and well-characterised magnetic susceptibility. In practice, the total measured response is interpreted as

$$\chi_{\text{eff}} = \chi_{\text{intrinsic}} + \chi_{\text{holder}} + \chi_{\text{impurities}}, \tag{3.8}$$

where the latter two contributions must be independently assessed or minimised to enable quantitative analysis of $\chi_{\text{intrinsic}}$.

3.1.3 Data Analysis

Signal Processing

Two distinct data-processing workflows are employed, depending on the strength of the magnetic moment of the investigated samples. For samples with strong magnetic moments, the contributions from the sample holder are negligible, therefore the internally fitted data provided by the MPMS3 can be used directly. These data are then exported and further processed in OriginPro 2025 (OriginLab Corporation, Northampton, MA, USA), where normalisation, visualisation, and fitting procedures were performed for the analysis of the magnetic properties. In contrast, for samples with low magnetic moments on the order of the magnetic signal of the sample holder, the internal fitting routine of the MPMS3 is not

usable. For these samples background subtraction is required [28]. For this, the raw voltage scan files are directly used and background subtraction is performed to isolate the sample contribution. This can then, again, be further analysed in OriginPro.

Background Subtraction

For low magnetic moment samples, background subtraction was performed using raw DC scan data obtained from the MPMS3. In this approach, the internally fitted MPMS3 output is not used, instead, the raw voltage-versus-position scan data are processed directly using a dedicated background subtraction software developed in the group of Anton Jesche at the university of Augsburg.

To achieve a reliable background subtraction, the measurements of the empty sample holders must be performed under identical experimental conditions as the measurements with the sample. Another requirement for accurate determination of magnetic moments from the background subtracted data is accurate sample positioning. Figure 3.6 shows the effect of a 1 mm positional offset between the sample and background measurements on the subtracted signal at different signal-to-background ratios. This shows that even small misalignments lead to significant deviations in the extracted magnetic moment. As a reference, the ideal signal in the absence of any misalignment should resemble the dipole response shown in Figure 3.3. This demonstrates that accurate and reproducible sample positioning is critical to obtain reliable data. In fact, it could be argued that it is more important than the absolute magnetic moment of the sample holder.

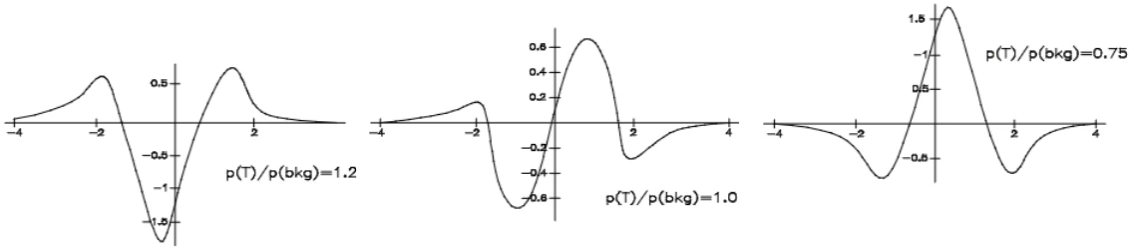


Figure 3.6: Effect of a 1 mm positional offset between sample and background DC scans on the subtracted signal, which ideally represents the isolated sample moment. Results are shown for decreasing ratios of sample moment $p(T)$ to background moment $p(bkg)$ from left to right. Adapted from [30].

The calibration of the software was performed to match the moment scale of the MPMS3, using the palladium reference sample (Quantum Design, Part No. 4500-645) which was supplied with the MPMS3. Palladium is used as a reference due to its well-characterised paramagnetic susceptibility, which enables reliable determination of the calibration factor [31]. During the setup of the software, a DC scan of the palladium reference sample is used to determine the calibration factor, which is then automatically applied to convert the processed signal into absolute magnetic moment units, analogous to the internal MPMS3 fitting routine.

In this work, background subtraction is an integral part of the measurement analysis, as it lays the foundation for the measurement of weakly magnetic samples. The consistency between raw scans, subtracted data and fitted signals was therefore always carefully verified. Deviations from expected behaviour were used as indicators of potential systematic errors and were identified by comparing measurements across different field strengths, temperatures, and repeated runs. Inspection of the raw data proved particularly important, as the MPMS3 occasionally introduces artefacts of unclear origin like abrupt jumps or other anomalies.

Geometry Correction

The MPMS3 is calibrated with cylindrical samples with a diameter of 2.8 mm and a height of 3.8 mm. Therefore, deviations from this geometry can lead to systematic errors in the measured magnetic moment. To account for this, the Quantum Design MPMS3 Sample Geometry Simulator was used [32]. This tool calculates geometry-dependent correction factors for DC and VSM measurements based on sample dimensions and shape (including cylinder, thin film, and rectangular prism), as well as scan length and radial offset (Figure 3.7). The measured signal must then be corrected by dividing by the corresponding factor.

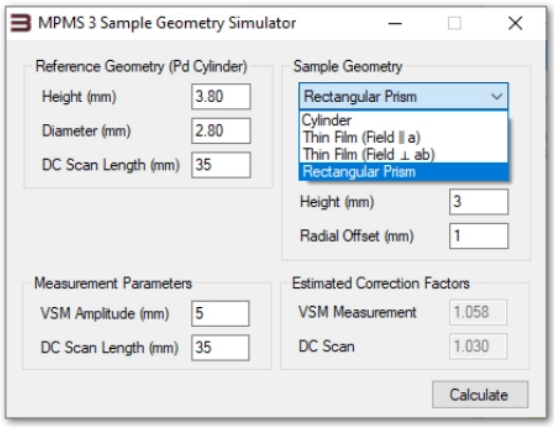


Figure 3.7: Graphical user interface of the Quantum Design MPMS3 Sample Geometry Simulator used to determine the correction factor for the magnetic moment of samples with non-standard geometries. Taken from [32].

3.2 X-band EPR Spectroscopy

3.2.1 Measurement Concept

Electron Paramagnetic Resonance spectroscopy, also referred to as Electron Spin Resonance (ESR) spectroscopy, probes transitions between Zeeman-split spin states of unpaired electrons in an external magnetic field using microwave radiation. In a static field B, the

spin energy levels split according to the Zeeman effect, introduced in Equation (2.10). For a single $S = 1/2$ system, resonant absorption occurs when the microwave photon energy matches the energy separation between the spin states

$$h\nu = g_s \mu_B B, \tag{3.9}$$

where ν is the microwave frequency (Figure 3.8(a)). In continuous-wave X-band EPR measurements, the sample is placed in a resonant cavity and irradiated with microwaves while the external magnetic field is varied. The resulting absorption signal is recorded as a function of field strength and its first-derivative is typically used for further analysis (Figure 3.8(b)). The analysis provides precise information on the local electronic structure and magnetic interactions of the measured paramagnetic centre [33].

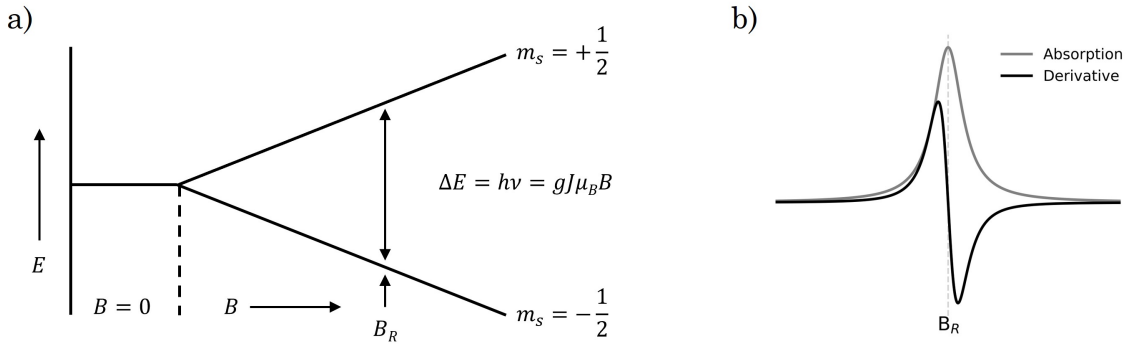


Figure 3.8: Schematic of EPR spectroscopy for a single unpaired electron spin. (a) Zeeman splitting of the $m_s = \pm 1/2$ energy levels of a spin-1/2 system upon application of an external magnetic field. At the resonance field B_R, resonant absorption occurs, manifesting as an absorption peak shown in (b), together with its derivative, which is typically recorded in EPR measurements. Adapted from [33].

X-band EPR, which operates at microwave frequencies of approximately 9 GHz to 10 GHz, is the most widely used variant of continuous-wave EPR spectroscopy due to its high sensitivity and widespread availability of instrumentation [33]. It is highly sensitive to paramagnetic centres even at low concentrations and provides microscopic information on unpaired electrons and their local environment. X-band EPR serves as a complementary technique to SQUID magnetometry. It enables the analysis of paramagnetic properties while remaining insensitive to diamagnetic contributions. This provides additional insight into the electronic properties of the sample, which could otherwise be masked by more dominant bulk magnetic behaviour.

3.2.2 Experimental Setup

EPR measurements were performed at X-band frequencies (9.4 GHz to 9.8 GHz) at the Institute of Inorganic Chemistry, Heidelberg University, in the group of Prof. Dr. Peter Comba. The used device is a Bruker Elexsys E500 spectrometer equipped with an ER 041 XK CW

microwave bridge, an ER 4116DM dual-mode resonator, and a B-E25 electromagnet. This setup enables static fields up to 1.3 T. Temperature-dependent measurements were conducted using a Bruker ER 4112HV-CF58nc cryogen-free variable temperature system controlled by an Oxford Instruments Mercury iTC, enabling measurements in the range of 6 K to 400 K. The sample temperature provided by this setup is known to deviate systematically from the set value, therefore the reported temperatures have a high uncertainty.

3.2.3 Data Analysis

The analysis of EPR spectra was performed using the MATLAB-based software package EasySpin [34] within the MATLAB environment (EasySpin 6.0, MATLAB R2025, MathWorks Inc., Natick, MA, USA). EasySpin is an open-source toolbox for the simulation and fitting of EPR spectra and supports a wide range of spin systems, including those exhibiting anisotropic g-tensors, hyperfine interactions, and exchange coupling. Both, powder and single-crystal spectra can be simulated, enabling direct comparison between experimental spectra and theoretical models. This approach enables quantitative analysis of the local electronic structure and magnetic interactions of the investigated paramagnetic moments.

3.3 Additive Manufacturing

Advances in additive manufacturing have enabled the fabrication of custom components with precisely defined geometries and controlled material properties. This allows the production of application-specific experimental setups with a level of geometric freedom and reproducibility that is difficult to achieve using other fabrication techniques [35]. In this work, these capabilities are employed to fabricate custom sample holders for the MPMS3 SQUID magnetometer, where tight dimensional tolerances and strict geometric constraints imposed by the instrument must be satisfied.

3.3.1 Printing Technology

Among the available additive manufacturing techniques, stereolithography (SLA) is particularly well suited for the fabrication of small and geometrically complex structures due to its high spatial resolution, excellent surface quality, and high dimensional reproducibility [36]. In contrast to filament-based methods, SLA enables the production of thin-walled, high-aspect-ratio structures with reduced surface roughness, making it well suited for applications requiring precise dimensional control. This is achieved by using an ultraviolet (UV) laser to selectively cure a liquid photopolymer resin layer by layer to form a solid 3D structure (Figure 3.9). A refinement of this approach is provided by low force stereolithography (LFS), which reduces peel forces during the separation of the printed layer from the transparent bottom film. This lowers mechanical stress on the printed part and improves both surface quality and dimensional accuracy compared to other SLA systems.

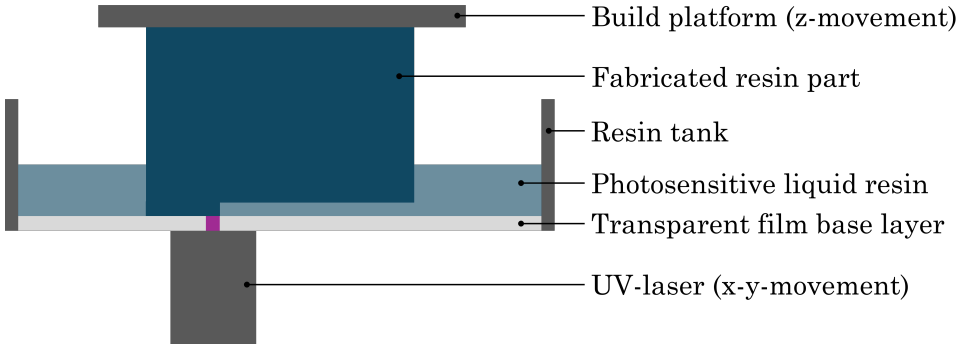


Figure 3.9: Schematic representation of the SLA 3D-printing process., showing an UV laser selectively curing a liquid photopolymer resin layer by layer to form a solid 3D structure. Adapted from [37].

3.3.2 Fabrication and Post-processing

All parts were designed using Autodesk Fusion 360 (Autodesk, Inc., San Francisco, CA, USA) and fabricated on an SLA 3D-printer (Formlabs Form 3, located at the 3D printing core facility at IMSEAM, Heidelberg University) which implements the LFS technique. This device uses a UV-curable photopolymer (Formlabs Clear Resin V4), which undergoes polymerisation upon irradiation with 405 nm UV light [38]. The resulting material is a three-dimensional cross-linked thermoset polymer network. Its mechanical and thermal properties are primarily governed by the degree of monomer conversion and the density of cross-links formed during curing. Immediately after printing, the material is in a partially cured state with a degree of conversion of approximately 60 % to 70 % [39]. In this state, residual monomers and photoinitiator by-products remain embedded within a partially cross-linked network.

Post-processing was performed using an agitated isopropanol bath (Formlabs Form Wash V1) and a curing oven (Formlabs Form Cure V1). Printed parts were cleaned in the agitated bath to remove surface residues and extract unreacted resin from the printed part. Solvent-induced swelling was minimised by limiting the duration of the washing process according to manufacturers specifications, followed by ambient drying to ensure complete solvent evaporation. Subsequent UV post-curing at 405 nm irradiation under controlled temperature conditions increases the degree of conversion to above 90 % to 95 %, resulting in the formation of a cross-linked network [38]. Uneven shrinkage of the material during the curing process was reduced by using controlled irradiation and temperature profiles which are supplied by the manufacturer. This leads to more homogeneous curing, resulting in parts with higher dimensional accuracy. From a mechanical perspective, post-curing increases the tensile strength and stiffness [38]. Another advantage of enforcing the complete curing of the printed part is its magnetic behaviour. Incompletely cured resin may contain residual resin species or photoinitiator fragments, which can introduce weak magnetic contributions. Full conversion of the photopolymer ensures a stable and reproducible background signal, which is required for sensitive SQUID measurements. After the post processing, all components were inspected for dimensional accuracy and fabrication defects. The fabrication

and post-processing conditions were kept consistent across all prints to ensure reproducible mechanical and magnetic properties.

However, the mechanical properties of the printed components are not determined solely by the material itself. The orientation of components during SLA fabrication has a direct impact on residual stress formation and post-curing dimensional stability [40]. Improper orientation can lead to anisotropic shrinkage and mechanical deformation, which is particularly relevant for precision components [41]. To minimise these effects, all sample holders were fabricated vertically or at a slight tilt of up to 5° relative to the build axis. This reduces the cross-sectional area per layer and promotes more uniform curing along the build direction, limiting internal stress gradients. The slight tilt additionally reduces the required support structures without sacrificing the benefits of near-vertical orientation. With this, post-curing-induced distortions were successfully reduced, ensuring high geometric reproducibility and reliable integration into the magnetometer's sample space.

Beyond their mechanical and thermal properties, the magnetic response of cured photopolymers is also relevant for experimental applications. Magnetic susceptibility measurements of photopolymers using magnetic resonance imaging (MRI)-based techniques have shown that cured SLA resins, including Formlabs Clear Resin V4, are weakly diamagnetic with susceptibilities typical of common organic polymers [42]. This confirms that the cured material can be used to produce sample holders that exhibit only a weak background suitable for SQUID magnetometry.

Table 3.1: Summary of printing, washing and curing parameters, as well as the materials and devices used for fabrication of the sample holders.

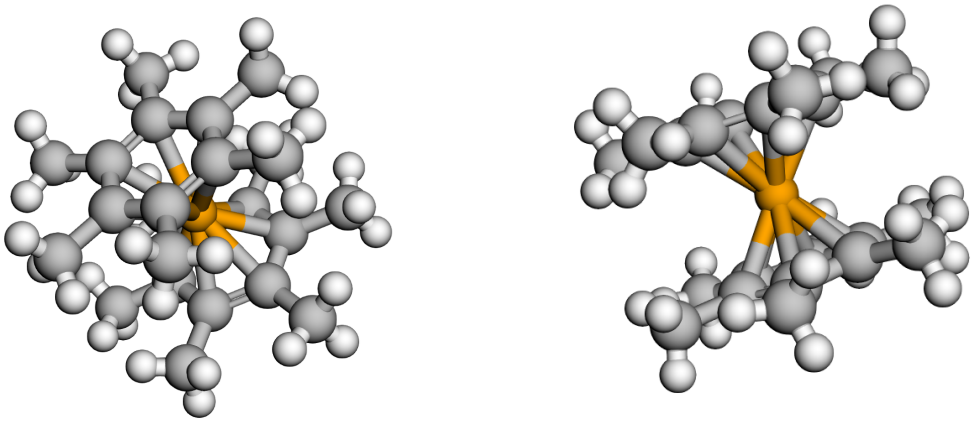
Printing	
Device	Formlabs Form 3 SLA 3D-printer (using Low-Force Stereolithography)
Software	Formlabs PreForm (Version 3.45)
Resin	Formlabs Clear V4
Layer Thickness	25 µm to 100 µm (adaptive mode)
Part Orientation	Vertical or up to 5° tilt, optimised to reduce support marks and anisotropic shrinkage
Supports	Light-touch automatic supports, manually removed prior to curing
Washing	
Device	Formlabs Form Wash V1 (agitated bath)
Solvent	Isopropanol (purity $\geq 99\,\%$)
Duration	20 min
Drying	Air drying until complete solvent evaporation (4 h to 6 h) to prevent swelling-induced deformation
Curing	
Device	Formlabs Form Cure V1 (UV & thermal post-curing)
Temperature	60 °C
Duration	30 min
UV Source	405 nm LED

4 Probing Distance-Dependent Coupling in Fe(I) Sandwich Complexes

4.1 Overview of Fe(I) Systems

4.1.1 Structure and Electronic Configuration

For this part of the project, the magnetic properties of the homoleptic Fe(I) sandwich complex $[Fe(C_6(CH_3)_6)_2]^+$ were investigated using SQUID magnetometry and X-band EPR spectroscopy. The cation $[Fe(C_6(CH_3)_6)_2]^+$, hereafter referred to as the *Fe(I) complex*, is an organoiron sandwich complex in which an Fe(I) ion is coordinated by two hexamethylbenzene ($C_6(CH_3)_6$, HMB) ligands. This arrangement results in an arene sandwich structure analogous to metallocenes [43, 44, 45], as shown in Figure 4.1. The compounds were supplied by Oliver Townrow (Karlsruhe Institute of Technology) in the general form $[Fe(HMB)_2]^+[WCA]^-$, where WCA denotes a weakly coordinating anion. The electronic



(a) (b)

Figure 4.1: Molecular structure of the investigated Fe(I) complex, showing (a) a view focussing on one HMB ligand, and (b) the overall sandwich-type coordination geometry. Colour scheme: Fe (orange), C (grey), H (white).

configuration, and thus the magnetic behaviour, of the Fe(I) centre is determined by the bonding type with its ligands. The Fe(I) ion is coordinated by both HMB ligands in an η^6-hapticity mode, meaning that the aromatic π-system, built from the carbon p_z orbitals of the hexamethylbenzene ligand, interacts with the metal centre through the delocalised ring orbitals rather than the individual atoms. The six methyl groups on each ring increase the electron density of the aromatic π-system. This further stabilises the Fe(I) oxidation state. With both ligands arranged parallel around the central ion, the complex adopts an approximately D_{6h}-symmetric structure.

Within this ligand field, the Fe(I) ion adopts a low-spin d^7 electronic configuration corresponding to a spin of $1/2$. A qualitative representation of the resulting orbital splitting and electron occupancy is shown in Figure 4.2. The relative energies and symmetry of the highest occupied molecular orbital (HOMO) and the orbital immediately below it remain unclear, as the two computational techniques, density functional theory (DFT) and complete active space self-consistent field (CASSCF), disagree on which lies lower depending on whether orbital energy or occupancy is considered. Nevertheless, the singly occupied molecular orbital (SOMO) is consistently predicted to be a π-orbital of e_{1g} symmetry [46], which is the more important information, as the symmetry and spatial distribution of the SOMO are of central importance for the magnetic properties of the complex.

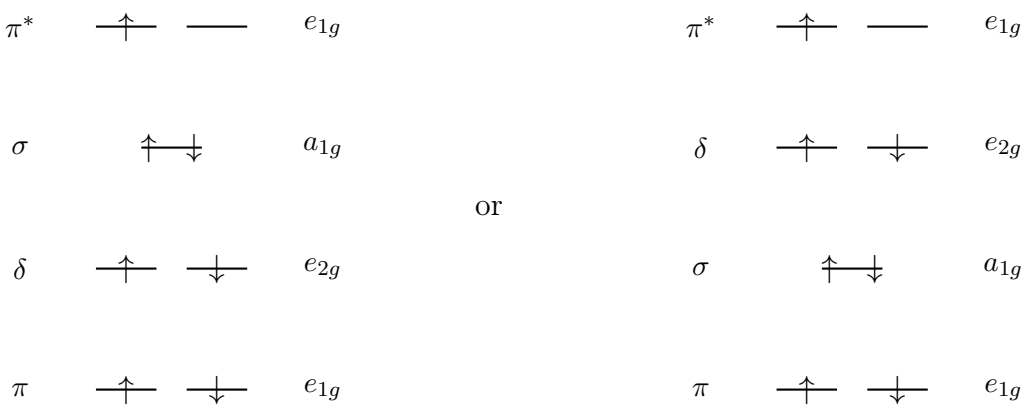
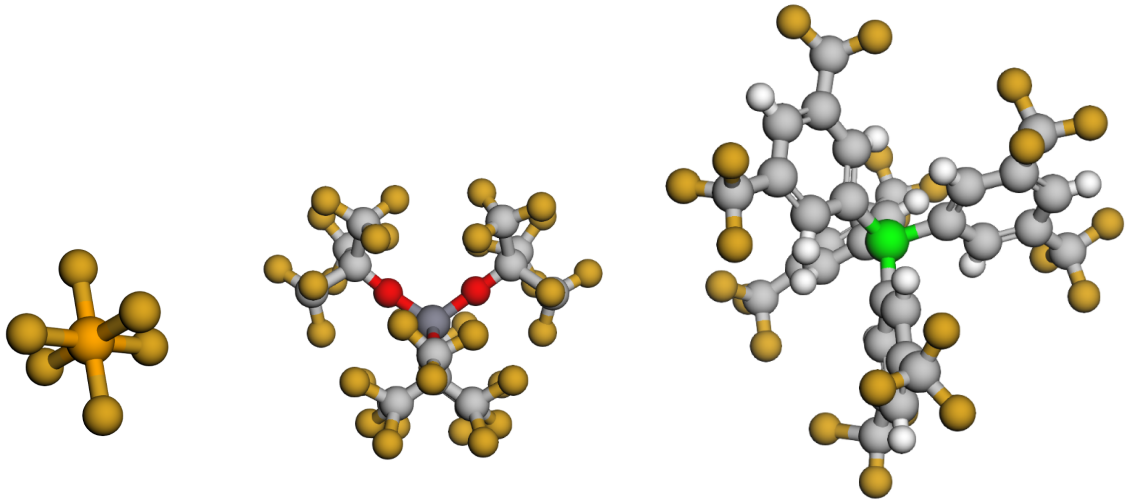


Figure 4.2: Molecular orbital diagram showing two possible electronic configurations of the Fe(I) ion in the Fe(I) complex. The two cases differ in the symmetry and occupation of the SOMO. The labels π^*, σ, δ, and π denote the bonding character of the molecular orbitals, while e_{1g}, e_{2g}, and a_{1g} indicate their symmetry. Adapted from [46].

4.1.2 Investigated Samples

Each investigated sample contains the Fe(I) complex along with its associated counterion, which varies between samples. All samples were supplied as powders, and Crystallographic Information Files (CIFs) were provided for structural reference. The synthesis of the investigated samples was carried out using dichloromethane (CH_2Cl_2, DCM). While the solvent is necessary for the synthesis of the compounds, residual DCM should ideally be already removed prior to measurements. However, there is the possibility of leftover DCM in the samples, which could influence the magnetic measurements.



(a) PF_6^- (b) $Al(OR^F)_4^-$ (c) $B(Ar^F)_4^-$

Figure 4.3: Anions used in Fe(I) samples, arranged in order of increasing size from (a) to (c). Colour scheme: F (yellow), P (orange), Al (dark grey), O (red), C (light grey), B (green), H (white).

For this study, three weakly coordinating anions (Figure 4.3) were employed, which determine the intermetallic spacing within the Fe(I) samples (Table 4.1): PF_6^-, $Al(OR^F)_4^-$ ($R^F = C(CF_3)_3$), and $B(Ar^F)_4^-$ ($Ar^F = C_6H_3(CF_3)_2$).

Table 4.1: Fe(I) complexes, counterions, and Fe–Fe distances derived from CIFs obtained through x-ray diffraction (XRD) measurements, including the nearest-neighbour distance and the average Fe–Fe separation.

Cation	Anion	Nearest neighbour distance (Å)	Average distance (Å)
$Fe(HMB)_2$	PF_6^-	7.888	9.200
$Fe(HMB)_2$	$Al(OR^F)_4^-$	9.205	10.671
$Fe(HMB)_2$	$B(Ar^F)_4^-$	9.865	12.386

4.1.3 Sample Preparation

All samples were handled and prepared under inert conditions inside an argon-filled glovebox to prevent exposure to air and moisture.

For SQUID magnetometry, the masses of the samples were determined using an analytical balance (Mettler Toledo JBI603-C/FACT). To ensure accurate mass determination, the sample capsule was weighed three times empty and three times after filling, with the average values used. The typical sample mass was around 10 mg, exact masses are listed in Table 4.2. For measurements above 1.8 K, i.e. not using the ^{3}He option, the sample was sealed in a plastic capsule (Quantum Design VSM Powder Sample Holder, 4096-388) and mounted in a brass MPMS3 sample holder (Quantum Design MPMS 3 Brass Half-tube Sample Holder, 4500-608). For measurements using the ^{3}He option, the plastic capsule was trimmed to remove excess material, and the remaining portion containing the sample was glued into a polypropylene straw (Quantum Design, 4500-668) using GE 7031 varnish (Lake Shore Cryotronics, Westerville, OH, USA) and installed using the straw adapter (Quantum Design, 4500-666). In both cases, positioning of the sample within the holder was performed inside the glovebox using the standard alignment tool provided with the MPMS3. After preparation, the sample was quickly transferred to the magnetometer to prevent exposure to oxygen and moisture.

For EPR spectroscopy, powder samples were dissolved in 1,2-difluorobenzene (DFB), chosen for its absence of EPR signal, non-coordinating character, and tendency to form a homogeneous solid upon freezing, which is required for obtaining a well-defined rigid powder spectrum. The solvent-to-sample ratio was adjusted to ensure complete dissolution of the powder. In contrast to SQUID magnetometry, where sample mass directly determines the measured magnetic moment, the mass is not critical for EPR analysis, as the technique probes the local electronic structure of individual paramagnetic centres rather than collective magnetic phenomena, and the relevant quantity extracted, the g-factor, is an intrinsic property of the paramagnetic centre independent of the amount of material measured.

Table 4.2: Molar masses and sample masses of the investigated Fe(I) compounds used for SQUID magnetometry measurements.

Cation	Anion	Molar mass ($g\,mol^{-1}$)	Sample mass (mg)
$Fe(HMB)_2$	PF_6^-	525.35	10.3
$Fe(HMB)_2$	$Al(OR^F)_4^-$	1243.63	21.3
$Fe(HMB)_2$	$B(Ar^F)_4^-$	1328.53	12.6

4.2 $[Fe(HMB)_2][PF_6]$

X-band EPR was used to measure the microwave absorption of dissolved $[Fe(HMB)_2][PF_6]$ as a function of the applied magnetic field at 75 K, at which the solvent (DFB) is frozen, yielding a rigid powder spectrum. The first derivative of the absorption spectrum was analysed, from which the anisotropic g-tensor was determined to be

$$g = \begin{pmatrix} 2.033 & 0 & 0 \\ 0 & 1.995 & 0 \\ 0 & 0 & 1.995 \end{pmatrix}. \tag{4.1}$$

Since the SQUID magnetometry measurements were performed on a powder sample, in which all molecular orientations are equally represented, the orientationally averaged g-factor is the relevant quantity for comparison with bulk susceptibility data. To a good approximation, this is given by the root-mean-square (RMS) average, $\bar{g} = \sqrt{\frac{1}{3}(g_{xx}^2 + g_{yy}^2 + g_{zz}^2)} = 2.008$, and serves as the reference value for the analysis of the field-dependent magnetisation presented in the following.

The DC magnetisation of $[Fe(HMB)_2][PF_6]$ was measured as a function of the applied magnetic field in the range 0 T to 7 T at temperatures of 1.8 K, 3 K, and 5 K. Before the analysis, the data were normalised to sample mass and molar mass. The resulting M(B) data is presented in units of μ_B per formula unit in Figure 4.4(a). The 1.8 K dataset exhibits the steepest initial slope, followed by the 3 K and 5 K curves. The curvature is most pronounced at 1.8 K, indicating a stronger tendency towards saturation at lower temperatures. With increasing temperature, the magnetisation response becomes progressively more linear within the measured field range, and none of the curves reaches saturation. Attempts to fit the data using a Brillouin function (Equation (2.11)) do not yield satisfactory results, indicating that the system cannot be described as an ensemble of non-interacting paramagnetic centres. This suggests the presence of magnetic interactions, the nature of which cannot be fully assessed from this data alone. The temperature-dependent susceptibility data will provide additional information on this. The g-factor anisotropy seen in X-band EPR spectroscopy may also contribute to these deviations, as it is not captured by the used Brillouin model. It is also observable, that the magnetisation does not saturate within the measured field range of 7 T. For a spin-1/2 system with $g \approx 2$, saturation of the magnetic moment is expected at a magnetic moment of approximately $1\,\mu_B$ per formula unit. To further assess if this value is reached, either higher applied fields or lower temperatures are required.

For further analysis, the field-dependent isothermal magnetisation data were rescaled by temperature and plotted in the right panel of Figure 4.4. The three datasets initially overlap but diverge with increasing B/T, with the 1.8 K data exhibiting the lowest moment at fixed B/T, followed by the 3 K and 5 K curves. For an ensemble of non-interacting paramagnetic moments, the magnetisation depends only on the ratio B/T, and all isotherms should collapse onto a universal curve. Crucially, this holds even in the presence of g-anisotropy, since each contribution still depends only on B/T. The observed failure of the isotherms to collapse is therefore attributed to interactions between the magnetic centres. The measured moment at fixed B/T decreases with decreasing temperature. As the thermal energy is

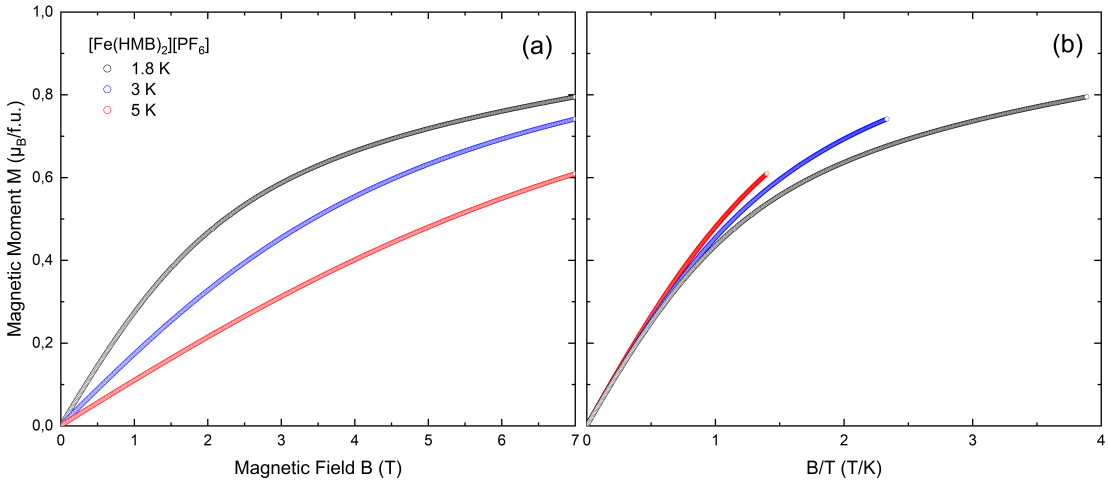


Figure 4.4: Field-dependent isothermal magnetisation of $[Fe(HMB)_2][PF_6]$ measured between 0 T and 7 T at temperatures of 1.8 K (black), 3 K (blue), and 5 K (red), shown in units of μ_B per formula unit. (a) Magnetic moment M as a function of applied field B. (b) Magnetic moment with the field axis rescaled by temperature to highlight magnetic interactions.

reduced, the exchange interactions become increasingly significant relative to k_BT, counteracting the field-induced alignment and suppressing the net magnetisation below the value expected for a non-interacting paramagnet. This is consistent with antiferromagnetic interactions, which become more prominent at lower temperatures and suppress the net magnetic moment. This provides a coherent explanation for the failure of the Brillouin function fit to the $M(B)$ data observed previously.

Temperature-dependent magnetisation measurements were peformed at applied magnetic fields of 0.1 T and 1 T. From these measurements, the molar magnetic susceptibility χ was calculated using the measured magnetic moment using the sample mass and molar mass, both listed in Table 4.2, and the applied magnetic field. The result is plotted together with the corresponding inverse susceptibility χ^{-1} in Figure 4.5. Representing the data as inverse susceptibility results in linear behaviour of the Curie–Weiss law at high temperatures. This facilitates the identification of Curie–Weiss behaviour and enables the parameters of the Curie–Weiss fit to be extracted more reliably. These fitted parameters are the g-factor, the temperature-independent contribution χ_0, and the Weiss temperature Θ_W. The measurements was repeated at two different magnetic fields to examine field-dependent effects and to verify the consistency of the magnetic response.

Although both datasets exhibit similar behaviour, the susceptibility curves obtained at 0.1 T and 1 T do not overlap across the entire temperature range, with the 0.1 T data showing systematically lower susceptibility values than those at 1 T. This indicates a field-dependent contribution to the measured susceptibility, which may originate from several sources, including sample holder contributions, remanent magnetic fields of the magnet, or impurities and sample degradation. The observed temperature behaviour resembles Curie–Weiss law

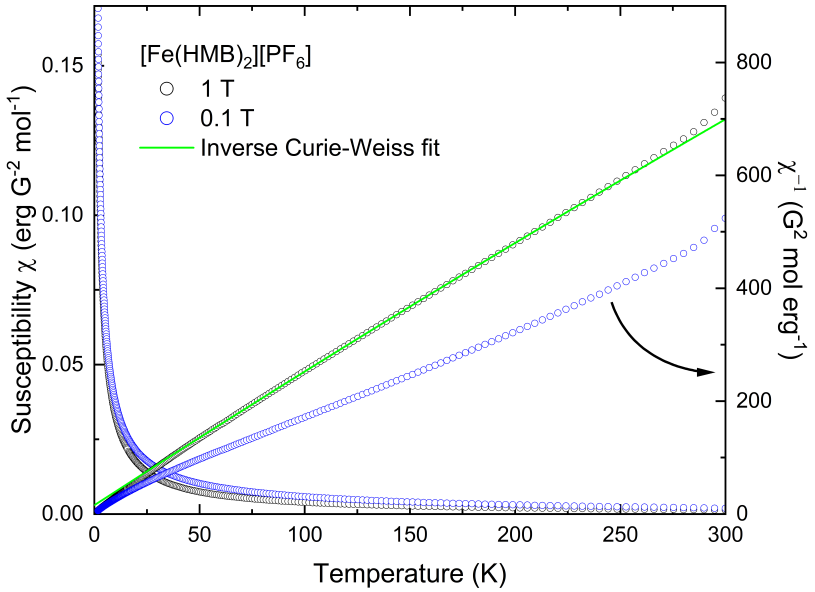


Figure 4.5: Temperature dependence of the molar magnetic susceptibility $\chi(T)$ and inverse susceptibility $\chi^{-1}(T)$ of $[Fe(HMB)_2][PF_6]$ measured at applied fields of 0.1 T (blue) and 1 T (black). The solid green line represents a Curie–Weiss fit to $\chi^{-1}(T)$ in the high-temperature region.

(Equation 2.24) behaviour, with deviations at high temperatures, above 270 K, manifesting as a steeper than linear increase in $\chi^{-1}(T)$ at both fields. Further analysis involved fitting the Curie–Weiss law (Equation 2.24) to the high-temperature region of $\chi^{-1}(T)$, yielding parameters that provide a quantitative basis for comparison across the three compounds. Due to the Curie–Weiss law being an approximation at high temperatures, the fitting procedure was generally restricted to temperatures above 50 K. The Weiss temperature was obtained from a Curie–Weiss fit of the 1 T data, in the temperature range 50 K to 250 K, yielding $\Theta_W = -6.5\,\mathrm{K}$. The uncertainty was estimated by varying the fit window. The different fit results are shown in Table 4.3. Including the statistical fit error, a value of $\Theta_W = -6.5(7)\,\mathrm{K}$ is obtained. Additionally, the fit results in a g-factor of $g = 2.099(3)$ and $\chi_0 = 8.15(43) \times 10^{-5}\,\mathrm{erg\,G^{-2}\,mol^{-1}}$, assuming S = 1/2. This is about 4.5% above the averaged g-factor from X-band EPR, which is in close agreement and supports the prediction that the system can be described as a spin 1/2.

Together, the $M(B)$ and $M(T)$ measurements provide complementary information about the magnetic behaviour of the system. While the field-dependent measurements reveal deviations from the behaviour of an ensemble of non-interacting paramagnetic moments under applied magnetic fields, the temperature-dependent measurements highlight the emergence of magnetic interactions at low temperatures.

Table 4.3: Weiss temperatures Θ_W obtained from Curie–Weiss fits to the inverse susceptibility of $[Fe(HMB)_2][PF_6]$ using different fitting ranges. The reference fit range is 50 K to 250 K.

Fit range (K)	Θ_W (K)
50–250 (reference)	−6.5(2)
40–250	−5.8(2)
30–250	−4.9(2)
50–260	−6.9(2)
50–270	−7.3(2)

To investigate the low-temperature magnetic behaviour of $[Fe(HMB)_2][PF_6]$ in greater detail, additional measurements were performed using the ^{3}He option of the MPMS3, extending the accessible temperature range from the standard 1.8 K down to 0.4 K. This temperature regime was explored to determine whether the deviations from ideal paramagnetic behaviour become more pronounced at even lower temperatures. Figure 4.6 presents the previously discussed field-dependent isothermal magnetisation data alongside the 0.4 K isothermal magnetisation data, shown as a function of applied field in (a) and rescaled by temperature in (b). The 0.4 K dataset continues the trend established at higher temperatures, with a steeper initial slope in $M(B)$ and a more pronounced deviation from universal B/T scaling, providing further evidence for antiferromagnetic correlations. This is consistent with the negative

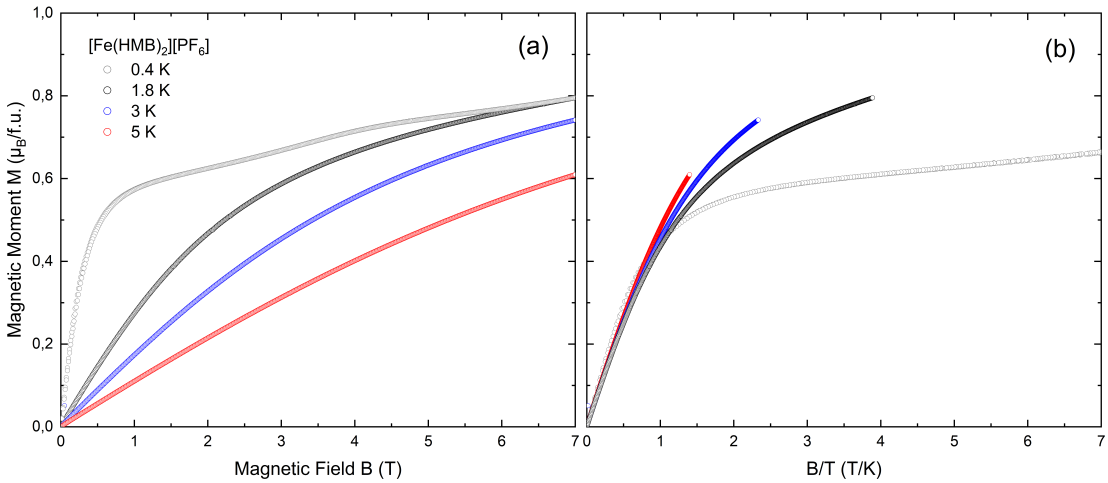


Figure 4.6: Field-dependent isothermal magnetisation of $[Fe(HMB)_2][PF_6]$ measured between 0 T and 7 T at temperatures of 0.4 K (grey), 1.8 K (black), 3 K (blue), and 5 K (red), shown in units of μ_B per formula unit. (a) Magnetic moment M as a function of applied field B. (b) The same data plotted as a function of B/T to assess scaling behaviour and deviations indicative of magnetic interactions.

Weiss temperature obtained from the Curie–Weiss analysis and the previously observed failure of the Brillouin function fit. Additionally, the 0.4 K data exhibit features in $M(B)$ that are absent at higher temperatures, which can be described as plateau-like and show antiferromagnetic coupling and a level crossing into a new magnetic ground state This may be indicative of magnetic frustration arising from the geometric arrangement of the Fe(I) centres.

To further investigate the plateau-like features, the field derivative $\mathrm{d}M/\mathrm{d}B$ was calculated and is shown in Figure 4.7. $\mathrm{d}M/\mathrm{d}B$ exhibits a maximum, corresponding to the plateau step in $M(B)$. To assess whether geometric frustration could account for the observed features, the crystallographic structure was examined for triangular arrangements of the Fe(I) centres. Triangular motifs were identified in the (011) and (101) planes of the crystal structure, as shown in Figure 4.8. This observation, in combination with the $M(B)$ data, leads to the attribution of the observed behaviour to geometrical magnetic frustration.

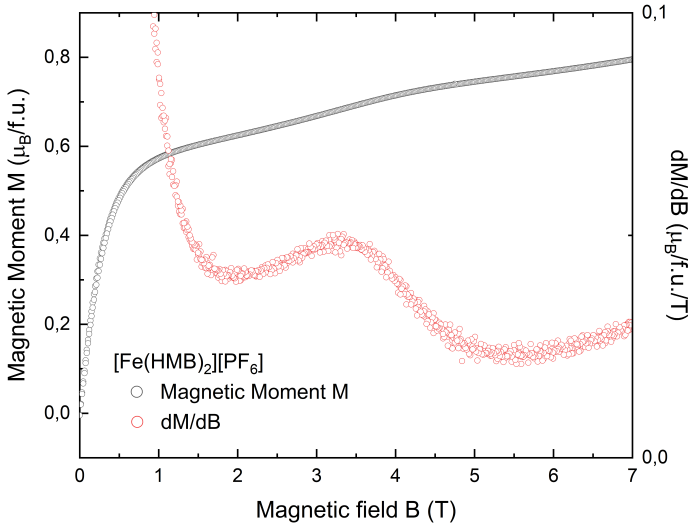
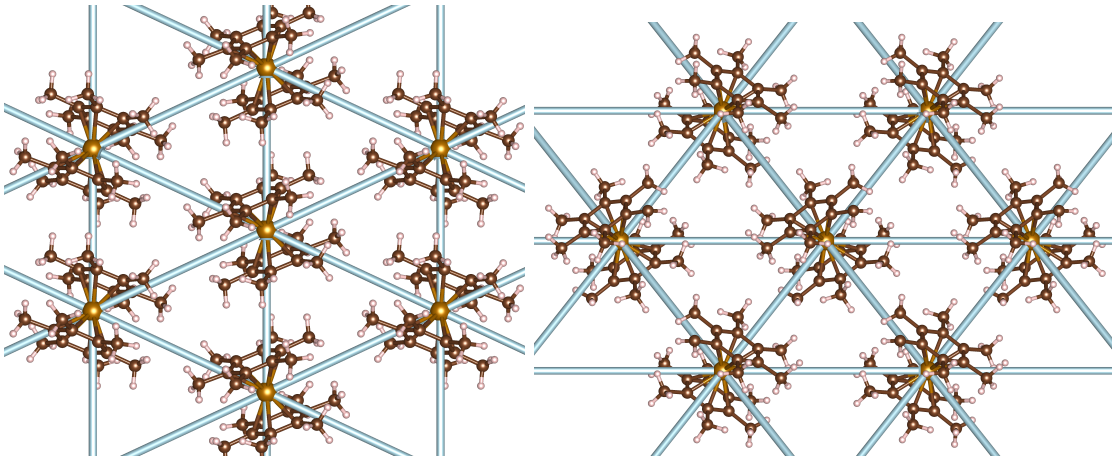


Figure 4.7: Isothermal magnetisation and its Derivative $\mathrm{d}M/\mathrm{d}B$ of $[\mathrm{Fe(HMB)_2}][\mathrm{PF_6}]$ measured at 0.4 K using the ^{3}He option.

In addition to the field-dependent measurements, the temperature dependence of the magnetisation was measured between 0.4 K and 4 K. The antiferromagnetic interaction becomes even clearer at these low temperatures, which can be observed in the low temperature end of the susceptibility data. The resulting magnetic susceptibility and corresponding inverse susceptibility data are shown in Figure 4.9, alongside the previously discussed data. A pronounced feature is observed near 1.8 K. This feature coincides with the transition between the ^{3}He and ^{4}He operating regimes of the instrument and is, therefore, attributed to the measurement system rather than an intrinsic property of the sample.



(a) (011) (b) (101)

Figure 4.8: Crystallographic planes of the solid state crystal structure of $[Fe(HMB)_2][PF_6]$, in which triangular lattice motifs were found.

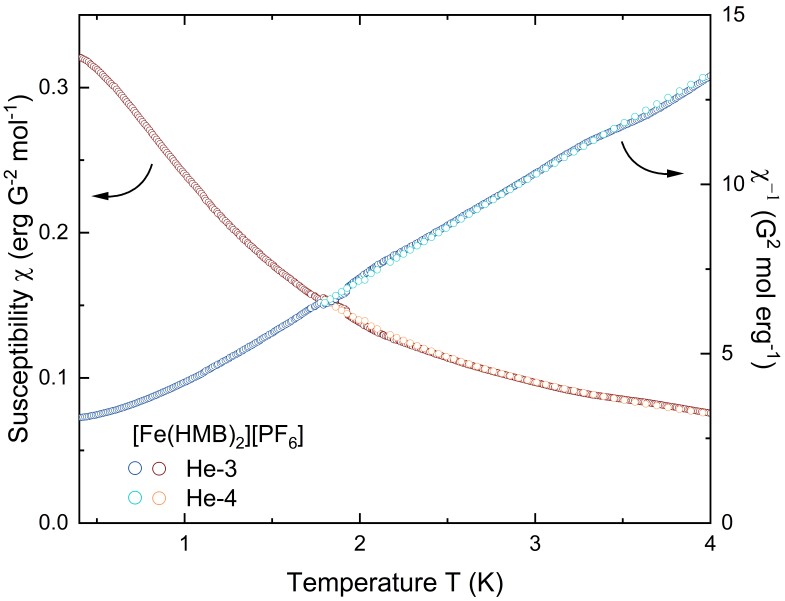


Figure 4.9: Temperature dependence of the susceptibility $\chi(T)$ and inverse susceptibility $\chi^{-1}(T)$ of $[Fe(HMB)_2][PF_6]$ measured from 0.4 K to 4 K.

4.3 $[Fe(HMB)_2][Al(OR^F)_4]$

The DC magnetisation of $[Fe(HMB)_2][Al(OR^F)_4]$ was measured as a function of applied magnetic field in the range of 0 T to 7 T at temperatures of 1.8 K, 3 K, and 5 K. The data were normalised to sample mass and molar mass and are presented in units of μ_B per formula unit in Figure 4.10(a). The 1.8 K dataset exhibits the steepest initial slope, followed by the 3 K and 5 K curves, with the 1.8 K data appearing to approach saturation near 0.9 μ_B. This slight reduction below the expected saturation value of 1 μ_B may reflect a systematic error in the sample mass determination, for instance due to residual solvent. The data are in good agreement with the Brillouin function (Equation (2.11)), and a simultaneous fit to all three isotherms yields $g = 2.072(2)$ and $S = 0.4403(5)$ with χ_0 fixed to zero, once again supporting the prediction of $S = 1/2$.

The M(B) data were additionally plotted as a function of the magnetic field rescaled by temperature in Figure 4.10(b). In contrast to $[Fe(HMB)_2][PF_6]$, the three datasets collapse onto a single universal curve, consistent with the absence of significant magnetic interactions and anisotropy.

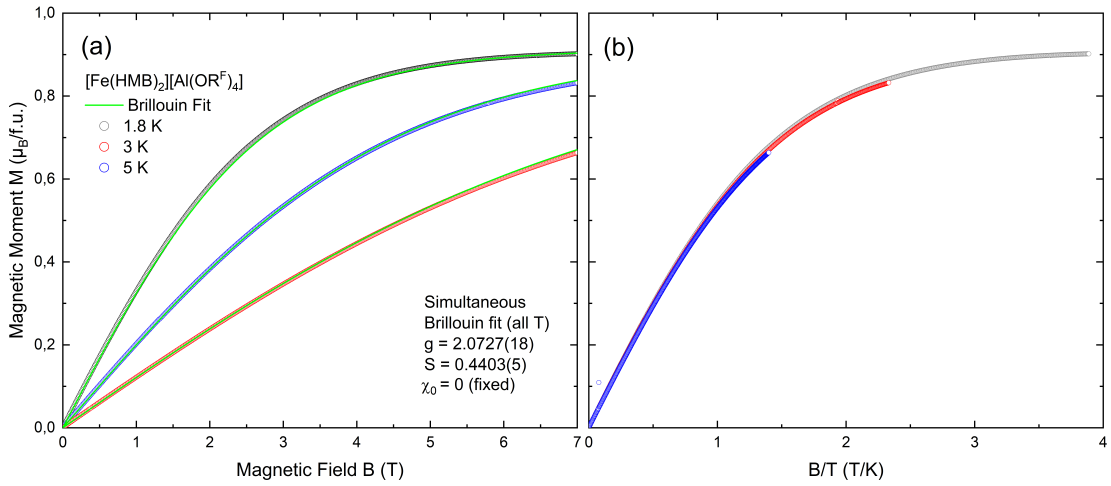


Figure 4.10: Field-dependent isothermal magnetisation of $[Fe(HMB)_2][Al(OR^F)_4]$ measured between 0 T and 7 T at temperatures of 1.8 K (black), 3 K (blue), and 5 K (red), shown in units of μ_B per formula unit. (a) Magnetic moment M as a function of applied field B. (b) Magnetic moment with the field axis rescaled by temperature.

Temperature-dependent magnetisation measurements were recorded at an applied magnetic field of 1 T. From this measurement, the molar magnetic susceptibility χ was calculated and plotted alongside the inverse susceptibility χ^{-1} in Figure 4.5. The temperature dependence of χ^{-1} is consistent with Curie–Weiss behaviour, and the Curie–Weiss law was fit to the inverse susceptibility in the range 50 K to 250 K, where the Curie–Weiss law is applicable. The

Weiss temperature for this fit was fixed to zero, as the $M(B)$ measurements indicated non-interacting paramagnetic behaviour with no evidence of significant exchange interactions. The best fit yields $g = 1.9570(3)$ and $\chi_0 = -3.280(51) \times 10^{-5}\,\mathrm{erg\,G^{-2}\,mol^{-1}}$ assuming $S = 1/2$.

More surprising is the negative χ_0 offset, which contrasts with the positive temperature-independent contribution commonly associated with Van Vleck paramagnetism. This cannot be explained by an error through the instrument or the sample preparation, as the same device, sample holder type and preparation routine were employed for all samples and $[Fe(HMB)_2][PF_6]$ does not exhibit this behaviour under identical conditions. The negative offset is therefore assumed to be an intrinsic property of this compound. This also indicates that its strength is larger than the Van Vleck paramagnetic contribution, as the net temperature-independent susceptibility contribution is negative. The $M(T)$-derived g-factor is in reasonable agreement with the value obtained from the $M(B)$ fit, $g = 2.072(2)$, with the deviation of approximately 5.6 % likely associated with the negative χ_0 offset.

Overall, it can be concluded that this sample, which has larger inter-atomic distances between the Fe(I) ions than $[Fe(HMB)_2][PF_6]$, exhibits no significant magnetic interactions, in contrast to the behaviour observed in $[Fe(HMB)_2][PF_6]$.

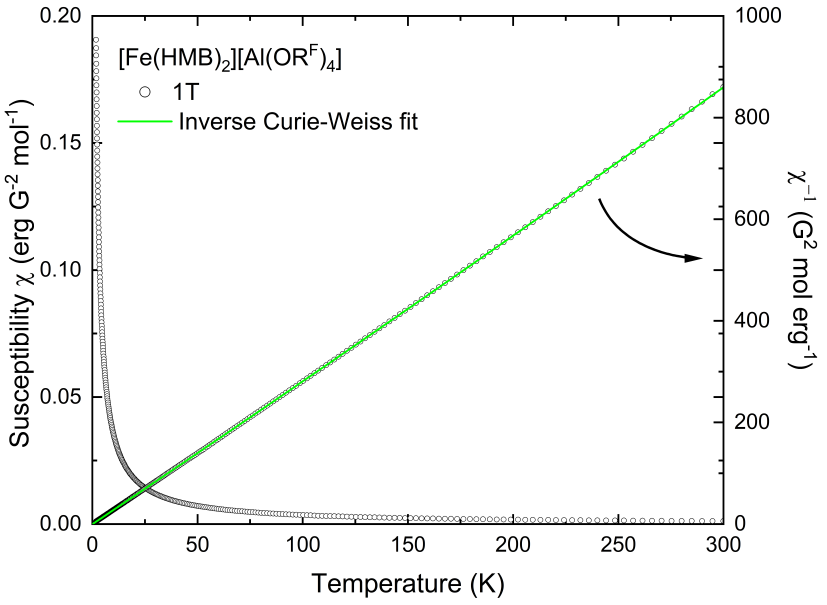


Figure 4.11: Temperature dependence of the molar magnetic susceptibility $\chi(T)$ and inverse susceptibility $\chi^{-1}(T)$ of $[Fe(HMB)_2][Al(OR^F)_4]$ measured at an applied field of 1 T. The solid green line represents a Curie–Weiss fit to $\chi^{-1}(T)$ in the high-temperature region.

4.4 $[Fe(HMB)_2][B(Ar^F)_4]$

Analogous to the first two samples, the microwave absorption of $[Fe(HMB)_2][B(Ar^F)_4]$ was measured as a function of applied field at 75 K. Analysis of the first derivative of the absorption spectrum yielded the anisotropic g-tensor

$$g = \begin{pmatrix} 2.080 & 0 & 0 \\ 0 & 1.997 & 0 \\ 0 & 0 & 1.872 \end{pmatrix}, \tag{4.2}$$

with an RMS average g-factor of $g_{\mathrm{RMS}} = 1.985$. The DC magnetisation of $[Fe(HMB)_2][B(Ar^F)_4]$ was measured as a function of applied magnetic field in the range of 0 T to 7 T at temperatures of 1.8 K, 3 K, and 5 K. The data were normalised to sample mass and molar mass and are presented in units of μ_B per formula unit in Figure 4.12(a). The 1.8 K dataset exhibits the steepest initial slope, followed by the 3 K and 5 K curves, with the 1.8 K data reaching saturation at 1.0 μ_B, in excellent agreement with the expected value for a spin-1/2 system with $g \approx 2$. The data are in good agreement with the Brillouin function for an ideal paramagnet, and a simultaneous fit to all three isotherms yields $g = 2.0271(12)$ and $S = 0.4954(4)$ with χ_0 fixed to zero. The extracted g-factor is in good agreement with the EPR value of $g = 1.985$, with a deviation of approximately 2.1 %. The M(B) data were additionally plotted with the magnetic field axis rescaled by temperature in Figure 4.12(b). The three datasets collapse onto a single universal curve, consistent with the absence of significant magnetic interactions and anisotropy.

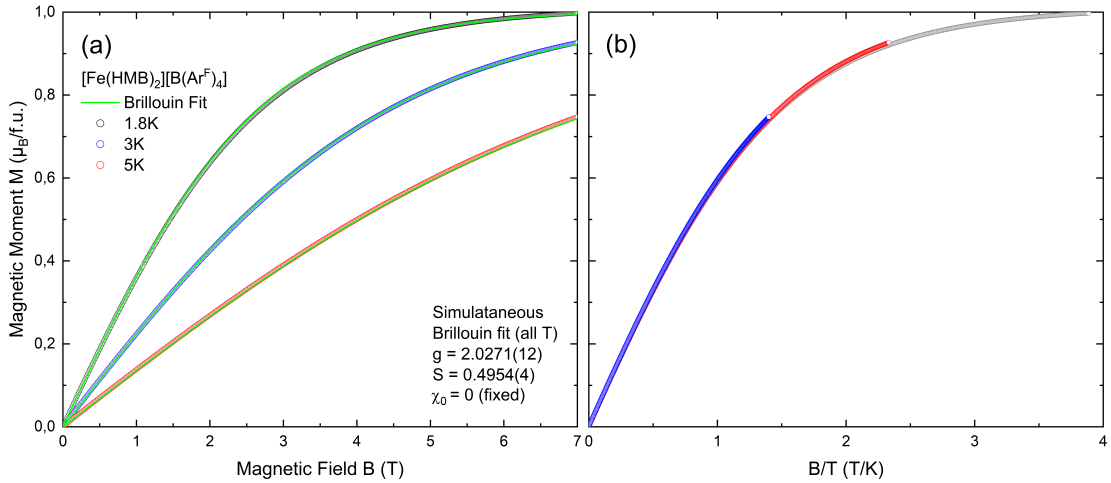


Figure 4.12: Field-dependent isothermal magnetisation of $[Fe(HMB)_2][B(Ar^F)_4]$ measured between 0 T and 7 T at temperatures of 1.8 K (black), 3 K (blue), and 5 K (red), shown in units of μ_B per formula unit. (a) Magnetic moment M as a function of applied field B. (b) Magnetic moment with the field axis rescaled by temperature

Temperature dependent magnetisation measurements were recorded at applied magnetic fields of 0.1 T and 1 T. From these measurements, the molar magnetic susceptibility χ was calculated and plotted alongside the inverse susceptibility χ^{-1} in Figure 4.13. Although both datasets exhibit similar behaviour, the susceptibility curves obtained at 0.1 T and 1 T do not fully overlap, indicating the presence of additional field-dependent contributions. This offset may originate from several sources, including sample holder contributions, remanent magnetic fields of the magnet, impurities or sample degradation. The temperature dependence of χ^{-1} is consistent with Curie–Weiss behaviour, and the Curie–Weiss law was fit to the inverse susceptibility in the range 50 K to 250 K. The Weiss temperature was fixed to zero, consistent with the absence of significant magnetic interactions shown by the $M(B)$ data. The Curie–Weiss fit of the 1 T data yielded $g = 2.107(1)$ and $\chi_0 = 2.758(17) \times 10^{-4}\,\mathrm{erg\,G^{-2}\,mol^{-1}}$, assuming $S = 1/2$, further supporting the $S = 1/2$ ground state prediction. The positive temperature-independent offset χ_0 is attributed to Van Vleck paramagnetism. The $M(T)$-derived g-factor exceeds both the EPR value of $g = 1.985$ and the $M(B)$ result of $g = 2.0271(12)$, with deviations of 6.2 % and 4.0 % respectively. As the Van Vleck contribution is explicitly accounted for via χ_0 in the $M(T)$ fit, the discrepancy with the $M(B)$ is attributed to the χ_0 fixed to zero in the $M(B)$ Brillouin fit.

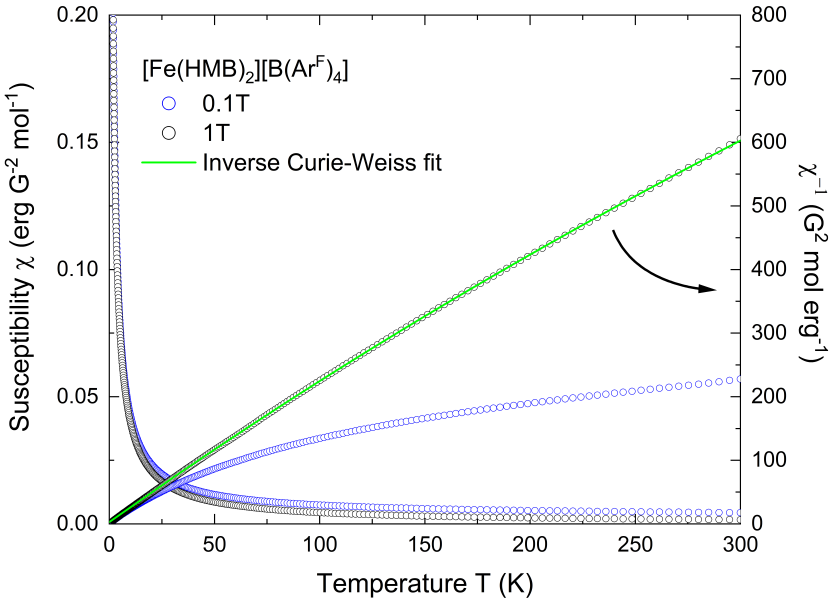


Figure 4.13: Temperature dependence of the molar magnetic susceptibility $\chi(T)$ and inverse susceptibility $\chi^{-1}(T)$ of $[Fe(HMB)_2][B(Ar^F)_4]$ measured at applied fields of 0.1 T (blue) and 1 T (black). The solid green line represents a Curie–Weiss fit to $\chi^{-1}(T)$ in the high-temperature region.

4.5 Comparative Analysis and Discussion

The magnetic properties of the three Fe(I) samples are compared in the following to establish the relationship between the Fe(I) ion separation and the magnetic interactions. Figure 4.14 presents the isothermal magnetisation rescaled by temperature of all three measured Fe(I)-based compounds, including sub-Kelvin ^{3}He data for $[Fe(HMB)_2][PF_6]$. The data of $[Fe(HMB)_2][PF_6]$, which were measured at different temperatures, do not collapse onto a single universal curve, indicative of magnetic interactions, while the data for the other two samples collapse onto a single universal curve, consistent with the behaviour of an ensemble of non interacting paramagnetic moments. This contrast correlates with the intermolecular Fe(I) ion distances, shown in Table 4.1. The magnetic interactions appear only in the compound with the shortest distances between the iron centres, proving the hypothesis that the interaction is sensitive to the spatial separation of the magnetic centres.

A further difference appearing in this plot is the difference in saturation magnetisation between $[Fe(HMB)_2][Al(OR^F)_4]$ and $[Fe(HMB)_2][B(Ar^F)_4]$. As the magnetic ion (Fe(I)) is the same, both should show the same saturation, expected to be $1\mu_B$. The saturation magnetisation of $[Fe(HMB)_2][B(Ar^F)_4]$ agrees with this perfectly, while $[Fe(HMB)_2][Al(OR^F)_4]$ deviates slightly from the expected value. This is most likely attributable to a systematic error in the sample mass determination, possible due to residual solvent in the sample.

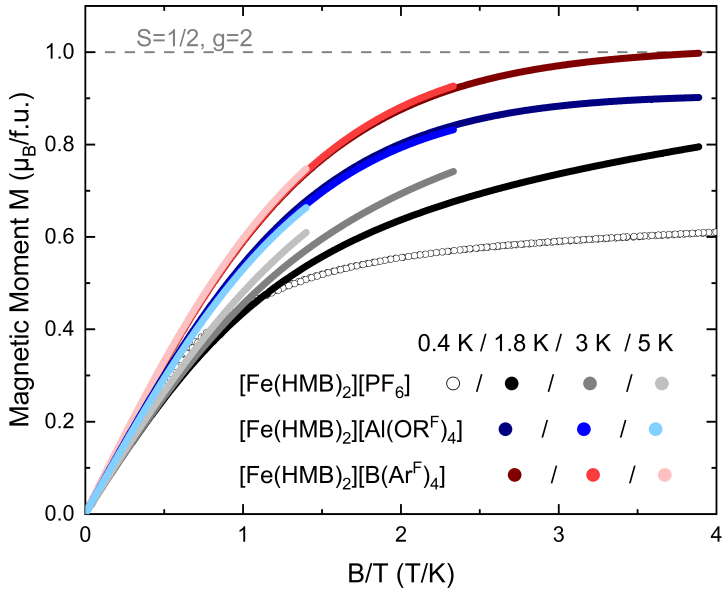


Figure 4.14: Field-dependent isothermal magnetisation of all samples with the field axis rescaled by temperature, including sub-Kelvin ^{3}He data for $[Fe(HMB)_2][PF_6]$. The dashed line indicates the saturation magnetisation expected for a spin-1/2 system with $g = 2$.

The temperature dependence of the molar susceptibility and inverse susceptibility for all three samples, measured at 1 T, is shown in Figure 4.15. The 1 T data were chosen as this field provides a higher signal-to-noise ratio while the magnetisation remains well below saturation, ensuring that the magnetic response is still approximately linear over most of the investigated temperature range. All three compounds exhibit Curie–Weiss behaviour at high temperatures. The negative Weiss temperature of $[Fe(HMB)_2][PF_6]$ is consistent with antiferromagnetic interactions, as identified from the $M(B)$ and B/T analysis, while the remaining two compounds yield satisfactory fits with Weiss temperatures fixed to zero, supporting the absence of significant interactions.

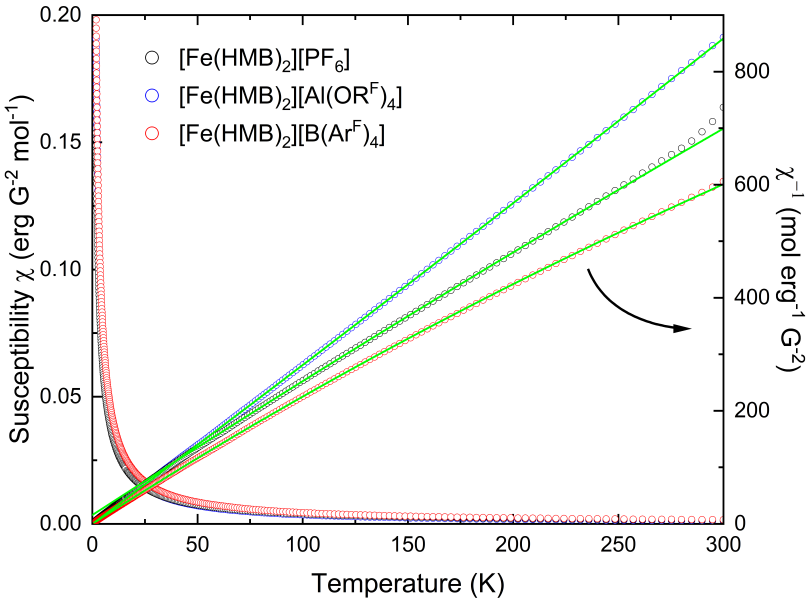


Figure 4.15: Temperature dependence of the molar magnetic susceptibility $\chi(T)$ and inverse susceptibility $\chi^{-1}(T)$ of all samples measured at 1 T. Curie–Weiss fits to $\chi^{-1}(T)$ in the high-temperature region are shown as green solid lines.

The g-factors obtained from the fits of the Curie–Weiss law are in good agreement with the value expected for a $S = 1/2$ centre across all three compounds. Further comparison of the g-factors obtained from EPR spectroscopy and from the fits to the magnetometry data (see Table 4.4) reveals method-dependent variations in the order of 4 % to 6 %. EPR spectroscopy provides a more direct and precise determination of the g-factor, as SQUID-magnetometry is susceptible to systematic distortions arising from incomplete background subtraction, impurity contributions, the dependence on the accuracy of the sample mass, and deviations from ideal Curie behaviour. All of these could lead to deviations of the fitted g-factor. The $M(T)$-derived values tend to exceed the EPR values, consistent with a positive offset from residual paramagnetic impurities or temperature-independent contributions that

were not fully accounted for in the fit. The observed differences in the g-factors highlights the importance of combining complementary experimental techniques in the characterisation of the magnetic properties of a system. EPR spectroscopy serves as the more reliable reference for the g-factor here.

Table 4.4: Comparison of the g-factors determined by X-band EPR spectroscopy and by SQUID magnetometry. The EPR values are given as the RMS average of the anisotropic g-tensor, while the magnetometry values are obtained from fits to the $M(B)$ and $M(T)$ data.

	EPR	SQUID	
Sample	RMS-average	$M(B)$ fit	$M(T)$ fit
$[Fe(HMB)_2][PF_6]$	2.008	–	2.099(3)
$[Fe(HMB)_2][Al(OR^F)_4]$	–	2.072(2)	1.957(1)
$[Fe(HMB)_2][B(Ar^F)_4]$	1.985	2.027(1)	2.107(1)

A further observation, though not directly relevant to the magnetic characterisation of the Fe(I) compounds, is the appearance of a pronounced maximum in χT around 50 K in all samples (Figure 4.16). Since this feature is similar across chemically distinct compounds, it is attributed to trace oxygen contamination, which in its condensed solid form undergoes magnetic phase transitions around 50 K [47, 48], producing characteristic anomalies in the magnetic susceptibility [49]. Notably, this signal persists despite sample preparation and storage under inert atmosphere in an argon glovebox, suggesting that even trace oxygen exposure during transfer or mounting is sufficient to produce a detectable artefact in this susceptibility regime.

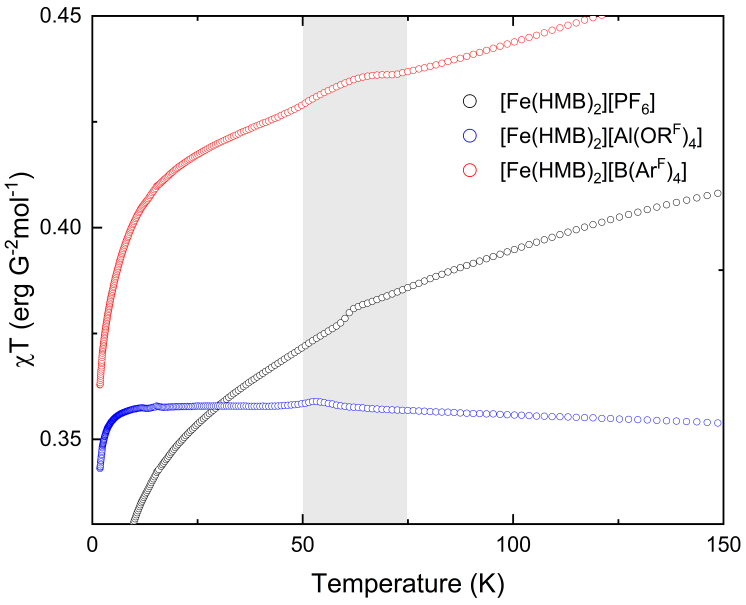


Figure 4.16: Temperature dependence of χT for all Fe(I) samples measured at 1 T. The pronounced maximum near 50 K is attributed to trace oxygen contamination. The grey region highlights the range in which this peak was observed across all three samples.

5 Development, Characterisation and Application of Custom Low-Background 3D-Printed Sample Holders

The reliable measurement of weakly magnetic samples using SQUID magnetometry remains an experimental challenge, primarily due to background contributions from the sample holder. This chapter addresses this limitation by developing a custom, low-background, 3D-printed sample holder intended for use with background subtraction software. The implementation of such a measurement approach requires careful design optimisation, systematic error analysis and iterative refinement of the experimental settings and data evaluation. A key aspect of the development is the validation of the 3D-printed sample holder using reference samples, to ensure quantitative reliability and reproducibility of the results. Once established, the resulting setup enables precise and reliable measurements of weakly magnetic samples.

5.1 Design Process and Magnetic Characterisation of the Custom Sample Holder

5.1.1 Evaluation of Current Options

Given the high sensitivity of the MPMS3, one can measure magnetisations in a range where even the contributions from the sample environment significantly affect the signal. This requires careful control of the magnetic background and geometric reproducibility of all components that are not part of the sample. A straightforward approach to minimise background contributions is the use of materials with intrinsically low magnetic susceptibilities [50]. Quartz and fused silica, both consisting of silicon dioxide (SiO_2), are widely employed for this purpose due to their low magnetic susceptibility. Both materials exhibit similar diamagnetic volume susceptibilities of approximately $\chi_V \approx -1.2 \times 10^{-5}$ (SI), corresponding to a molar susceptibility of approximately $-2.1 \times 10^{-5}\,\mathrm{erg\,G^{-2}\,mol^{-1}}$ [42, 51, 52]. Their temperature-independent and weakly diamagnetic response makes them well suited for the fabrication of SQUID sample holders (see Section 3.1.2). These are primarily useful for bulk or single-crystal samples mounted using simple mechanical or adhesive fixation. However,

while quartz-based sample holders show excellent magnetic properties, they are not suitable for powdered samples. These require enclosed sample volumes that tightly enclose them, to ensure reproducible positioning and to prevent sample loss during measurements. The fabrication of such complex quartz geometries is technically challenging and costly. It can also introduce magnetic impurities, which are especially problematic when measuring weakly magnetic samples.

Another approach to reducing the sample holder's contribution relies on the sample holder having a constant cross-section throughout the detection coil region, so that the resulting background contribution cancels within the MPMS3 gradiometer. This is exploited by the standard brass sample holder supplied by Quantum Design (see Section 3.1.2), which tolerates a substantially higher absolute susceptibility of the material due to its geometry. This makes it ideal for samples that can be snapped into place or fixed with a small amount of low-temperature-compatible glue. For powdered samples, the same complication arises as with quartz, since the powder must be contained, in this case in plastic capsules. The ones sold by Quantum Design are injection-moulded polypropylene (Formolene 4100N) parts that snap into the brass half-tube sample holder. Due to their geometry, these capsules produce a substantial, diffuse background signal that renders them unsuitable for weakly magnetic samples.

An alternative approach is provided by additive manufacturing, in particular SLA 3D-printing. This technique enables precise fabrication of complex geometries with smooth surfaces and precise tolerances. This significantly expands the design possibilities for sample holder geometries. Compared to other additive manufacturing techniques like filament-based 3D-printing, SLA achieves superior spatial resolution and higher structural homogeneity, both of which are critical for SQUID sample holders. Modern photopolymer resins used in SLA typically do not contain ferromagnetic fillers and exhibit weak diamagnetic volume susceptibilities in the order of 1×10^{-6} to 1×10^{-5} (SI), which is generally slightly larger in magnitude than that of quartz [42]. However, SLA-printed components also show a non-negligible magnetic background that can be comparable in magnitude to the signal from weakly magnetic samples. This requires an additional strategy to reduce the sample holder contribution. A common approach is based on background subtraction, where the signal of the empty sample holder is measured independently and subtracted from the total signal [53]. While this approach is theoretically applicable to most setups, practically it is sensitive to repositioning and reproducibility errors. These are commonly encountered with the capsules for the Quantum Design brass holder. They exhibit small geometric variations and material inhomogeneities, and are difficult to reposition with sufficient precision between sample and background measurements. Even slight differences in radial alignment or axial positioning in the gradiometer of the magnetometer lead to systematic errors in the extracted magnetic moment. These errors become especially significant for weakly magnetic samples, with magnetic moments in the range $1 \times 10^{-8}\,\mathrm{erg\,G^{-1}}$ to $1 \times 10^{-6}\,\mathrm{erg\,G^{-1}}$. For these reasons, a custom-designed 3D-printed sample holder remains the most promising solution.

5.1.2 Design Considerations

The design process was guided by a few core principles for low-background SQUID sample holders, which were derived from established knowledge of the magnetic background contributions and the working principles of SQUID magnetometry [10, 54, 55]. These considerations address the symmetry and geometry of the sample holder and sample volume, as well as reproducibility and airtightness. These are discussed individually in the following sections.

Axial Symmetry

Axial symmetry refers to the symmetry of the sample holder's design along the measurement axis with the centre of symmetry being the sample volume. In the second-order gradiometer a uniform sample holder produces no net signal, as the contributions from different coil sections cancel out (see Section 3.1.2). This can be exploited by symmetrically placing identical counterparts of the required structures around the sample volume. In practice, however, this is not perfectly achievable due to slight manufacturing differences. Therefore, deviations from this ideal case appear, leading to an incomplete cancellation. The effect of this is most pronounced at sharp edges with large volume differences and is referred to as end effects [1]. Structural inhomogeneities such as threaded interfaces are therefore placed outside the scan window and arranged symmetrically around the sample volume. Overall, deviations from ideal symmetry or homogeneity can produce residual signals, showing that the geometry of the sample holder directly influences both the magnitude and reproducibility of low-signal magnetisation measurements.

Radial Symmetry

Radial symmetry of the sample holder around the sample axis ensures that the magnetic response of the holder is invariant under rotation around the scan axis. This is particularly important as the SQUID detection system is sensitive not only to the magnitude of the magnetic moment but also to its spatial distribution within the gradiometer detection coils. Deviations from radial symmetry can lead to inconsistencies in the reproduction of the background signal when the sample holder is removed and reinserted between background and sample measurements with a different angular orientation. Since the coupling to the gradiometer coils depends on the radial position of the magnetic moment, such rotations alter the measured signal even for identical bulk susceptibility [56]. This is particularly relevant for weakly magnetic samples, where the sample signal is comparable to residual background contributions.

Radial Centring

Radial centring refers to the alignment of the sample along the central axis of the detection coils. Unlike the geometric symmetry discussed in the previous sections, which is a design property, radial centring is an experimental condition that depends on insertion reproducibility. This can nonetheless be improved through careful design. Radial offsets introduce asymmetric coupling to the detection coils and thereby cause systematic errors in

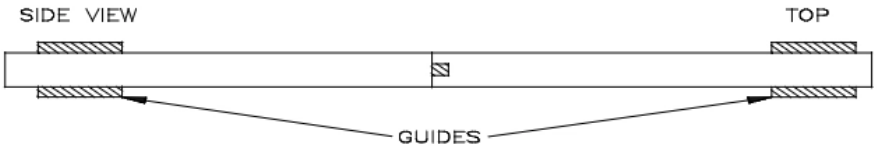


Figure 5.1: Schematic representation of a sample holder with a centrally positioned sample volume. Guide structures are symmetrically placed outside the measurement region to ensure reproducible radial centring of the sample holder. Taken from [57].

the extracted magnetic moment [56]. These errors are particularly pronounced for samples with large spatial extent or for weak signals. To ensure reproducible positioning, mechanical guide structures can be incorporated at the ends of the sample holder, outside the detection region of the magnetometer. These guides may consist of spacers made out of a weakly magnetic material or can be integrated in the 3D-model. For the MPMS3 bore diameter of approximately 9 mm, guide elements should be kept below 8 mm to avoid friction during insertion and extraction [57].

Geometry of the Sample Volume

For the application of the point-dipole approximation used for fitting in the data analysis, the sample shape should ideally be point-like. Practically, this means that the sample volume should not be long in the direction of the measurement axis. Additionally, it should be radially symmetrical, for the same reasons as the radial symmetry of the whole sample holder stated previously. Ideally the sample volume should be designed to mimic the geometry of the Quantum Design palladium reference sample. This ensures the reliable use of the standard MPMS fitting routine, which is based on calibrations made with this reference sample.

Airtightness of the Sample Volume

Many samples are air-sensitive and must be handled under inert conditions. Therefore, it is essential to provide an airtight seal to prevent the degradation or contamination of the sample during handling and measurement. At the same time, this airtight seal prevents the loss of powdered samples. Airtightness can be achieved by designing components that fit tightly around the sample volume, for example by exploiting the elasticity of the cured resin to enable a range of closing mechanisms without introducing additional sealing components. Because no additional parts are required in this approach, it preserves the low magnetic background of the sample holder while ensuring sample integrity. The reliability of this seal depends on the manufacturing tolerances. The SLA printing process introduces small dimensional variations, which should be accounted for in the design process to ensure a reliable seal.

5.1.3 Design Process

The sample holder was designed through numerous iterations, guided by mechanical considerations and magnetic performance. This iterative approach was enabled by SLA manufacturing, which provides fast prototyping and easy modification of previous designs. The evolution of the design progressed through four main steps: solid rod prototypes (V0.X), snap-fit designs (V1.X), thin cylindrical designs (V2.X), and compression-based designs (V3.X). While not all designs were used for measurement or further investigated, each iteration provides valuable insights into the overall geometry, the role of symmetry, the importance of accurate sample positioning and the impact of different complex structures on the magnetic background. The designs underwent iterative geometric refinement, with numerous incremental adjustments to fit, assembly, and background performance. Therefore, a comprehensive comparison of all iterations is deferred to Section 5.1.4, while the following sections focus on the most representative background measurements of each version.

Version 0: Solid Rod Prototype

The initial prototype (V0.1) consisted of a long solid rod designed to fit within the MPMS3 sample space and to connect to the sample transport rod via a standard threaded adapter (M4×0.75, class 6g). No sample volume was included at this stage. The primary objective was to evaluate the background signal of a geometrically uniform polymer structure and to confirm the dimensional compatibility of SLA-printed components with the MPMS3.

The first prints of this design exhibit a significant curvature due to uneven shrinkage during the curing process of the photopolymer. This phenomenon is commonly referred to as warping in the context of SLA fabrication. Systematic investigation revealed that long and thin structures require to be printed at a small angle relative to the z-axis (up to 5°) to ensure homogeneous curing within the printed part's cross-section. After adjusting the orientation of the printed parts and optimising support placement, warping was sufficiently suppressed to permit the insertion of the fully processed parts into the MPMS3 bore. Additionally, the successful fitting of the printed thread with the sample rod confirms that SLA printing delivers a sufficient dimensional accuracy for this application.

To facilitate the printing process, while reducing the amount of warping, the next version of the sample holder prototype was segmented into three parts that are connected by threaded

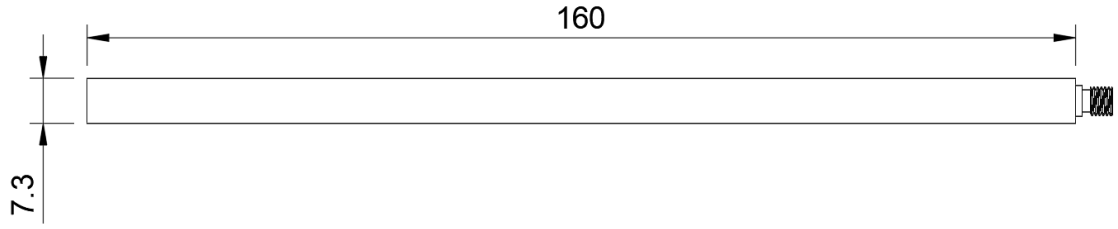


Figure 5.2: Schematic representation of the 3D-model of sample holder V0.1 including dimensions (in mm), employed in initial tests to assess compatibility with the MPMS3 as well as manufacturing quality and dimensional accuracy.

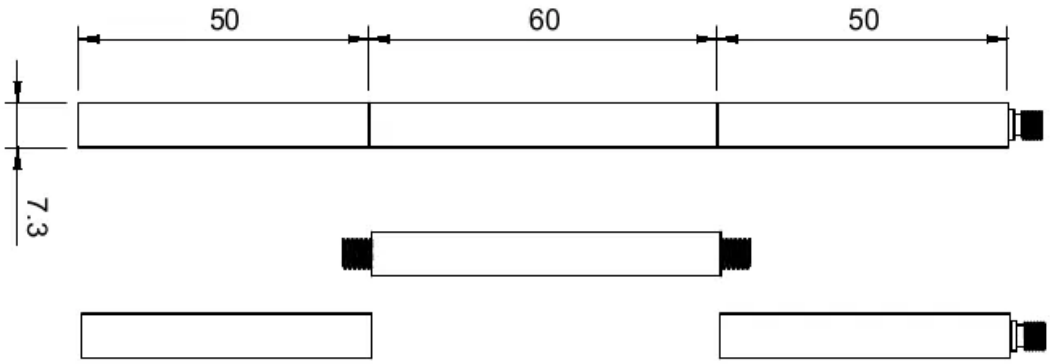


Figure 5.3: Schematic representation of the 3D-model of sample holder design V0.2, including dimensions (in mm), illustrating both the assembled and disassembled states of the design, which is composed of three components.

joints (V0.2). This split geometry still allowed the central section to be designed with sufficient length to move the threaded connection regions outside the sensitive measurement zone. All threaded connections and contact surfaces between printed parts are designed with a clearance of 0.2 mm to accommodate manufacturing tolerances and ensure reliable assembly, while minimising enclosed void volume that would increase the background signal.

After confirming dimensional fit, initial SQUID background measurements of the sample holder V0.2 were performed. These are the first measurements of the the 3D-printed parts and will be used to analyse subsequent design iterations. Measurements were carried out using DC scans with a scan length of 50 mm, two scans per field value, and a scan time of 4 s. The AutoCenter function was disabled to preserve a fixed measurement position. Applied fields of 0.1 T, 1 T, and 7 T were used. Measurements were performed at room temperature (300 K) and at low temperatures (100 K and 1.8 K) to assess the temperature dependence of the magnetic response and the mechanical stability of the cured resin at cryogenic temperatures, for which no data were available in the literature.

The results of the first measurements (Figure 5.4(a)) show a single scan at 300 K and 1 T. The scan exhibits almost flat behaviour from 15 mm to 40 mm and a 'dipole-like' feature symmetrically centred around 58.75 mm. The vertical line at 58.75 mm can be associated with the centre of the threaded connection between the middle and bottom parts, where a pronounced signal anomaly is evident and demonstrates that complex geometries introduce large localised contributions. In contrast, the region to the left of the thread exhibits a nearly constant signal corresponding to the solid part of the holder. This implies that by choosing the scan length such that the threaded regions fall outside the measurement window, their contribution becomes small. To further characterise this threaded region, the fitting function of the MPMS3 gradiometer (Equation (3.7)) was fitted to the measured signal, as shown in Figure 5.4(b)). The fit is approximate, as the threaded region is an extended and geometrically complex object rather than a point-like dipole, and the resulting deviation from the fitted curve reflects this limitation. Nevertheless, this contribution proves to be paramagnetic.

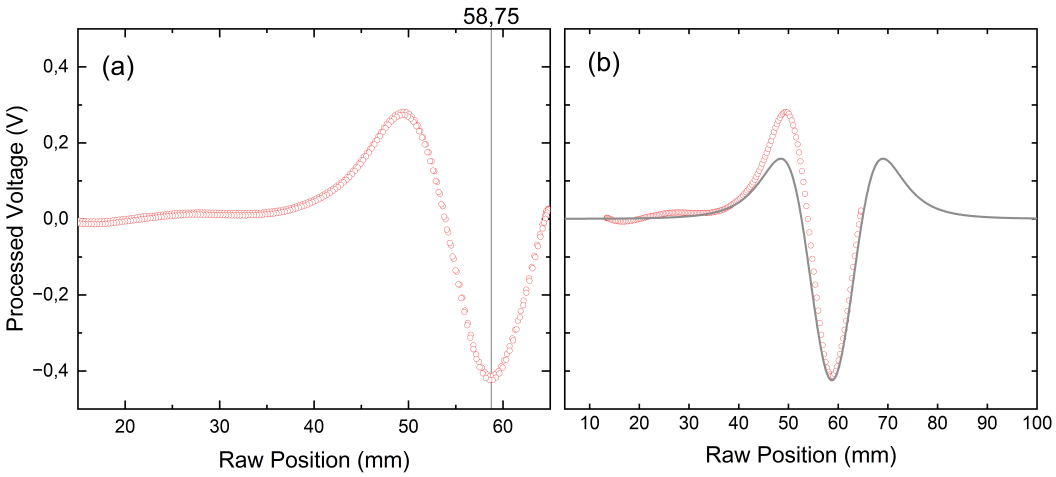


Figure 5.4: Background measurement of the 3D-printed solid rod (V0.2) at 300 K and 1 T. (a) Processed voltage as a function of scan position. (b) The same data including a dipole fit to the signal of the threaded region.

Next, measurements of the solid rod prototype were repeated at various fields and temperatures to asses the field and temperature dependent bahaviour. Figure 5.5 shows the DC scans at three temperatures at 1 T in (a) and for three different fields at 300 K are in (b). No significant difference was observed between measurements at room temperature and at 100 K, indicating that the cured photopolymer remains both mechanically stable and magnetically invariant in a wide temperature range. Only at very low temperatures (1.8 K), the signal substantially differs: the amplitude of the signal from the threaded region is higher and the data has a slight positive offset. The positive offset could be explained by an offset introduced by the SQUID electronics. The more significant difference is the change in amplitude of the thread signal. This can also be explained, as the thread of the print had to be slightly trimmed and thereby metal impurities were introduced. The DC scans at 300 K in fields of 0.1 T, 1 T, and 7 T reveal that the signal strength increases but the shape of the signal remains the same. This behaviour is consistent with the expected temperature-independent diamagnetic response of amorphous organic polymers. Based on these observations, all subsequent background characterisation measurements were performed at room temperature, significantly reducing measurement time.

As discussed above, the analysis of the DC scan profiles revealed a signal anomaly localised near 60 mm, which originates from the threaded connection between holder parts. At this stage, the design was not fully symmetrical around the gradiometer centre, leading to one of the threaded regions being inside the measurement region. Although unintended, the measurement of the threaded region confirms its relatively strong signal. This observation motivates the displacement of threaded interfaces outside the active scan range in subsequent designs.

The combined analysis of the design and printing process, together with the results of the initial measurements, provide the key practical constraints that guide the development of

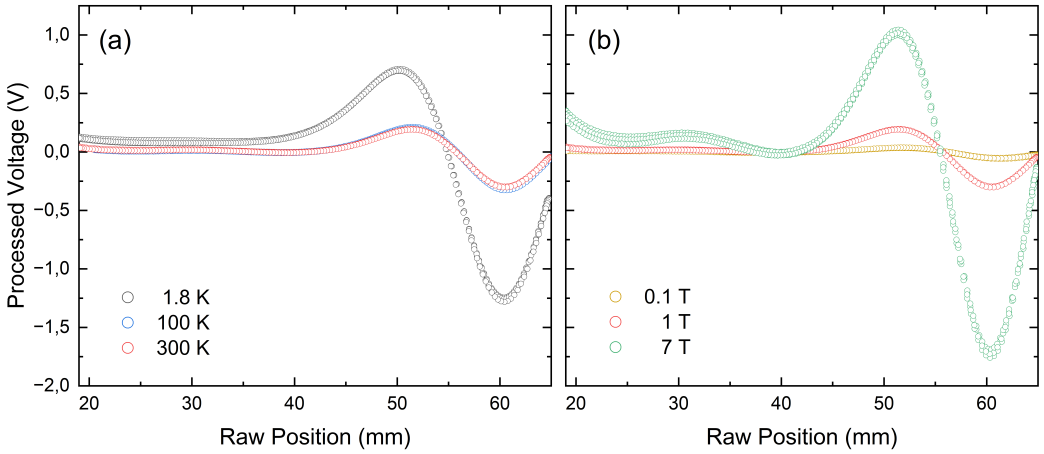


Figure 5.5: DC scans of the 3D-printed sample holder (V0.2). The left panel shows raw scan data recorded at a constant applied magnetic field of 1 T at temperatures of 1.8 K, 100 K, and 300 K. The right panel shows measurements performed at 300 K at applied magnetic fields of 0.1 T, 1 T, and 7 T.

subsequent holders. These identified constraints include the MPMS3 sample bore size, the dimensions of the threaded connection to the MPMS3 sample rod, the location of the centre position in the detection region and the impact of complex structures like threads and sample volumes on the measured signal. An essential observation is that the tolerance of 0.02 mm applied at the threaded joints was sufficient to ensure reliable, reproducible assembly across repeated fabrication runs.

Version 1: Snap Fit Sample Holder

Building on these constraints, the design process advanced to the snap fit sample holder. This is the first functional holder geometry that incorporated a defined sample volume, implemented by modifying the central section of the three-part solid rod prototype (V0.2). As a first test, a cubic volume of 2 mm edge length was used (V1.1). Access to the chamber was enabled by separating approximately one third of the holder body into an independent component, attached to the main structure via two thin flexible flaps, exploiting the elastic deformation of the cured photopolymer resin, that snap onto the main part. After the initial measurements ,which showed the overall fit of the parts and compatibility with the MPMS3, a more refined sample volume geometry was used. In V1.2 a cylindrical sample compartment with a diameter of 2.8 mm and a height of 3.8 mm was employed, which mimics the dimensions of the Quantum Design palladium reference sample. This design is shown in Figure 5.6.

The magnetic background of the sample holder with the initial square sample volume (V1.1) was analysed by a DC scan at 300 K and 1 T, shown in Figure 5.7. The threaded connection region at 58.75 mm produces the same localised anomaly as observed in the solid rod design

(V0.2). The sample volume, located 30 mm from the thread at 28.75 mm, introduces an additional signal feature of smaller magnitude. The signal profile in the vicinity of the sample volume deviates more strongly from an ideal dipole response than the threaded region alone, reflecting the additional geometric inhomogeneities introduced by the snap-fit component.

While this design provided reproducible axial sample positioning, other importantg concepts like radial symmetry and airtightness remained limited. The snap-fit interface introduced axial asymmetry into the overall sample holder design, and the mechanical closure did not provide reliable airtightness. The airtightness was assessed by placing approximately 5 mg of naphthalene in the sample volume of the sample holder, and observing the sample mass over several days by repeated weighing. Naphthalene is chosen for its known sublimation behaviour at room temperature and ambient pressure. The complete sublimation of the sample within a few days confirmed that this design is not airtight. Therefore it is not usable to retain fine powders or volatile samples, making this design suited to granular or non-volatile materials only.

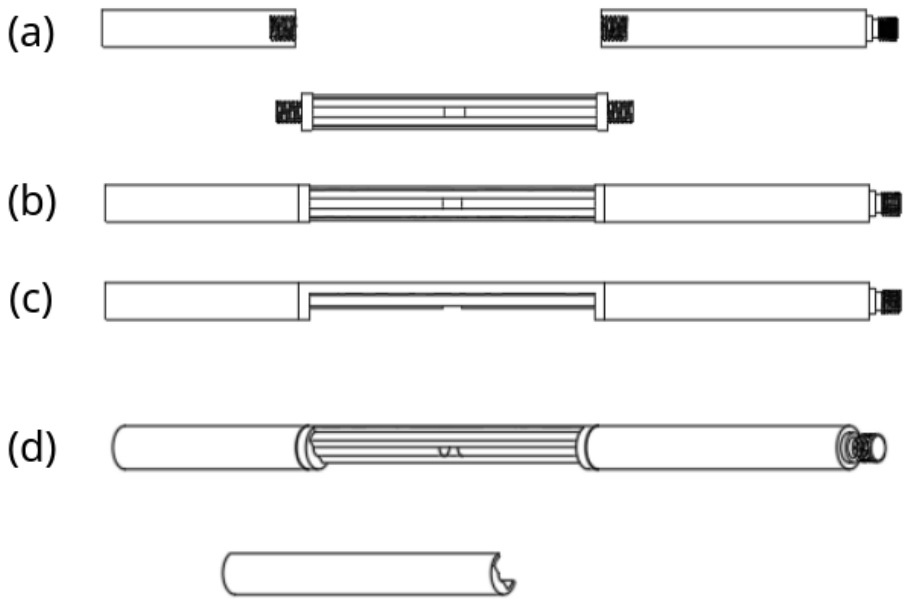


Figure 5.6: Schematic representation of the 3D-model of the sample holder V1.1, illustrating both the assembled and disassembled states. The three distinct parts of the main rod are shown in (a) from the top-down view, in (b) in the assembled state from the same view, and in (c) in the assembled state from the side view. Finally, (d) shows a 3D view of the assembled main rod and the lid to better visualise the snap fit mechanism.

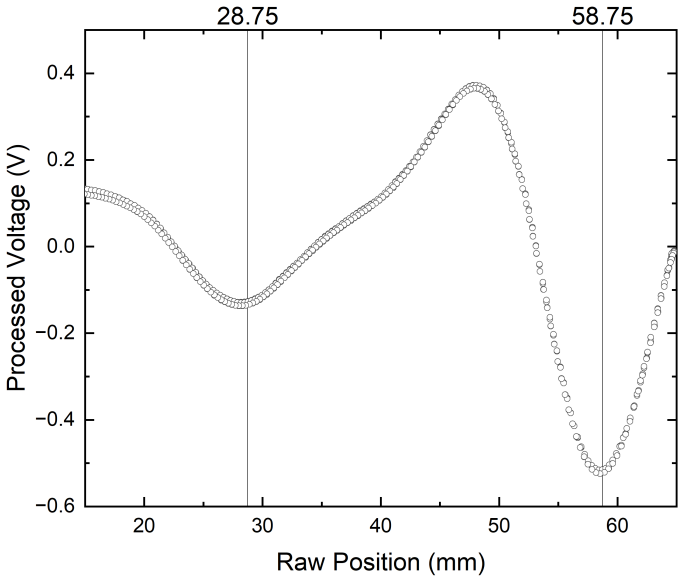


Figure 5.7: DC-Scans of the 3D-printed sample holder, snap-fit design V(1.1) with cubic sample volume, at 300 K and 1 T. The marked positions indicate the sample volume (28.75 mm) and the thread (58.75 mm).

Version 2: Thin Cylinder Sample Holder

The next design iteration aimed to improve radial symmetry and airtightness by adopting a fully radially symmetric geometry. The sample holder V2.1 consists of five components: a thin central tube forming the main holder body, an outer cylindrical sleeve, an enclosed sample chamber, and threaded top and bottom elements. This design is shown in Figure 5.8. Axial compression of the assembly was intended to seal the sample chamber while preserving radial symmetry. The magnetic background of this holder design, measured at 300 K and 1 T, is shown in Figure 5.9, once again showing a strong localised signal at 58.75 mm, and a second, weaker signal at 28.75 mm. As in the previous versions, the threaded region is the reason for the signal at 58.75 mm, while the sample volume is responsible for the signal at 28.75 mm. The sample volume signal manifests as a more strongly distorted dipole response compared to the earlier design, reflecting the increased geometric complexity of this version.

Summarising, the thin cylinder version provided an improved seal of the sample volume at the cost of a higher part count. The geometry is more radially symmetric than the previous iteration, though residual asymmetry remains due to the orientation of the pull-out sample cavity. This pull-out feature also introduces the risk of a radial sample offset, which distorts the measured signal. Overall, this version illustrates that improving a single design constraint, here radial symmetry, can introduce sufficient drawbacks to render the previous snap-fit design preferable.

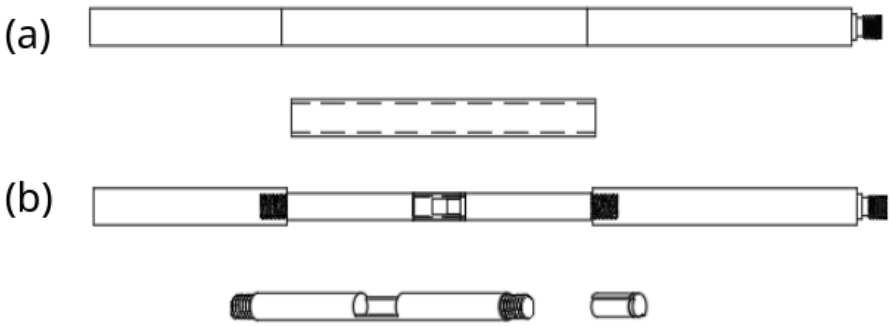


Figure 5.8: Schematic representation of the 3D-model of the sample holder V2.1, showing both the assembled (a) and disassembled (b) states of the design, with an additional focus on the central part containing the sample volume (c).

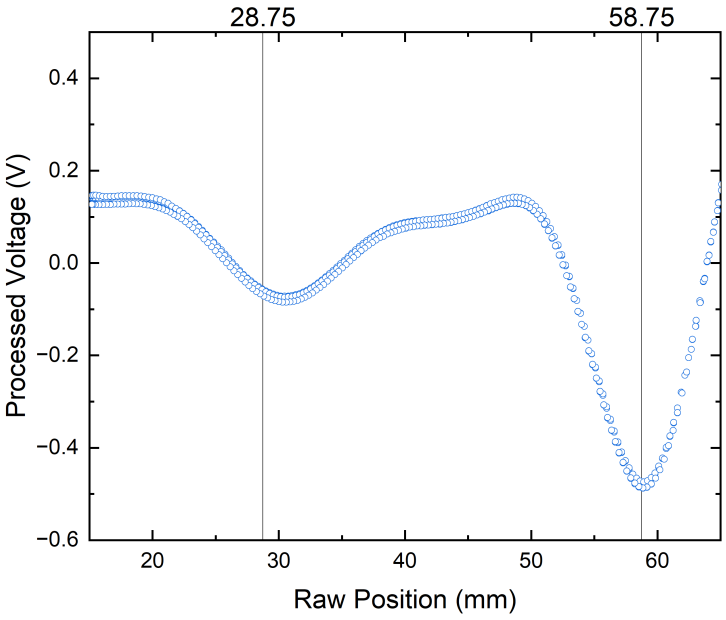


Figure 5.9: DC scans of the 3D-printed sample holder V2.1 at 300 K and 1 T. The marked positions indicate the sample volume (28.75 mm) and the thread (58.75 mm).

Version 3: Compression Sample Holder

Based on the limitations identified in the snap-fit (V1.X) and thin-cylinder (V2.X) designs, the final development stage focused on maximising radial symmetry and airtightness while minimising the number of components and interfaces within the SQUID detection region. The pronounced background distortions seen in V1.X and V2.X motivated a simplified geometry with fewer mechanical interfaces. The compression-based holder concept was developed in two successive iterations. The first implementation (V3.1, shown in Figure 5.10) features a three-part radially symmetric design. The bottom part forms the main holder body. Initially, its width is the same as that of the solid rod prototypes. After the threaded region, it transitions to a reduced width before terminating at the sample volume. The top part forms a matching structure that incorporates the sample volume plug and extends to the attachment screw, which connects to the MPMS3 sample rod. The two parts are joined by an outer hollow cylinder that provides threaded connections at both ends. In contrast to previous designs (V1.1 and V2.1), the central column is now split to incorporate the sample volume, which is sealed by compression upon tightening the outer hollow cylinder, which serves as the primary structural component. These changes significantly improved both axial symmetry and hermetic sealing compared to the snap-fit approach of versions V1.X, while maintaining reproducible sample positioning. However, the multi-part construction still introduces numerous mechanical interfaces, as shown in Figure 5.11, leading to a more complex signal within the active detection region.

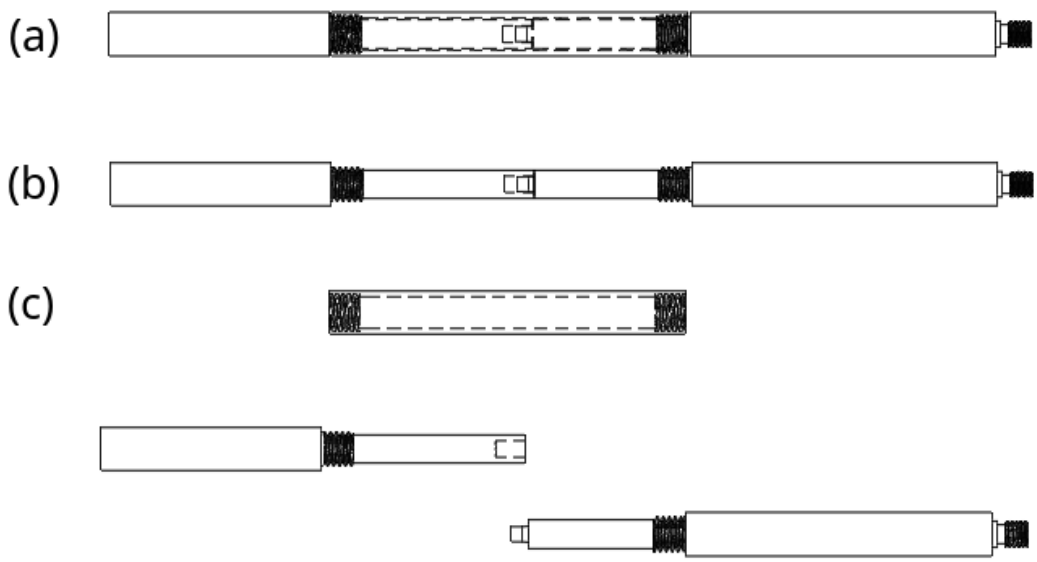


Figure 5.10: Schematic representation of the 3D-model of sample holder V3.1, illustrating both the assembled (a) and disassembled states (b), (c) of the design.

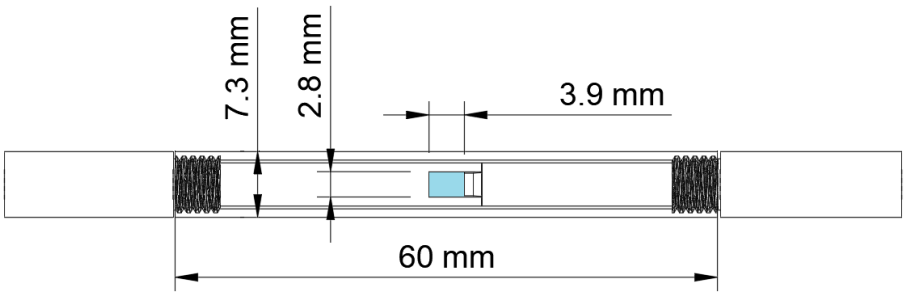


Figure 5.11: Detailed view of the central section of the sample holder V3.1, showing the dimensions of the sample volume, which is highlighted in blue.

The magnetic background of this holder design, measured at 300 K and 1 T, is shown in Figure 5.12, with the centre of the sample volume marked at 29 mm. The geometry of the design has been improved to move the threaded regions outside the measurement zones, as previously intended but slightly missed for V0.1, V1.1 and V2.1. This has been done by altering the length of the bottom part, which shifts the thread anomaly outside the measurement zone. The cylindrical sample volume produces a dipole-like response, which remains clearly identifiable despite superimposed background features from the surrounding holder geometry and a linear contribution intrinsic to the device.

Following systematic optimisation of the printing orientation, support structure placement, and post-curing procedure, warping was suppressed and dimensional reproducibility of approximately 50 µm was achieved. These improvements permitted a further simplification to a two-part design (V3.2), in which the top part and the middle sleeve are integrated into a single printed component. A schematic of this geometry is shown in Figure 5.13. This improved V3.1 by eliminating one mechanical interface within the SQUID detection region and reducing the number of parts to two. Sealing and compression are provided by a single threaded cap, improving both positional reproducibility and scan-to-scan background stability. The displacement of threaded interfaces outside the active scan range, improves radial symmetry, and reduced part count collectively result in more reliable background subtraction and lower residual uncertainty in the extracted sample moment. A further refinement introduces radial guide structures at the top and bottom of the holder, which are placed outside the detection region. The aim of this is to improve centring within the MPMS3 bore, thereby reducing positional uncertainties and improving the accuracy of the fitted moments. The refinement to V3.2 was implemented at a late stage of the project, such that the majority of measurements presented in this thesis were therefore performed using V3.1.

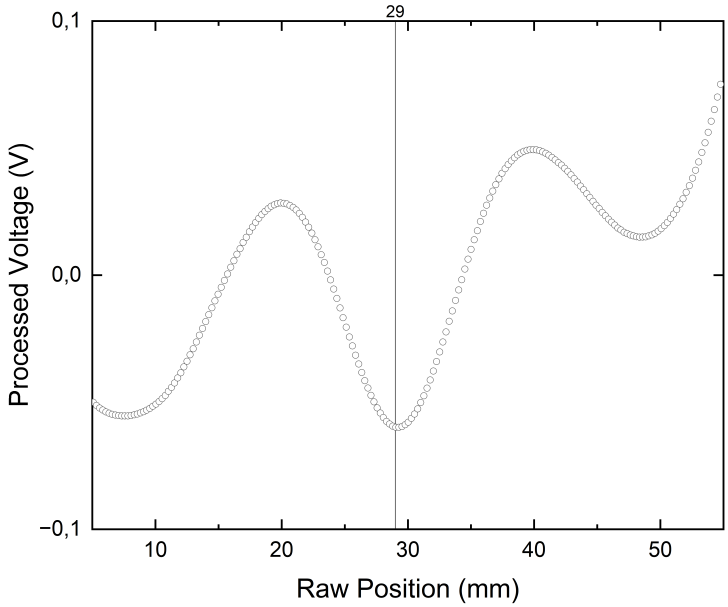


Figure 5.12: DC scans of the 3D-printed sample holder V3.1 at 300 K and 1 T. The marked position indicates the position of the sample volume (29 mm).

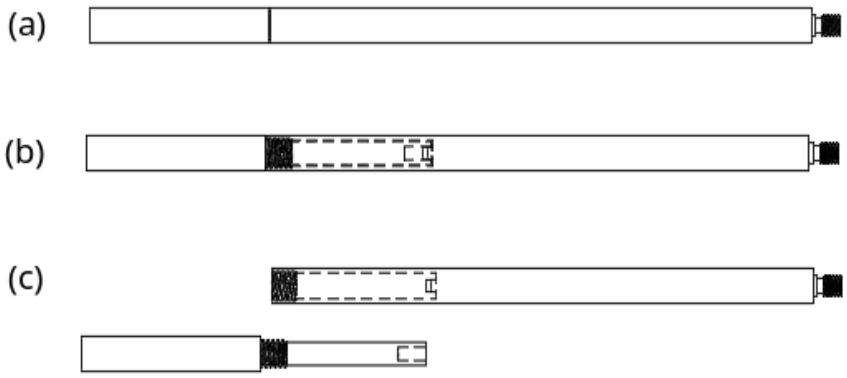


Figure 5.13: Schematic representation of sample holder V3.2, illustrating both the assembled (a),(b) and disassembled (c) states of the design.

5.1.4 Comparative Analysis

The previous sections analysed each design iteration individually. The following comparison considers all the designs that were measured collectively, grouping the holder versions according to their underlying geometry. V0.2, V1.1, and V2.1 share the original geometry, with the threaded region positioned within the measurement zone, whereas V1.2 and V3.1 share a revised geometry that relocates the threads outside this zone. Because this relocation also shifts the sample volume centre, direct comparison across the two geometries is less straightforward.

Figure 5.14(a) shows the background profiles of V0.2, V1.1, and V2.1 at 1 T and 300 K. The pronounced signal anomaly at 58.75 mm is present in all three designs, corresponding to the threaded connection region. The solid-rod geometry (V0.2) exhibits the smallest overall background, remaining nearly featureless from 15 mm to 40 mm consistent with its geometrically uniform cross-section of the central part of the sample holder. In contrast, V1.1 and V2.1 show additional signal variation in the vicinity of the sample chamber. This shows that the introduction of an empty sample chamber in V1.1 and V2.1 breaks this uniformity of V0.2, producing a localised effective magnetic signal from the missing diamagnetic volume. In V2.1, the multi-part cylindrical assembly introduces additional mechanical interfaces and tolerances that reduce positional reproducibility between loading cycles. Figure 5.14(b) compares the background profiles of V2.2, which is the improved version of V2.1 that is using a cylindrical sample volume, and V3.1 at 1 T and 300 K. Since V3.1 adopts the same cylindrical sample volume size and geometry, the two designs are directly comparable. Both profiles exhibit a localised minimum at 28.75 mm, corresponding to the sample chamber position. Outside this region, the signal exhibits contributions from the remaining holder geometry, with V3.1 consistently showing a lower overall background, demonstrating the benefit of the compression-based three-part construction.

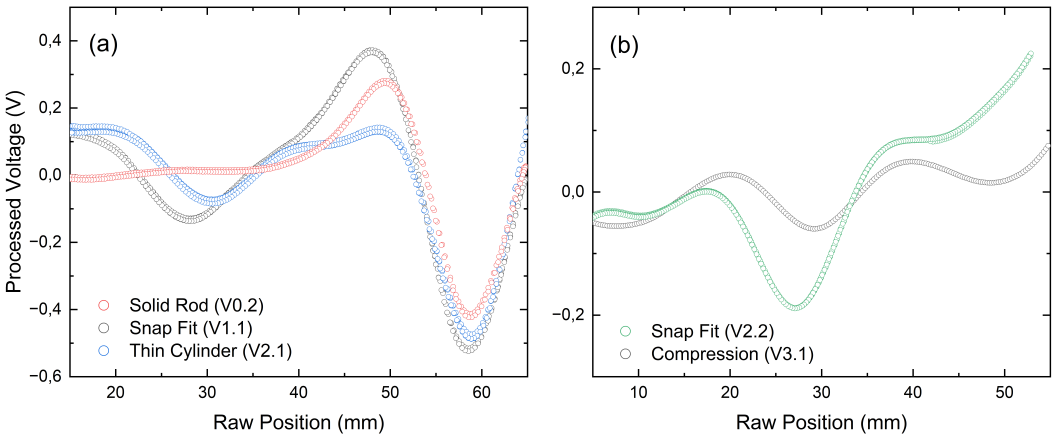


Figure 5.14: Raw SQUID DC scans of 3D-printed sample holders measured at 300 K and 1 T, comparing successive design iterations. (a) shows the measurement of Versions 0.2, 1.1 and 2.1, while (b) shows the measurements of Version 2.2 and 3.1.

The performed background measurements confirm that the dominant SQUID response of the 3D-printed sample holder originates from local geometric variations of the resin volume passing through the gradiometer coils, rather than from the absolute magnetic moment of the printed sample holder. Three critical design criteria emerged from the iterative development of the sample holder. These are minimising the part count within the detection region, strictly enforcing rotational symmetry and ensuring reliable positional reproducibility across repeated loading cycles. The final compression-based two-part design successfully implements all these criteria. This results in a good compromise between reduced magnetic background, mechanical stability, airtightness, and practical sample handling.

This highlights a key strength of the design approach adopted in this thesis. Rather than relying on a material with low susceptibility, as in the quartz-based approach, background suppression is achieved through the geometry. The experimental measurements confirmed that the dominant SQUID response of the SLA-printed sample holders originates not from the overall volume of the resin, which remains magnetic to a degree comparable to the samples under investigation, but from local variations in that volume within the gradiometer detection coils. Consequently, the achievable background suppression is less independent of the holder material's absolute susceptibility.

5.2 Numerical Simulation

This section provides a theoretical reference for the analysis of the sample holder. Simulations of the MPMS3 gradiometer response to magnetic point sources are used to illustrate how individual contributions combine to produce the overall background signal of the printed sample holder. The simulations proceed from simple abstractions to the detailed holder geometry in steps of increasing complexity. The aim of these simulations is to better understand the magnetic background produced by the holder and to establish a theoretical platform for iterative design optimisation, without the need to repeatedly print, post-process, and experimentally measure every design iteration. All simulations were implemented using Python (V3.14) together with the libraries NumPy (V2.4.2), SciPy (V1.17.1), Pandas (V3.0.1), and Matplotlib (V3.10.8). The calculations are based on the second-order gradiometer geometry of the MPMS3 and its associated response function. The radial extent of the sample holder is neglected throughout, and all simulations therefore consider only point sources located on the central axis.

As a first verification step, the response of a single point-like paramagnetic moment was simulated. The gradiometer response function is implemented following Equation (3.7), using a coil radius of 0.97 cm and coil spacing of 1.519 cm [58]. A single dipole of unit strength is placed at the centre of the coil, and the gradiometer response is evaluated along the scan axis from -5 cm to 5 cm. The resulting signal is normalised to its maximum absolute value. This was done, as the focus of the further comparisons lies on the shape of the dipole responses, rather than their absolute magnitude. The result is shown in Figure 5.15. It reproduces the characteristic MPMS3 response shape, consisting of a central peak with opposing shoulders. This simulation is mainly meant as a consistency check, confirming that the implementation correctly reproduces the expected signal form before it is applied

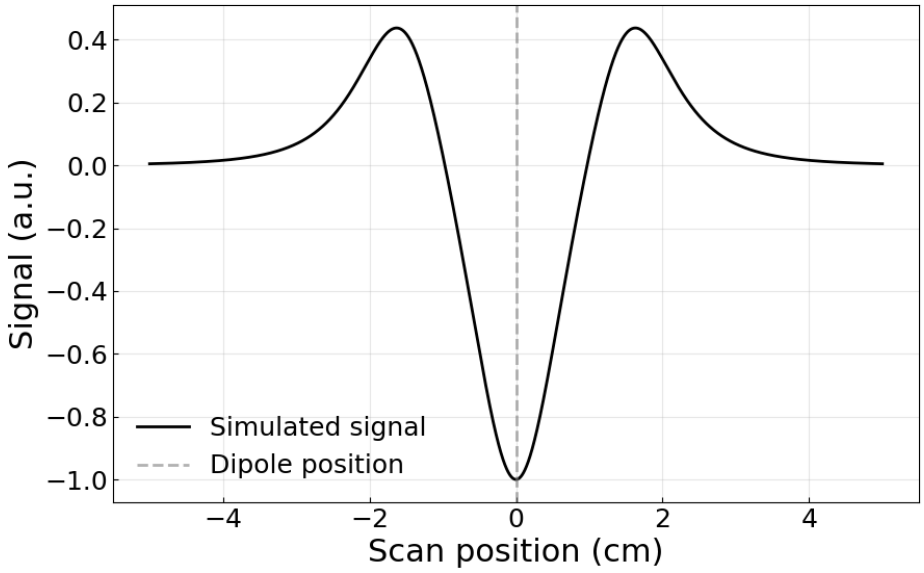


Figure 5.15: Simulated MPMS3 second-order gradiometer response to a single point-like magnetic dipole located at the coil centre (dashed vertical line at 0 mm). The signal is normalised to its maximum absolute value.

to more complex simulations. Interestingly, this simulation also shows that even localised magnetic moments can produce extended features in the measurements. This is particularly relevant for the development of the sample holder geometry, where local variations in material volume, such as threads or the empty sample volume, contribute significantly to the observed magnetic background signal.

After this initial test, additional magnetic moments were introduced to illustrate the contributions of different regions of the sample holder to the measured background signal. Figure 5.16 shows a simulation that simplifies the sample holder's signal to three dipoles, one located at the sample volume and the other two spaced symmetrically around it, representing the threads of the three-part sample holder design. The threaded areas and connection interfaces feature more complex geometries which, in combination with the manufacturing tolerances, result in a non-negligible signal. The three dipoles have relative strengths of 1.65 for the left thread, 2.22 for the sample volume, and 1.37 for the right thread, obtained by fitting the three-dipole model to the measured signal. The sample volume therefore exhibits the strongest response, while the two threads differ noticeably from one another. Although the two threaded regions are nominally identical, this difference reflects the manufacturing tolerances of the SLA process, which introduce slight geometric variations between them. Both, the sample region and the threaded connections, thus dominate the magnetic background of the holder.

In a further step, the model was extended to include an additional linear term, which is common for the MPMS3 and is usually subtracted in the automated fitting routine [53]. Be-

yond this general role, the linear term is particularly useful here, as the asymmetry between the two threads produces a gradient in the background along the scan axis. With the right thread contributing less than the left, this imbalance can be partly compensated by a sloped baseline. The result is shown in Figure 5.17. The linear contribution clearly improves the agreement between fit and data compared with the previous simulation without it.

To illustrate how the individual contributions combine, the three-dipole simulation including the linear contribution is shown again in Figure 5.18, this time with the response of each dipole plotted separately alongside their sum. The main sample region produces the dominant central feature, while the two threaded connections mostly contribute to the shape outside this region. These contributions overlap and superimpose to produce the final signal. This decomposition demonstrates that the extended features in the measured background arise from the superposition of several localised contributions rather than from a single source. Although the three-dipole model is highly simplified, it already reproduces several important qualitative features of the experimentally observed signal, supporting the assumption that the magnetic background is dominated by regions with complex geometries.

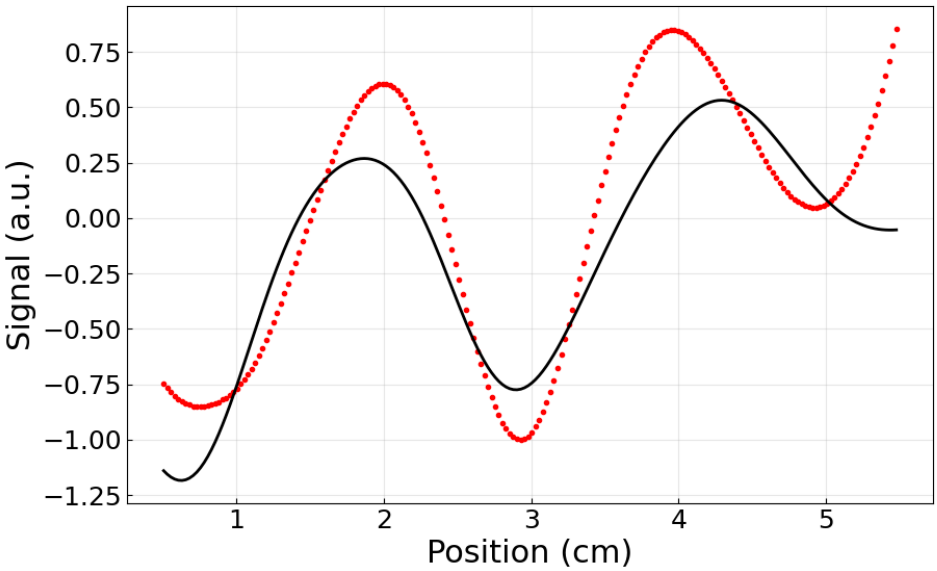


Figure 5.16: Simplified three-dipole simulation of the sample holder response (black) compared with a measurement (red). The three dipoles represent the main sample region and the two threaded connection areas.

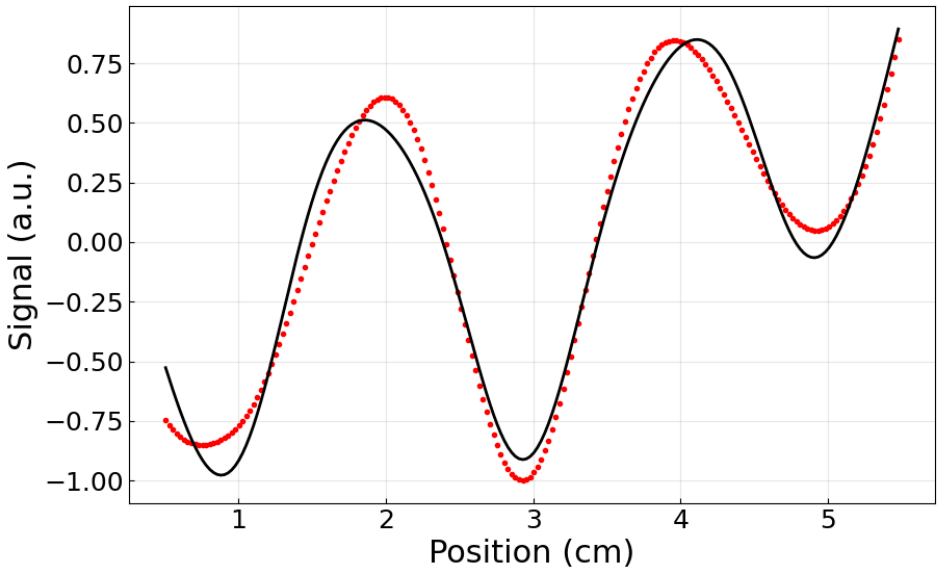


Figure 5.17: Three-dipole simulation including an additional linear background term (black) compared with the measurement (red). The linear contribution improves the agreement with the measured data relative to the model without it.

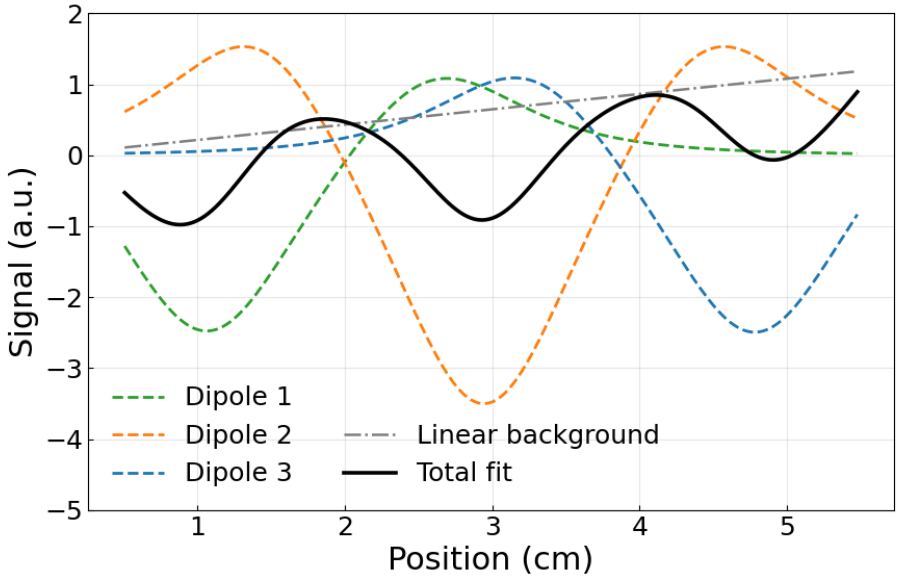


Figure 5.18: Three-dipole simulation including the linear term, showing the separated contribution of each dipole together with their sum. The individual responses superimpose to produce the total simulated signal.

In the final simulation stage, the theoretical magnetic response of the sample holder is modeled directly from the computer-aided design (CAD) geometry. The CAD model is converted into a one-dimensional volume profile along the SQUID measurement axis. The local resin volume along this axis (Figure 5.19) is then used as the estimate for the magnetic moment strength distribution. With this the sample holder is modeled as a series of point dipoles positioned along the central axis without explicitly considering radial extensions. Despite this simplification, the model captures the dominant contribution to the measured SQUID response as the MPMS3 is primarily sensitive to the axial magnetic moment distribution.

Figure 5.20 shows the simulated signal based on the CAD files alongside the measured signal after subtraction of the linear background, determined in the three-dipole simulation. The two profiles share only the approximate positions of the main contributions, as already indicated by the three-dipole simulation, but differ substantially in shape and relative amplitude. This demonstrates that geometric inhomogeneities, particularly at threaded interfaces, strongly influence the magnetic background signal of the holder. However, the simulation does not reproduce the measured profiles with sufficient accuracy for it to be of practical use. This is likely due to dimensional deviations between the CAD geometry and the printed part, combined with the simplifying assumptions employed. Therefore, it was not further developed. A more sophisticated simulation framework, accounting for print-induced geometric deviations (e.g. overcuring in the threaded regions) and a more accurate model of the radial distribution of the sample holder volume, could substantially facilitate future sample holder development by enabling predictive background optimisation prior to fabrication. However, such a full implementation lies beyond the scope of this work.

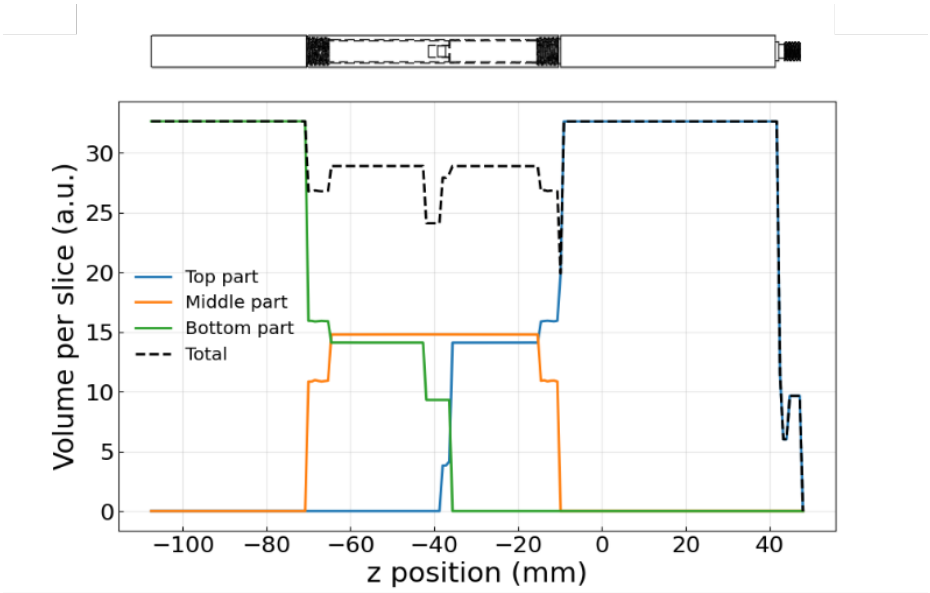


Figure 5.19: Volume profile along the SQUID measurement axis of the 3D-printed sample holder V3.1, with the design above for reference. Shown are the contributions of the top part (blue), bottom part (green), and central outer shell (orange), together with their sum (black).

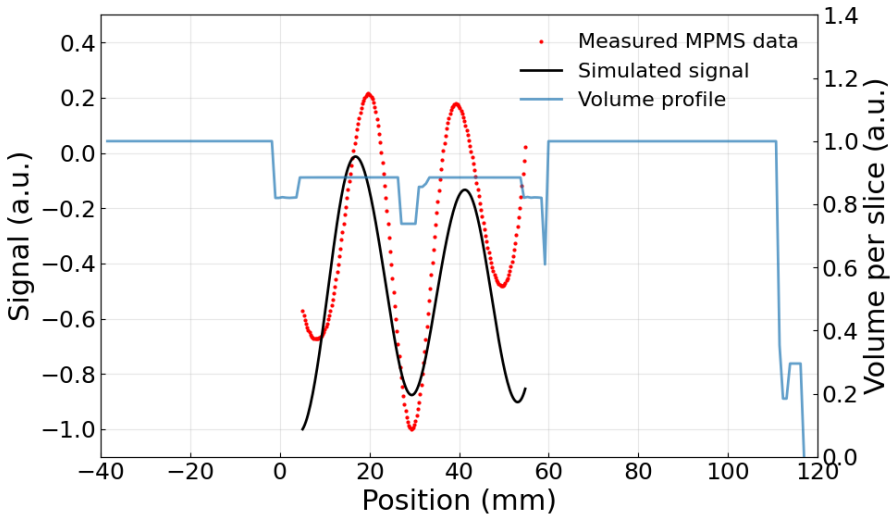


Figure 5.20: Final simulation (black) based on the volume profile along the SQUID measurement axis (blue) of the 3D-printed sample holder V3.1, in comparison to the measured data (red).

5.3 Experimental Validation

With the compression-based design established, the next step is to validate the holder's performance. These measurements were performed with version V3.1, the three-part compression design, since the final version V3.2 was developed in response to the results presented throughout this chapter and was not yet available. The evaluation of the 3D-printed sample holder was carried out to assess the reproducibility of the background signal and the accuracy of the extracted magnetic susceptibilities relative to established reference values. Reproducibility was evaluated by performing repeated measurements of the empty holder background under identical conditions, in order to quantify the consistency of the signal between nominally identical scans. To complement this assessment of reproducibility, the accuracy of the extracted susceptibilities was evaluated using a set of reference samples spanning a broad range of magnitudes, which served to characterise the operational range of the holder and to identify its practical limitations. If available, the results were compared with measurements obtained using the standard Quantum Design brass sample holder, providing a benchmark for performance assessment.

5.3.1 Reproducibility of the Background Signal

To assess the reproducibility of the empty holder background signal, two consecutive measurements were performed without removing the sample holder in between. Both used the identical empty sample holder and the same measurement sequence, which performs four scans per field value.

Isothermal magnetisation measurements were carried out at 300 K with applied magnetic fields in the range 0 T to 4 T, using DC voltage scans at the highest available detection sensitivity of the MPMS3 (range 1). Representative scans at 0.1 T, 1 T, 2 T, and 4 T were selected to assess the reproducibility across a broad range of magnetic fields. At each field value, four scans were performed per measurement to characterise the field dependence of the reproducibility systematically.

The analysis begins with the lowest field, where the largest deviations are expected due to the reduced absolute signal. The results of the measurement at 0.1 T are shown in Figures 5.21 and 5.22. Figure 5.21 shows the first measurement in (a) and the second in (b), to assess whether differences already appear between individual scans of a single measurement. The individual scans consistently show the same shape, although they vary slightly within both measurements. For a more direct comparison between the two measurements, Figure 5.22 compares the corresponding scans of the first and second measurements. These also show qualitatively similar curves with slight differences. Overall, at 0.1 T the absolute voltage signal is very small even at maximum sensitivity, making the measurement susceptible to noise and additional background contributions from the SQUID electronics, which appears as a linear background contribution to the sample holder signal. To better assess these deviations, the average and standard deviation of all scans from both measurements are shown in Figure 5.23(a).

With increasing field, the scan-to-scan overlap improves progressively. At 1 T (Figure 5.23(b)), 2 T (Figure 5.23(c)), and 4 T (Figure 5.23(d)), the individual scans are more consistent than at 0.1 T, becoming indistinguishable by eye when plotted together. Only the averages with their standard deviations are therefore shown. Even in this representation, the differences are difficult to assess visually. The average ratio of the standard deviation to the voltage signal was therefore calculated, with the values listed in Table 5.1.

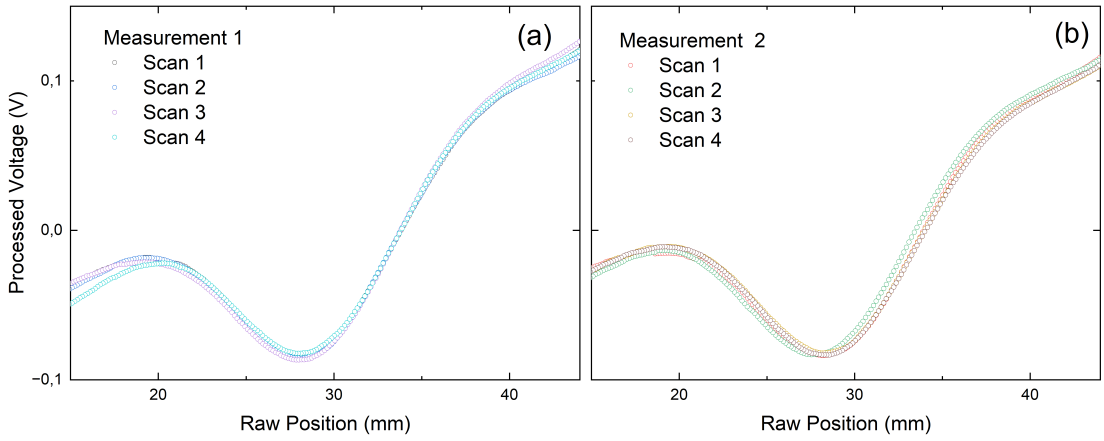


Figure 5.21: Individual scans of two consecutive background measurements of the empty 3D-printed sample holder V3.1 at 300 K and 0.1 T, arranged as panels for direct assessment of scan-to-scan variation.

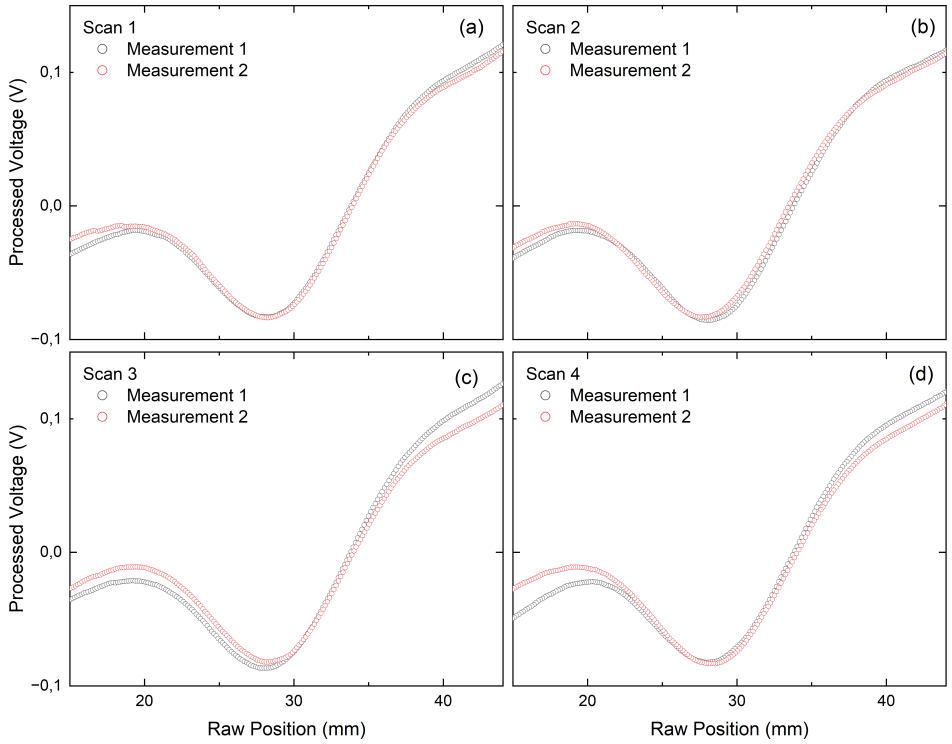


Figure 5.22: Overlay of two consecutive background measurements of the empty 3D-printed sample holder V3.1 at 300 K and 0.1 T, demonstrating the reproducibility of the measured voltage profile.

A clear trend is visible: the relative deviation is highest at 0.1 T and decreases with increasing field, remaining approximately equal for 1 T and 2 T. At 4 T, the scan profiles closely resemble the MPMS3 gradiometer fitting function, since the linear background from the instrument becomes relatively smaller compared with the signal as the field increases. This is not relevant for the subsequent fitting, as the linear term is included in the fit performed by the background subtraction software.

Table 5.1: Average ratio of the standard deviation to the absolute voltage signal across all scans, for each applied field.

Field (T)	0.1	1.0	2.0	4.0
$\lvert\sigma/V\rvert$	1.21×10^{-1}	3.08×10^{-3}	3.10×10^{-3}	7.51×10^{-4}

These measurements demonstrate that the background signal of the 3D-printed holder is highly reproducible, with the reproducibility improving significantly when increasing the applied field. The higher scan-to-scan variation observed at low fields is attributed to the low absolute signal level.

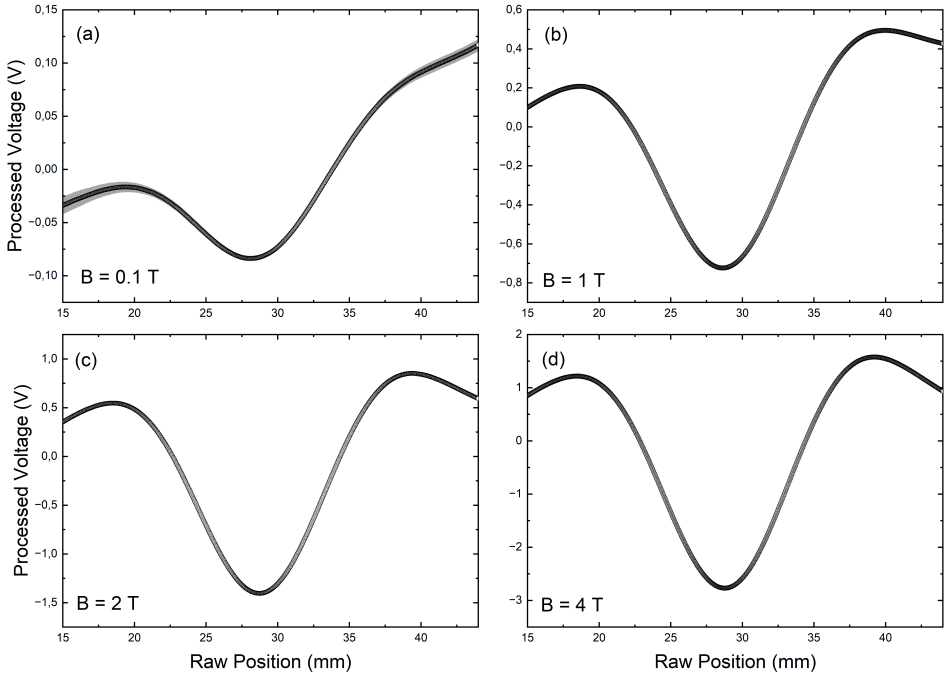


Figure 5.23: Average background signal of the empty 3D-printed holder with standard deviation, measured at 300 K for applied fields of (a) 0.1 T, (b) 1 T, (c) 2 T, and (d) 4 T. Each average is taken over all scans from two consecutive measurements. The scan-to-scan consistency improves with increasing field.

5.3.2 Comparison with Brass Holder and Plastic Capsule

As discussed before (see Chapter 5.1.1), the 3D-printed sample holder was developed as an alternative to the Quantum Design brass sample holder combined with plastic capsules for powdered samples. The two approaches are therefore compared in this section to assess whether the 3D-printed holder offers an improvement in magnetic background, positional reproducibility, and practical sample handling.

Figure 5.24 shows the background profiles of both empty sample holders, the Quantum Design capsule in the standard Quantum Design brass holder and the 3D-printed sample holder V3.1 developed in this work. The measurements were performed at 300 K and 1 T. The scan length for the 3D-printed holder was restricted to 30 mm as this already fully captures the sample region without contributions from the holder extremities. For the brass and capsule configuration the full 50 mm range was used. This is due to the fact that the brass holder with capsule yields a more complex background, whereas the 3D-printed sample holder produces a well-defined profile consistent with the response of a localised moment, reflecting its simplified symmetric geometry.

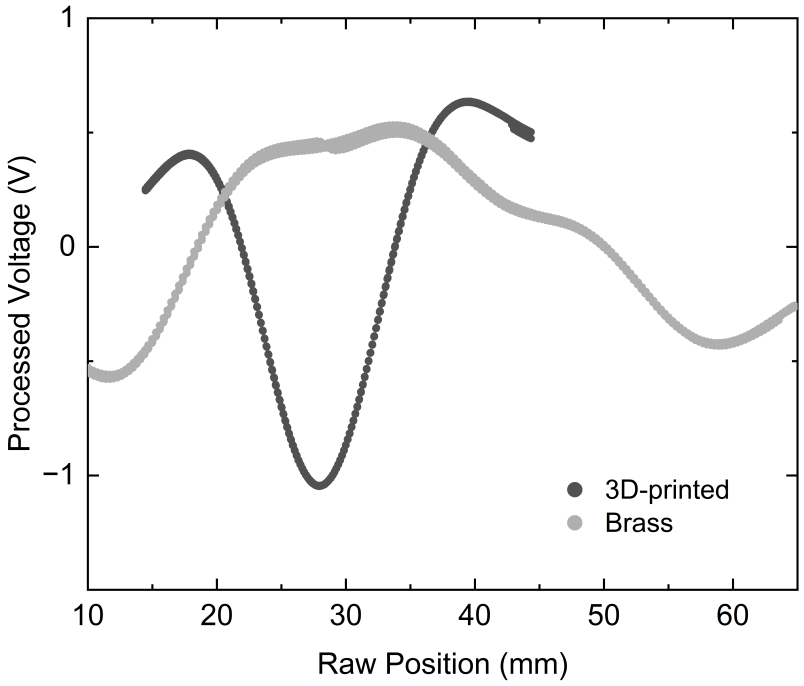


Figure 5.24: Comparison of the background profiles of both empty holders, the QD capsule in th standard Quantum Design brass holder and the 3D-printed sample holder V3.1 developed in this work, at 300 K and 1 T.

To demonstrate the difference in the usability of these two sample holder options, approximately 6 mg of naphthalene are measured in both configurations under identical conditions. The DC scans of the sample measurement, the background measurement and the background-subtracted results are shown in Figure 5.25. The background subtraction process relies on the point by point subtraction of the background data from the measurement of the sample and the sample holder. This process is sensible to deviations in the positioning of the sample mounting setup. If there are no deviations in this positioning, the resulting signal is therefore purely from the sample, and is subsequently fitted with the gradiometer response function (Equation (3.7)).

In the brass holder with plastic capsule (Figure 5.25(a)), the measured background signal is, as noted before, quite complex. This gets slightly altered by the sample, which can be seen by the "filled" data. It is observable that the strength of the sample signal is dominated by the capsule background, which is not generally a problem, if the alignment of the measurements is accurate. The background subtracted data don't show a signal that can be fitted by the background subtraction routine. Therefore, no reliable sample moment can be extracted. This leads to the conclusion, that there was a deviation in the positioning of the capsule between the background and sample measurements.

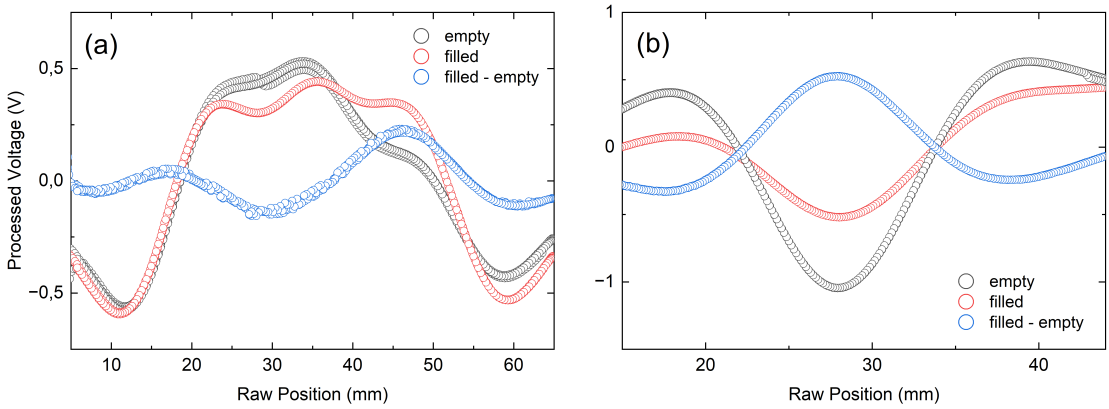


Figure 5.25: Subtraction of the sample holder background for the (a) commercial Quantum Design capsule in the brass holder and (b) the 3D-printed sample holder V3.1. The corrected sample signal (blue) is obtained by subtracting the DC scan of the empty sample holder (black) from the scan of the sample within the sample holder (red). The scans were performed at 300 K and 1 T

In the data of the 3D-printed sample holder (Figure 5.25(b)), the background measurement shows signal that resembles the shape of the response of a paramagnetic sample. The amplitude of this decreases after introducing the sample, while the shape remains similar. The signal after background subtraction shows a signal that, again resembles the shape of the response to a localised magnetic moment, but with reversed sign. Meaning that the sample is diamagnetic, which is true for naphthalene. Consequently the signal can be fitted and the diamagnetic susceptibility can be directly determined.

This comparison demonstrates the primary situation for which the custom holder was designed, namely the measurement of weakly magnetic powders. Based on this successful background subtraction with the 3D-printed sample holder, the quantitative accuracy is assessed in the following.

5.3.3 Accuracy Assessment Using Reference Samples

The accuracy of the susceptibility extracted using the 3D-printed holder is assessed using several reference samples. In decreasing order of susceptibility magnitude, these are the Quantum Design gadolinium gallium garnet (GGG) AC calibration sample (paramagnetic), the Quantum Design palladium standard (paramagnetic), naphthalene (diamagnetic), and anthracene (diamagnetic). For each sample, the measured susceptibility is compared with a reference value. This can be a calculated theoretical value, a literature value, or if both are not available or very broad, the measurement using the standard brass holder serves as a reference.

GGG Reference Sample

GGG is supplied by Quantum Design as a calibration reference for AC susceptibility measurements in the MPMS3, with mass $m = 157.48(1)\,\mathrm{mg}$ and composition $Gd_3Ga_5O_{12}$, making it an excellent paramagnetic reference material [59, 60]. Owing to its large magnetic susceptibility in the order of $10 \times 10^{-5}\,\mathrm{erg\,G^{-2}\,mol^{-1}}$, the magnetic moment of the sample exceeds the background signal of the sample holder by several orders of magnitude. Consequently, the measurement primarily probes whether the holder introduces systematic distortions into the extracted susceptibility, while being comparatively insensitive to the effectiveness of background subtraction. The molar mass and literature values for the Curie constant and Weiss temperature predict a molar susceptibility in the range $1.10 \times 10^{-5}\,\mathrm{erg\,G^{-2}\,mol^{-1}}$ to $1.42 \times 10^{-5}\,\mathrm{erg\,G^{-2}\,mol^{-1}}$. Since this range is comparatively broad, the standard Quantum Design brass holder is used as the primary reference for evaluating the accuracy of the 3D-printed sample holder, providing a relative assessment of its measurement quality.

The isothermal magnetisation of the GGG reference sample and the background of the sample holder were measured at 300 K in magnetic fields from 0 T to 7 T using the 3D-printed sample holder V3.1. The resulting magnetisation with and without background subtarction are shown in Figure 5.26(a). Linear fits to the complete field range yield the susceptibilities χ summarised in Table 5.2. The GGG sample was also measured, including background measurements, using the standard Quantum Design brass holder by Matthias Heinrich (Kirchhoff Institute for Physics, Heidelberg University), providing a direct reference measurement 5.26(b) with the obtained χ, also summarised in Table 5.2.

All measured susceptibilities lie within the quite broad literature range. The susceptibilities obtained using the brass holder and the 3D-printed holder agree to within 0.33 %. Furthermore, the relative difference from the background-corrected to the uncorrected measurements performed using the 3D-printed holder is 0.17 %. This shows that the sample holder background is small compared to the magnetic response of the GGG reference sample. Strangely, the background subtraction leads to a larger deviation from the brass measurement. This could be explained either by the brass holder result itself deviating from the true value, or by the background subtraction overcompensating the background of the 3D-printed sample holder.

Table 5.2: Molar magnetic susceptibility of the GGG reference sample determined from linear fits to the isothermal magnetisation data for different holder configurations, compared with the literature range.

Configuration	χ ($\mathrm{erg\,G^{-2}\,mol^{-1}}$)	Deviation from brass (%)
Brass holder	1.186×10^{-5}	0.00
3D-printed, uncorrected	1.184×10^{-5}	−0.15
3D-printed, corrected	1.182×10^{-5}	−0.33
Literature range	1.10×10^{-5} to 1.42×10^{-5}	

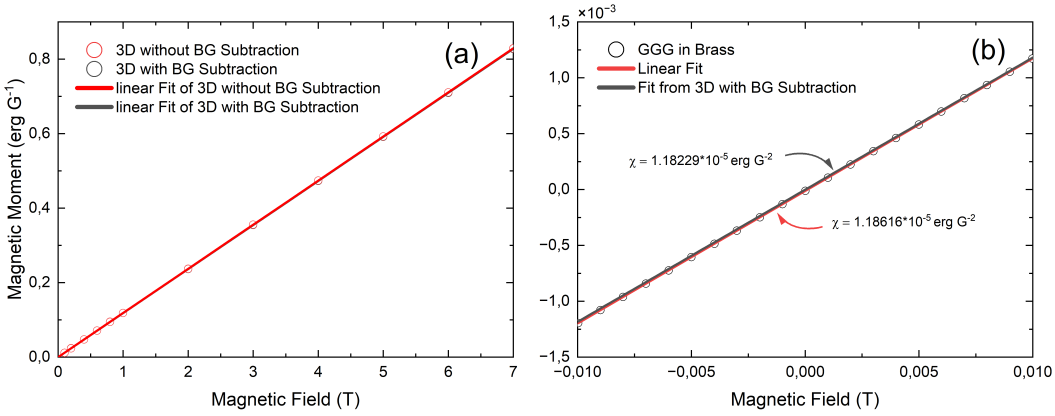


Figure 5.26: Isothermal magnetisation of the GGG AC calibration reference measured using the 3D-printed sample holder (a) with and without background correction, and the standard brass holder (b).

Quantum Design states that the GGG standard is only intended to verify calibration consistency rather than for it to serve as an absolute calibration standard [59]. Overall, the GGG reference measurement demonstrates that the 3D-printed sample holder reproduces the susceptibility obtained with the standard brass holder to within 0.33 %. This leads to the conclusion, that the holder geometry and axial sample positioning are sufficient for accurate susceptibility determination in strongly paramagnetic samples. For such samples, the holder background contribution is negligible and does not limit measurement accuracy.

Palladium Reference Sample

The palladium reference sample (Quantum Design, P587, with $m = 262.40(1)\,\mathrm{mg}$) provides a precise theoretical susceptibility against which the measurement accuracy can be assessed. Using the mass susceptibility, provided by Quantum Design, $\chi_{\mathrm{mass}} = 5.25 \times 10^{-6}\,\mathrm{erg\,G^{-2}\,g^{-1}}$, the expected susceptibility of the reference sample is $\chi_{\mathrm{theo}} = 1.377\,60 \times 10^{-6}\,\mathrm{erg\,G^{-2}}$. The sample was first measured in the standard brass sample holder, with and without background subtraction, to validate the subtraction procedure independently of the custom sample holder. Next, the same measurements were performed using the identical settings using the 3D-printed sample holder V3.1. The evaluation and background subtraction follows the same routine as described in Section 5.3.2. The results are shown in Table 5.3.

The measurements of the Pd reference sample using the brass sample holder without background correction show a deviation in the obtained susceptibility from the theoretical value by only 0.30 %. This indicates that the magnetic contribution of the brass holder is negligible in comparison to the signal strength of the Pd sample. The background subtraction further reduces this deviation to 0.17 %, demonstrating that the subtraction procedure is working correctly. The remaining offset could be attributed to the used glue (GE 7031 varnish) for securing the Pd sample into place.

Table 5.3: Magnetic susceptibility of the palladium reference sample measured in the standard brass sample holder and the 3D-printed sample holder (V3.1), with and without background correction, compared with the theoretical value.

Configuration	χ (erg G^{-2})	Deviation from χ_{theo} (%)
Theoretical value	1.378×10^{-6}	0.00
Brass holder, uncorrected	1.373×10^{-6}	−0.30
Brass holder, corrected	1.375×10^{-6}	−0.17
3D-printed, uncorrected	1.361×10^{-6}	−1.23
3D-printed, corrected	1.337×10^{-6}	−2.93

For the measurements using the 3D-printed holder, the uncorrected measurement deviates from the theoretical value by only approximately 1 %, while background correction increases the deviation to approximately 3 %. The isothermal magnetisation for both holder configurations are shown in Figure 5.27. The increase in the deviation from the reference value through background subtraction of the 3D-printed holder indicates, that the sample holder background measurement is systematically overcorrecting the sample holder's contribution.

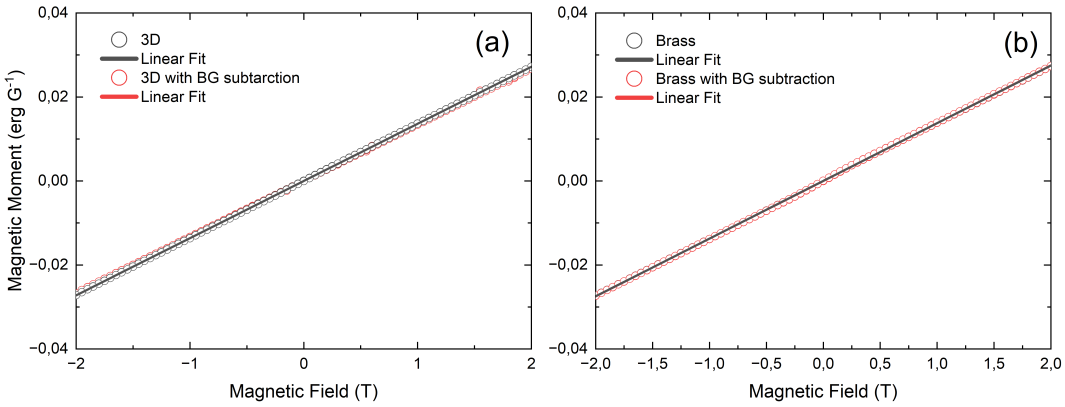
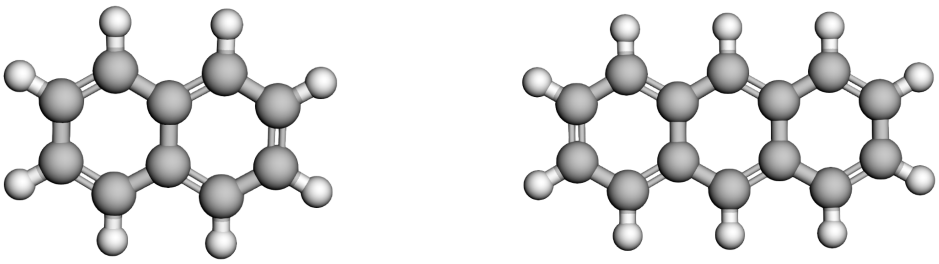


Figure 5.27: Isothermal magnetisation at 300 K from −2 T to 2 T of the palladium reference sample measured in the brass holder (a) and the 3D-printed holder (b), with and without background subtraction.

Naphthalene and Anthracene

Naphthalene ($C_{10}H_8$, Figure 5.28a) and anthracene ($C_{14}H_{10}$, Figure 5.28b) were selected as weakly diamagnetic reference systems for further evaluation of the sample holder performance. Both are planar, conjugated π-electron systems in which electron delocalisation gives rise to aromatic ring currents, producing a diamagnetic response that is small in magnitude but well characterised in the literature [61].



(a) Naphthalene $C_{10}H_8$ (b) Anthracene $C_{14}H_{10}$

Figure 5.28: Aromatic test samples used for validation of the 3D-printed sample holder. Both are polycyclic aromatic hydrocarbons composed of fused benzene rings, serving as representative weakly diamagnetic π-conjugated systems.

Naphthalene has a moderate vapour pressure at room temperature and would therefore require an airtight sample volume to prevent the loss of the sample due to sublimation. To additionally suppress the sublimation of the sample, the measurements were performed at 100 K with the compression holder V3.1. Anthracene possesses a substantially higher vapour pressure and was measured at 300 K. Sample preparation was performed without metal tools to prevent ferromagnetic contamination. The sample cavity was filled completely to prevent sample movement during the scan resulting in masses of 15.95(18) mg and 12.17(37) mg for naphthalene and anthracene, respectively.

The measured molar magnetisation as a function of the applied magnetic field is shown in Figure 5.29. Both samples exhibit clear diamagnetic behaviour, with magnetisation varying linearly with applied field and no indication of saturation or ferromagnetic contributions. It can be observed that the data below 1 T is not linear in field as it contains many outliers, this is due to the increasing daviations, which were analysed for the background in Section 5.3.1. Therefore these were excluded for the further analysis. The molar susceptibilities extracted from linear fits to the data above 2 T are summarised in Table 5.4. The anthracene value is in close agreement with the literature value, while naphthalene shows a higher deviation. The larger deviation observed for naphthalene is attributed to the autorange setting of the SQUID, which selected an insufficiently sensitive measurement range for reasons that could not be identified. This was not observed during the anthracene measurement, and lead to the subsequent adoption of a fixed range setting for all further measurements.

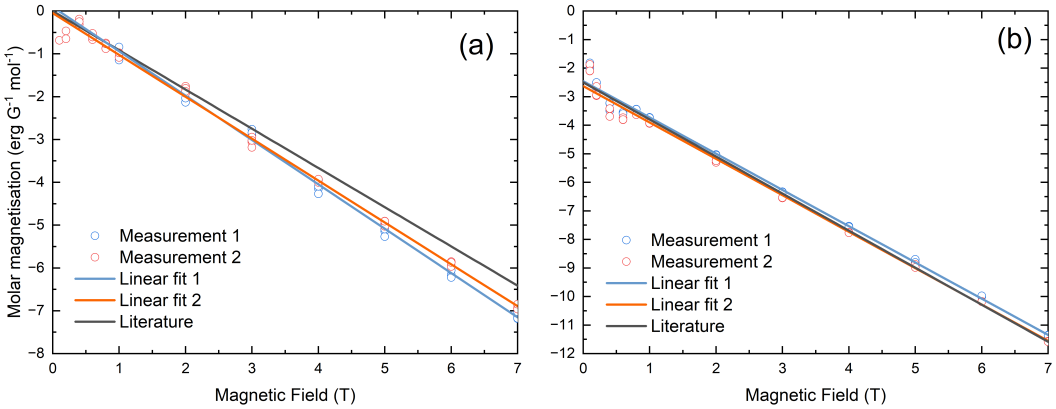


Figure 5.29: Isothermal molar magnetisation as a function of applied magnetic field measured from 0 T to 7 T for naphthalene (a) and anthracene (b) using the 3D-printed sample holder (Version 3.1). The experimental data are compared with literature values from [62].

As a comparison, the molar susceptibilities of naphthalene and anthracene were estimated using Pascal's constants. This yields values of -83.4×10^{-6} erg G^{-2} mol^{-1} for naphthalene and 113.3×10^{-6} erg G^{-2} mol^{-1} for anthracene. These values underestimate the magnitude of the literature values, by 10.3 % for naphthalene and 12.9 % for anthracene. This shows the limitations of the Pascal's constants in capturing the enhanced diamagnetism arising from aromatic ring currents.

Table 5.4: Molar magnetic susceptibilities of naphthalene and anthracene determined from linear fits to the field-dependent molar magnetisation measured using the 3D-printed sample holder (Version 3.1), in comparison to literature values from [61].

Sample	$\chi_{\mathrm{mol,lit}}$ (erg G^{-2} mol^{-1})	χ_{mol} (erg G^{-2} mol^{-1})	Dev. (%)
Naphthalene	-93×10^{-6}	-103.5×10^{-6}	+11.29
		-97.78×10^{-6}	+5.14
Anthracene	-130.1×10^{-6}	-127.5×10^{-6}	−2.00
		-126.9×10^{-6}	−2.46

5.3.4 Comparative Analysis

The reference measurements presented in the previous sections are now considered together to identify general trends or systematic deviations. Table 5.5 summarises the susceptibilities of the samples and the deviation of the values measured with the 3D-printed holder, both before and after background correction. A consistent pattern emerges across the measurements of the two reference samples. The background correction results in a systematic

over-correction that exceeds the original background contribution. This can be explained by the fact, that the system was calibrated using the Pd reference inside a brass holder, which should be improved by using background subtracted data using the 3D-printed sample holder to determine the appropriate calibration factor. This could be simply done inside the background subtraction software. For the weakly magnetic organic compounds, there is no comparison to an uncorrected value, as this is simply not possible. In contrast to the brass sample holder where not even background subtraction works, the 3D-printed sample holder enables the determination of the susceptibility using background subtraction. The value obtained for naphthalene is not representative, as it was found to be systematically affected by the SQUID range setting.

Table 5.5: Summary of obtained susceptibilities for all reference samples in the 3D-printed holder, before and after background correction, ordered by decreasing susceptibility magnitude.

Sample	χ (erg G^{-2})		Uncorr. dev. (%)	Corr. dev. (%)
GGG reference	1.186	$\times 10^{-5}$	−0.15	−0.33
Pd reference	1.378	$\times 10^{-6}$	−1.23	−2.93
Naphthalene	−1.157	$\times 10^{-8}$	not possible	8.22
Anthracene	−8.885	$\times 10^{-9}$	not possible	−2.23

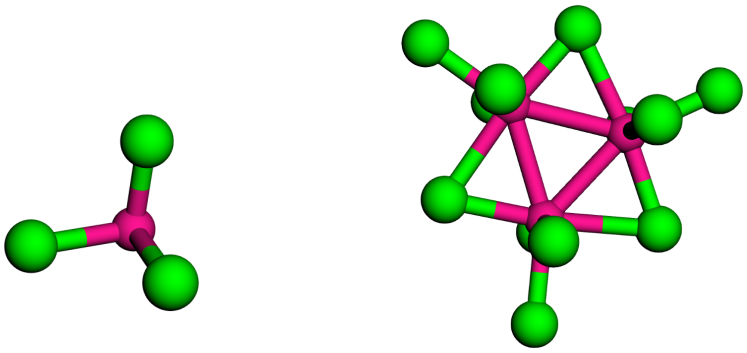
Importantly, the primary motivation for the 3D-printed holder is nonetheless validated by the comparison. The custom holder allows the diamagnetic signal of weakly magnetic samples, e.g. naphthalene and anthracene, to be measured, and is even expected to produce even better results, once the clibration factor is properly set. Alternatively, future improvements to the background subtraction procedure may also reduce the over-correction and extend the practical accuracy of the holder.

5.4 Diamagnetic Response of Rhenium(III) Chloride Complexes

The rhenium systems investigated in this work, $ReCl_3$ and Re_3Cl_9, serve as model compounds to probe metal-centred aromaticity via magnetic susceptibility measurements [3]. As introduced in Section 2.5, metal-centred aromaticity results in an enhanced diamagnetic response arising from field-induced cyclic delocalisation of electrons over a closed metal framework, in direct analogy to the ring-current effect in organic aromatic systems. The closed triangular Re_3 core of Re_3Cl_9 provides the cyclic symmetry required for this, while the mononuclear $ReCl_3$ serves as a reference compound in which no such delocalisation occurs.

The following section has the aim to show that Re_3Cl_9 exhibits an enhanced diamagnetic susceptibility to $ReCl_3$, due to a delocalisation-induced contribution beyond the local orbital diamagnetic and Van Vleck paramagnetic contributions present in both compounds.

Any susceptibility difference observed between the two systems can therefore be taken as indicative of cyclic delocalisation over the Re_3 core. For such a measurement to be reliable, potential contributions from oxygen contamination, ferromagnetic impurities, and sample holder background are adequately controlled. A quantitative decomposition of this difference is, however, complicated due to the strong spin–orbit coupling in 5d systems, as discussed below.



(a) (b)

Figure 5.30: Rhenium(III) chloride complexes investigated as reference systems for probing metal-centred aromaticity: the mononuclear $ReCl_3$ (a) and the trinuclear Re_3Cl_9 (b). Colour scheme: Re (purple), Cl (green).

Both compounds, $ReCl_3$ and Re_3Cl_9, contain formally Re(III) centres with a $5d^4$ electron configuration, making them electronically comparable at the local level. In the solid state $ReCl_3$ sample, the Re centres are spatially separated and interact only weakly, such that the magnetic response is expected to reflect the properties of isolated Re(III) sites. In Re_3Cl_9, by contrast, strong overlap between the Re 5d orbitals gives rise to metal–metal bonds and molecular orbitals extending over the entire Re_3 core [63, 64]. Cyclic delocalisation over the closed triangular Re_3 framework is a prerequisite for a ring-current-like magnetic contribution, which is expected to manifest as an enhanced diamagnetic susceptibility in Re_3Cl_9 relative to the mononuclear reference. Spin–orbit coupling in 5d systems is large enough to mix spin and orbital angular momentum, rendering the spin-only approximation inadequate. This introduces ambiguity into the quantitative interpretation of any precise susceptibility difference, such that the aim is to get data for a qualitative comparison.

5.4.1 Sample Preparation and Measurement Protocol

The Re(III) complexes were synthesised by Jie Zhang in the Greb group at Heidelberg University and used without further modification. The samples are stable at air and under light, and were stored under ambient conditions. All sample handling was performed with non-metallic tools to prevent ferromagnetic contamination of the samples. The used sample masses are listed in Table 5.6.

Measurements were performed using a slightly adapted version of the custom 3D-printed sample holder V3.1 with background subtraction applied as described in Section 3.1.3. The

cylindrical sample volume was reduced to a height of 2 mm with a diameter of 3.8 mm, as the available quantity was insufficient to fill the standard Pd reference sample sized cavity. Isothermal magnetisation curves were recorded from 0 T to 7 T at various temperatures between 1.8 K and 300 K. Magnetisation measurements at constant magnetic fields were performed from 1.8 K to 300 K at various in the range from 1 T to 5 T. All measurements were carried out in DC scan mode with 30 mm scan length, fixed range setting of the SQUID of 1 ($|B| \leq 4\,\mathrm{T}$) or 10 ($|B| > 4\,\mathrm{T}$), and two scans per data point under stable field and temperature conditions.

Table 5.6: Masses and molar masses of the Re(III) samples used for SQUID magnetometry measurements.

Sample	Molar mass ($\mathrm{g\,mol^{-1}}$)	Sample mass (mg)
$ReCl_3$	292.557	27.79(1)
Re_3Cl_9	877.671	25.62(4)

5.4.2 Isothermal Magnetisation of the Monomer $ReCl_3$

The isothermal magnetisation of the rhenium monomer was recorded between 0 T and 7 T. The background subtraction was successful at 10 K, 25 K and 75 K, while measurements at additional temperatures (1.8 K, 4 K, 50 K, 100 K, 150 K, 200 K and 300 K) were not usable due to not yet fully understood errors of the device. The reliable datasets exhibit jumps in the measured moment at 2 T and 4 T for 10 K and 75 K respectively. Such jumps can be attributed to the switching of the used range setting and electronic background in the readout electronics [54]. This explanation fits perfectly for the 75 K dataset where the range was switched at 4 T. Contrary, the jump in the 10 K data is not directly attributable to a common effect. If this is purely a constant offset, it can easily be corrected by shifting the results by a fixed value. Such a constant shift does not affect the following analysis, as the susceptibility will be extracted from the slope which is not affected by this. The correction is shown in Figure 5.31.

The corrected data, and the remaining dataset that did not need correction at 25 K, are shown in Figure 5.32 alongside their linear fits. These measurements indicate a diamagnetic response with a weak temperature dependence. The susceptibilities at all three temperatures were extracted from the linear fits to the data above 2 T. The obtained susceptibilities are listed in Table 5.7.

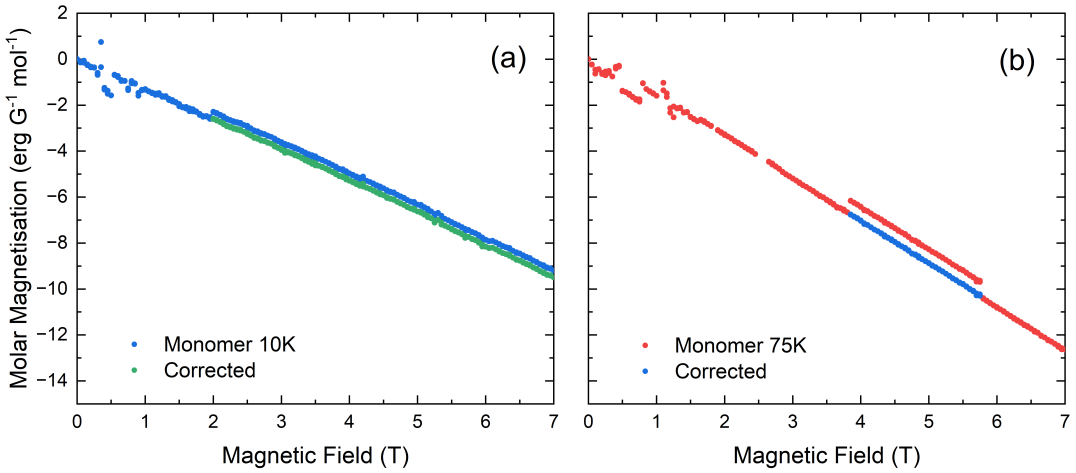


Figure 5.31: Corrections applied to the isothermal magnetisation $M(B)$ of $ReCl_3$ measured between 0 T and 7 T at 10 K (a) and 75 K (b).

Table 5.7: Temperature-dependent molar magnetic susceptibility of $ReCl_3$ determined from linear fits to the $M(B)$ data. In the third column, the deviations from the Pascal diamagnetic estimate $\chi_{\text{Pascal}} = -99\times10^{-6}\,\text{erg}\,\text{G}^{-2}\,\text{mol}^{-1}$ is given by $\chi/\chi_{\text{Pascal}}$.

Temperature (K)	χ_{mol} (erg G^{-2} mol^{-1})	$\chi/\chi_{\text{Pascal}}$
10	-1.3653×10^{-4}	1.38
25	-1.7262×10^{-4}	1.74
75	-1.8694×10^{-4}	1.89

All three isothermal magnetisation curves show a negative and linear behaviour, consistent with a diamagnetic response. The magnitude of the diamagnetic susceptibility decreases with decreasing temperature, which at first sight, could suggest a temperature dependence of the diamagnetic contribution. However, such behaviour is physically unreasonable, as orbital diamagnetism is, to a substantial degree, independent of temperature. A more plausable explanation is the presence of a paramagnetic contribution from an impurity that is superimposed on the diamagnetic background. Such a contribution follows a Curie-like $1/T$ dependence and therefore increases at lower temperatures, which reduces the diamagnetic signal and leads to an apparent reduction in the net susceptibility magnitude. A clearer separation of these contributions is obtained from the $M(T)$ data, which is discussed in the following.

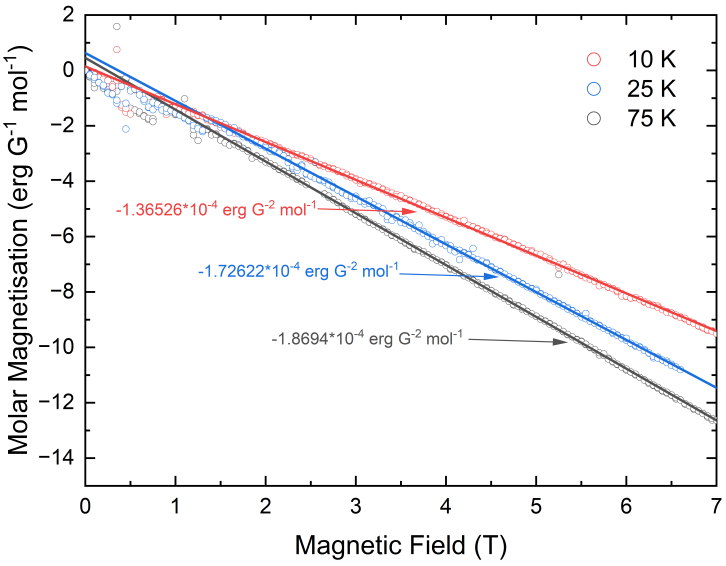


Figure 5.32: Isothermal magnetisation of $ReCl_3$ measured from 0 T to 7 T at 10 K, 25 K, and 75 K. The 10 K and 75 K datasets have been corrected for the artefacts from the readout electronics. Linear fits ($M = \chi B + \chi_0$) to the data for $2\,\mathrm{T} \leq B \leq 7\,\mathrm{T}$ are shown, with the obtained susceptibilities indicated by the adjacent labels.

5.4.3 Temperature Dependent Magnetisation of the Monomer $ReCl_3$

The corresponding temperature-dependent magnetisation data has been recorded from 1.8 K to 300 K, with only the range from 1.8 K to 175 K having reliable background subtraction, and is shown in the Figure 5.33(a). These data exhibit a more complex temperature dependence than expected from the M(B) data. At high temperatures, the susceptibility approaches a constant diamagnetic value of approximately $-1.75 \times 10^{-4}\,\mathrm{erg\,G^{-2}\,mol^{-1}}$, and towards low temperatures it increases rapidly, until it shows a dip with a local minimum. Additionally, a pronounced feature is observed around 50 K.

This increase towards low temperatures can be attributed to a paramagnetic impurity, showing Curie-like behaviour. While the approached diamagnetic contribution can be explained by the temperature-independent orbital diamagnetism, the susceptibility at high temperatures is lower than expected when compared to the values from the M(B) fits (Table 5.7). This shows an underestimation of the susceptibility in the M(T) data, as the 75 K M(B) data shows a stronger diamagnetic molar susceptibility than the data point for 75 K in the M(T) data. The trend observed from the three M(B) curves is supported by this data, supporting the assumption that the diamagnetic contribution is not temperature-dependent but superimposed by a temperature-dependent Curie-contribution. The feature near 50 K is attributed

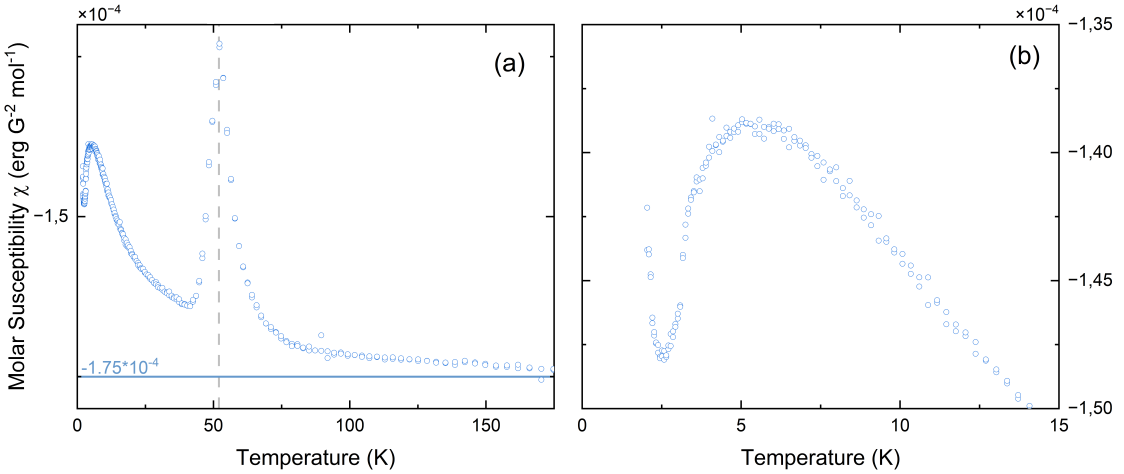


Figure 5.33: Temperature dependence of the magnetisation $M(T)$ of $ReCl_3$. (a) shows the isothermal magnetisation $M(T)$ measured between 1.8 K and 175 K with the horizontal line indicating the approached diamagnetic susceptibility at high temperatures and the vertical line marking the centre of the oxygen peak. (b) Shows a magnified view of the low-temperature region between 0 K and 15 K.

to oxygen-related contributions, which may arise from sample handling or residual adsorption effects. At low temperatures, shown in more detail in the right panel of Figure 5.33, the data suggest the presence of an additional magnetic contribution superimposed on the diamagnetic background. The shape of the low-temperature feature is qualitatively consistent with a spin-chain-like contribution, as commonly observed in rhenium-based systems, particularly mixed-valence or defect-related Re(IV) species. [13]. Given the small amplitude of this contribution, its concentration is estimated to remain below the percent level and could therefore be a residual species from synthesis or an impurity.

5.4.4 Isothermal Magnetisation of the Trimer Re_3Cl_9

The measurement of the trimer follows the same protocol as the monomer. However, it exhibits significantly fewer artefacts in the recorded data, leading to the successful background subtraction for 1.8 K, 4 K, 50 K, 100 K, 150 K, 200 K and 300 K. Figure 5.34 shows the M(B) data for all recorded temperatures with successful background subtraction. For temperatures above 100 K, the curves collapse onto a common linear diamagnetic behaviour. The 50 K data shows linear diamagnetic behaviour as well, but of a lower strength. Moving to even lower temperatures, the 4 K and 1.8 K data show paramagnetic behaviour. A linear fit to the high-temperature data above 150 K yields a molar susceptibility of $-2.056 \times 10^{-4}\,\mathrm{erg\,G^{-2}\,mol^{-1}}$, corresponding to 69 % of the Pascal diamagnetic estimate of $-2.97 \times 10^{-4}\,\mathrm{erg\,G^{-2}\,mol^{-1}}$. This can be attributed to the temperature-independent orbital diamagnetism. At 50 K, a deviation from this high temperature behaviour is observed, resulting in a reduced diamagnetic

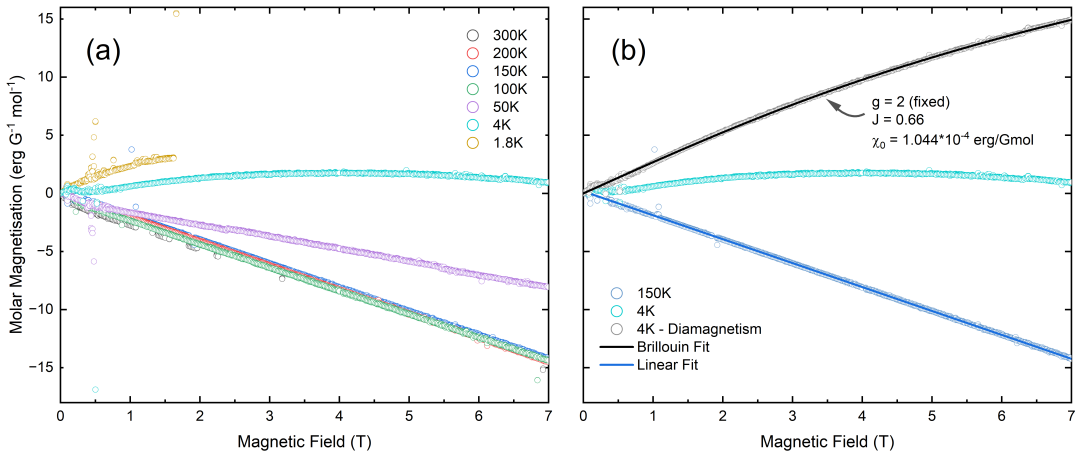


Figure 5.34: Isothermal magnetisation $M(B)$ of Re_3Cl_9 measured between 0 T and 7 T. (a) Displays all recorded temperatures between 1.8 K and 300 K, and (b) shows the magnetisation curves at 4 K and 150 K, the 4 K from which the temperature independent diamagnetic contribution was subtracted, and a Brillouin function fit to this corrected data.

susceptibility. At low temperatures (4 K and 1.8 K), a positive contribution to the susceptibility emerges, indicating the presence of a paramagnetic component. After subtraction of the high-temperature diamagnetic contribution from the 4 K data, shown in Figure 5.34, this contribution can be described by a Brillouin function (Figure (2.14)) with $g = 2$, $J = 0.66$ and $\chi_0 = 1.044 \times 10^{-4}\,\mathrm{erg\,G^{-2}\,mol^{-1}}$. This is consistent with a paramagnetic impurity exhibiting Curie-like behaviour.

5.4.5 Temperature Dependent Magnetisation of the Trimer Re_3Cl_9

The temperature-dependent magnetisation data of the trimer, shown in Figure 5.35, further support this interpretation. The susceptibility shows a complex temperature dependence: At high temperatures, the susceptibility approaches a constant value, towards lower temperatures a feature appears at 52 K followed by an overall crossover from diamagnetic- to paramagnetic-dominated behaviour at low temperatures. A region near zero field was excluded from analysis due to the vanishing signal-to-noise ratio of the DC scan, which results in a reduced measurement reliability. Analogous to the monomer data, the high temperature diamagnetic susceptibility is attributed to temperature-independent diamagnetism. The feature at 52 K is attributed to oxygen, but it is not as easily distinguishable this time as it overlaps with other contributions, unlike in the monomer measurement. The susceptibility then increases linearly towards low temperatures, then increasing rapidly and transitioning from diamagnetic to paramagnetic behaviour.

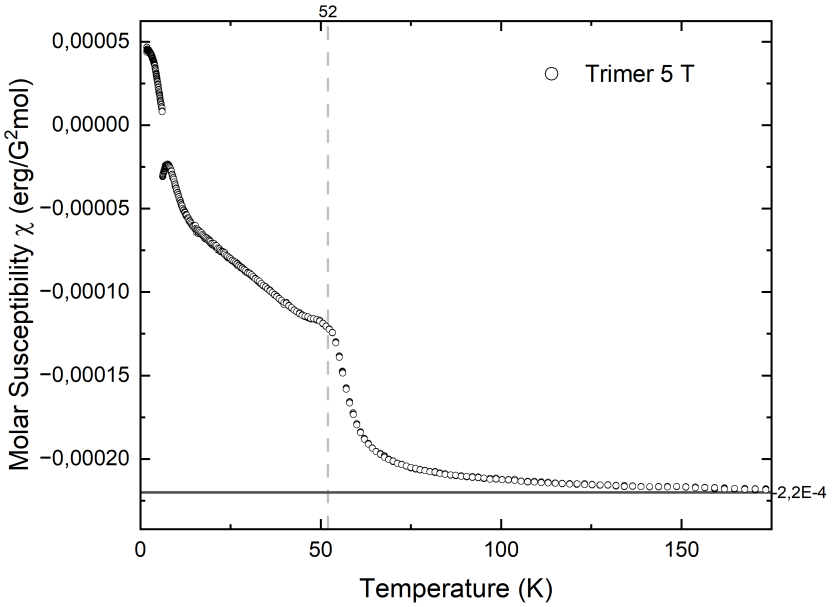


Figure 5.35: Temperature dependence of the magnetisation $M(T)$ of Re_3Cl_9 measured from 1.8 K to 175 K in an applied field of 5 T. The vertical line at 52 K marks the contribution associated with oxygen, while the horizontal line at -2.2×10^{-4} erg G^{-2} mol^{-1} marks the temperature-independent diamagnetic contribution.

5.4.6 Comparative Analysis

After the individual analysis, the data obtained for both samples, $ReCl_3$ and Re_3Cl_9, are compared and discussed together in the following. The combined $M(B)$ data of both samples is shown in Figure 5.36. From the previous fits it can be observed that the diamagnetic susceptibility of Re_3Cl_9 at 75 K is already higher than the high-temperature susceptibility of $ReCl_3$.This difference could be an indication of enhanced diamagnetic susceptibility arising from ring-current delocalisation within the trimeric core. This is further supported by the combined $M(T)$ data, shown in Figure 5.37. Both samples exhibit temperature-independent diamagnetism with superimposed paramagnetic impurity contributions and an oxygen-related anomaly near 50 K. In these measurements, high temperature data is available for both samples, showing an even higher difference between the approached susceptibilities at high temperatures of approximately 26 %. Another difference between the monomer and trimer measurements arises in the low temperature regime. The $M(T)$ data of the trimer shows an additional contribution between 10 K and 50 K. This could be some kind of weak inter-cluster exchange interactions. This contribution is absent in the monomeric $ReCl_3$ sample.

However, the collaborator responsible for the synthesis of the samples has shown some concerns about the structure of the monomeric sample. There is the hypothesis that this sample, at least partly, adopts the Re_3Cl_9 structure. This introduces uncertainty, since, if $ReCl_3$ also forms trimeric units in the solid state, the susceptibility difference can no longer be simply assigned to the enhanced diamagnetic susceptibility through aromaticity. In contrast, if the low-temperature feature in the $M(T)$ data of Re_3Cl_9 is intrinsic to the trimeric cluster, its absence in the monomeric sample supports the structural distinction between the two compounds.

The oxygen anomaly near 50 K is present in both datasets and emphasizes the importance of the sample preparation under inert conditions for measurements of such weak magnetic moments. In strongly magnetic systems, an oxygen contamination peak represents only a minor perturbation, whereas in weakly diamagnetic compounds, such as those studied here, it constitutes a large relative feature that can obscure intrinsic contributions. In the $ReCl_3$ data the anomaly is clearly resolved, whereas in Re_3Cl_9 it overlaps with cluster-based features that cannot be fully separated in its presence. Future measurements should therefore employ preparation in the glovebox to eliminate this contribution entirely.

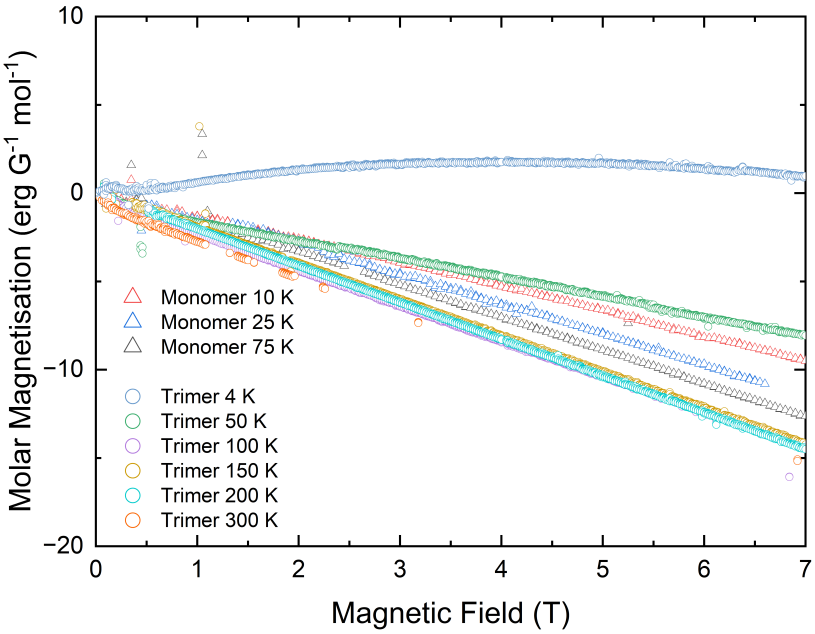


Figure 5.36: Comparing the isothermal magnetisations of $ReCl_3$ and Re_3Cl_9. The data illustrate the field-dependent magnetic response of both compounds over the full applied field range.

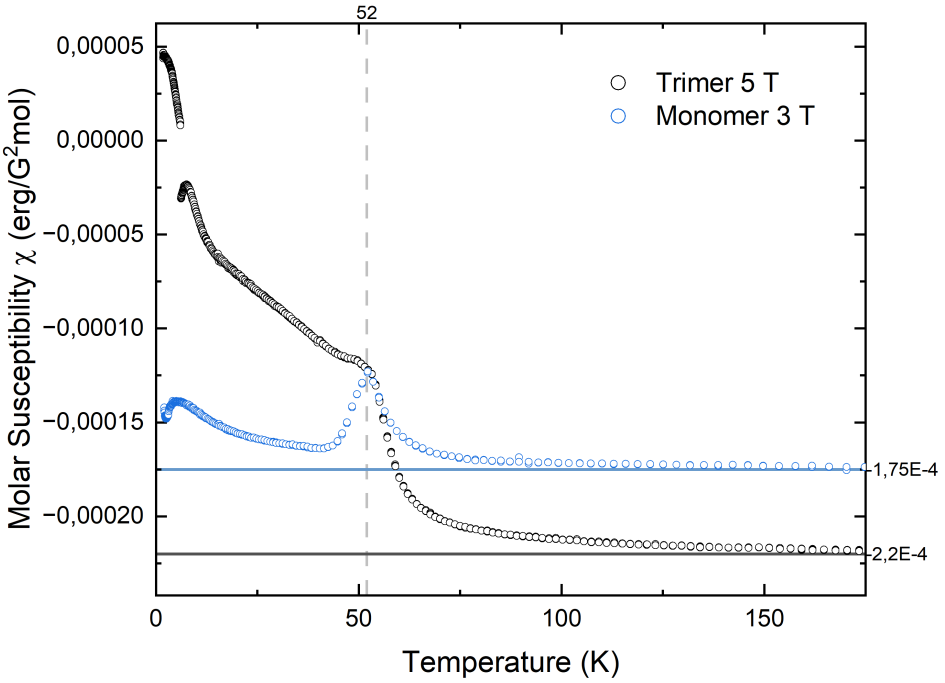


Figure 5.37: Temperature-dependent molar susceptibility of $ReCl_3$ and Re_3Cl_9, highlighting differences in low-temperature behaviour and the presence of additional temperature-dependent contributions in the trimeric system. The horizontal lines indicate the susceptibility approached at high temperatures, and the vertical line indicates the centre of the oxygen peak.

6 Conclusion and Outlook

This thesis investigated the magnetic properties of two distinct systems using SQUID magnetometry on a Quantum Design MPMS3 SQUID magnetometer, alongside the development of low-background sample holders for this instrument. The first part addressed the magnetic and electronic structure of three Fe(I) sandwich complexes, while the second part combined the design and validation of the 3D-printed sample holder with its application to Re(III) systems investigated as candidates for metal-centred aromaticity.

6.1 Fe(I) Complexes

The synthesis of Fe(I) sandwich complexes represents a rare example of a Fe(I) oxidation state stabilised by arene ligands, a combination that is both synthetically challenging and of fundamental interest to organometallic chemistry. The low oxidation state renders the metal centre highly reducing and reactive, requiring steric protection through the arene ligands and charge stabilisation by weakly coordinating counterions, while the resulting electron-rich metal centre makes these complexes a valuable model system for studying bonding in low oxidation state organometallic chemistry.

The magnetic behaviour of the three samples containing the Fe(I) sandwich complex $[Fe(HMB)_2]^+$, using the anions, with increasing size, $[PF_6]^-$, $[Al(OR^F)_4]^-$ and $[B(Ar^F)_4]^-$, was investigated using SQUID magnetometry and X-band EPR spectroscopy, confirming the spin $S = 1/2$ ground state. The $[Al(OR^F)_4]$ and $[B(Ar^F)_4]$ samples displayed ideal paramagnetic behaviour, whereas the $[PF_6]$ sample showed a clear deviation from this behaviour, with the failure of B/T scaling indicating antiferromagnetic interactions between the Fe(I) centres. This was complemented by measurements of the temperature-dependent susceptibility between 1.8 K and 300 K. These were fitted with the Curie–Weiss law and support the observations from the isothermal magnetisation data. The $[B(Ar^F)_4]^-$ and $[Al(OR^F)_4]^-$ samples showed close agreement when fitted with a Weiss temperature of $\Theta_W = 0\,\mathrm{K}$, while the fit to the $[PF_6]^-$ sample yielded $\Theta_W = 6.5(7)\,\mathrm{K}$. Plateau-like features observed in the isothermal magnetisation data at 0.4 K potentially indicate geometric frustration arising from the triangular arrangement of Fe(I) ions, which were found within the (011) and (101) crystallographic planes. This demonstrated that the magnetic response is strongly dependent on the intermolecular exchange interactions to the precise spatial arrangement of Fe(I) centres. These observations of the electronic features of this compound class, and their tunability through variation of the intermolecular spacing, open up possibilities for the design of further members of the compound class. This could lead to a more complete understanding of this not yet fully characterised group of compounds.

6.2 Sample Holder Development and Aromaticity

All-metal aromaticity has recently gained considerable interest, extending a concept long reserved for organic π-systems to clusters of metal atoms held together by delocalised bonding. As this ring current manifests macroscopically as an enhanced diamagnetic response, SQUID magnetometry is an especially interesting approach to probe it directly, since it measures the bulk magnetisation of the sample.

The investigation of metal-centred aromaticity required the development of a dedicated measurement workflow, as the expected diamagnetic moment of the sample lies below the moment of current options for powder samples, and the ring-current contribution is even weaker. This motivated the iterative development of a custom 3D-printed low-background sample holder for the Quantum Design MPMS3, fabricated by SLA 3D-printing. Starting from an initial solid-rod geometry (V0.2) and progressing through snap-fit (V1.X) and compression-based (V3.X) designs, leading to the compression holder (V3.1) which was employed throughout this thesis. The design evolution was guided by criteria identified from background measurements, being the minimisation of part count within the active detection region, strict maintenance of rotational symmetry, and reliable positional reproducibility across repeated loading cycles. The background characterisation demonstrated that the dominant SQUID response of the sample holder originates from local geometric variations in magnetic volume passing through the gradiometer detection coils, which has been optimised to be mostly homogeneous throughout the measurement zone. The background signal was shown to be highly reproducible across repeated measurements at the same field, with reproducibility improving markedly with increasing applied field. Validation against reference samples spanning a wide range of susceptibility magnitudes revealed a clear pattern that the process overestimates the holder's contribution to the measured signal, slightly offsetting the corrected moment for both GGG (deviation increasing from 0.15 % to 0.33 %) and Pd (from 1 % to 3 %). For the weakly diamagnetic samples anthracene and naphthalene, no susceptibilities could be determined without background subtraction, as their magnetic moment lies below the residual background inherent to the available and printed sample holder. This is a consequence of using the internal calibration, which was performed with the Pd reference sample in a brass sample holder, and can be resolved by using a calibration factor obtained using the background subtracted data from the 3D-printed sample holder. Although the background signal is comparable in magnitude to that of the conventional Quantum Design brass sample holder and capsule, the reproducible positioning achieved by the design developed in this work makes background subtraction considerably more reliable, resulting in the determination of the susceptibility of antharcene within 2% of the reference value. The higher deviations in naphthalene were due to non ideal settings of the MPMS3 and could be certainly improved when following the final workflow described in Section A.1. The validated sample holder was subsequently applied to the magnetic characterisation of $ReCl_3$ and Re_3Cl_9 as candidates for metal-centred aromaticity. $ReCl_3$ displayed spin-chain features, and both showed an oxygen contamination peak near 50 K, attributed to the phase transition of O_2 at 43.8 K, and paramagnetic contributions from impurities at low temperatures. The temperature-dependent susceptibility measurements show a difference in the diamagnetic susceptibilities approached at high temperatures of 25%, with the Re_3Cl_9 showing the

stronger diamagnetism, consistent with the hypothesis of enhanced diamagnetism due to ring-currents, and clearly larger than the uncertainties from the sample holder workflow.

The sample holder developed in this work significantly extends the accessible sensitivity range of the MPMS3 for diamagnetic and weakly paramagnetic compounds, and is expected to serve as a foundation for broader investigations of metal-centred aromaticity and related phenomena. Future improvements to the sa,ple holder should focus on two aspects. First, the systematic over-correction identified should be adressed by evaluating the use of a sample holder specific calibration factor. Second, a subsequent refinement (V3.2), incorporating radial guide structures to improve centring within the MPMS3 bore, was completed too late to be used for the measurements presented in this thesis but represents a starting point for future work. Another interesting, while most probably small, correction for the sample holder is the calibration of the auto tracking feature [65]. This is especially valuable for temperature-dependent susceptibility measurements. Additionally, several questions raised by the rhenium analysis remain open. Further structural characterisation would also help clarify the ambiguity between $ReCl_3$ and Re_3Cl_9. Reducing oxygen contamination during sample handling would yield a cleaner signal in the low-temperature region, removing the need to account for the O_2 peak. Finally, additional measurements covering a wider temperature range, alongside the data already obtained, would allow the aromaticity hypothesis to be tested more precisely. Another sample worth measuring is $Re_2Cl_8^-$, which is currently being prepared but was not ready in time to be measured in this work. This should replace the $ReCl_3$ sample as a reference.

A Appendix

A.1 Practical Guidelines for Use of the 3D-Printed Sample Holder

To fully exploit the low-background performance of the developed sample holder, sample preparation and measurement procedures should be carried out in a consistent and reproducible manner. All samples should be prepared and handled under inert conditions, irrespective of their chemical stability. This is necessary as the paramagnetic oxygen contribution present under ambient conditions produces a signal that can become large compared to the magnetic moments of the investigated samples. Sample mass determination should be performed using repeated weighing of both the empty and loaded lower section of the holder. The sample holder should be produced using the workflow and settings described in Table 3.1. All tools used for handling, weighing and loading samples should be non-magnetic, since trace ferromagnetic contamination can dominate the signal of weakly magnetic samples. Impurities should be minimised throughout handling, beginning already at the post-processing stage. The printed parts should only be handled while wearing gloves and ideally be stored in sealed containers between uses. If necessary, the sample holder can be cleaned with ethanol or isopropanol, while acetone should not be used. Cleaning should never be carried out between the sample measurement and its corresponding background measurement to prevent leftover cleaning solvent. To ensure reproducible assembly, threaded sample holder designs should be marked across the threaded section after final closure. This allows the holder to be reassembled in the same position and minimises geometric variations between sample and background measurements. Background and sample measurements must be performed using identical measurement protocols. The background measurement should ideally be performed first, since the holder must not be cleaned in between, and performing it second could otherwise leave behind residual sample material or cleaning solvent. DC scans should be performed using a scan length of 30 mm and a scan time of at least 12 s. At each measurement point, sufficient time should be allowed for complete stabilisation of both temperature and magnetic field before data acquisition. The centre position should be set manually and kept identical for both sample and background measurements. For the sample holder V3.1 this corresponds to 71 mm. The SQUID range should be fixed throughout the measurement. A range setting of 1 is recommended whenever the sample moment allows it. All DC scans should be inspected visually. Agreement between repeated measurements provides an important validation of data quality and helps identify unreliable data sets. Finally, the MPMS3 magnet should be degaussed before each measurement. This minimises residual magnetic fields arising from trapped flux in the superconducting coils and improves the reproducibility of both background and sample measurements.

A.2 Pictures of the 3D-Printed Sample Holder

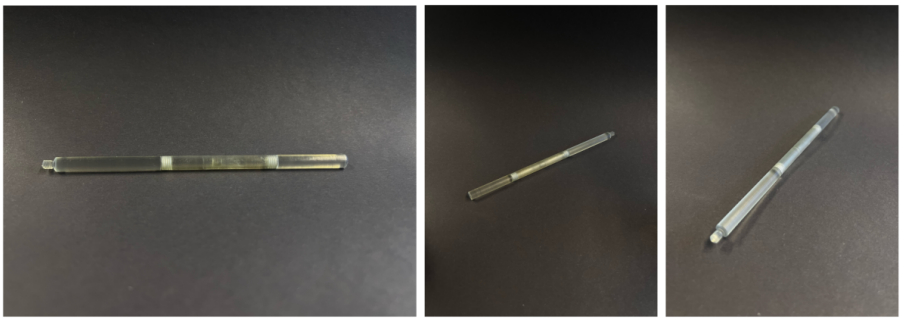


Figure A.1: Pictures taken of sample holder V3.1 in assembled state.

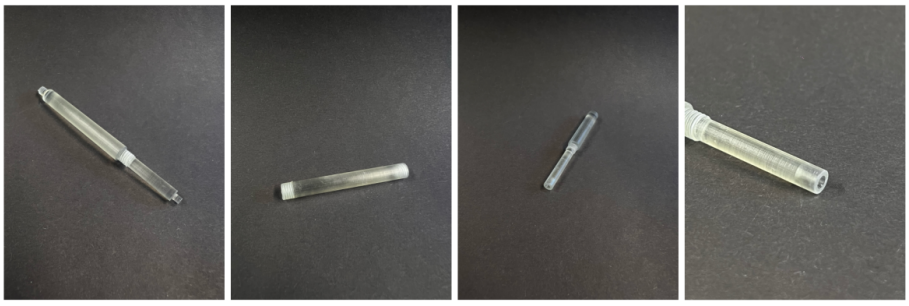


Figure A.2: Pictures taken of sample holder V3.1 in disassembled state.

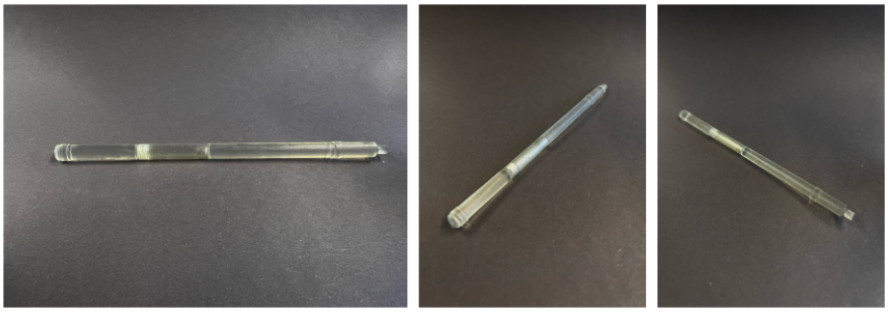


Figure A.3: Pictures taken of sample holder V3.2 in assembled state.

A.3 Detailed Plots of the Reproducability assesment

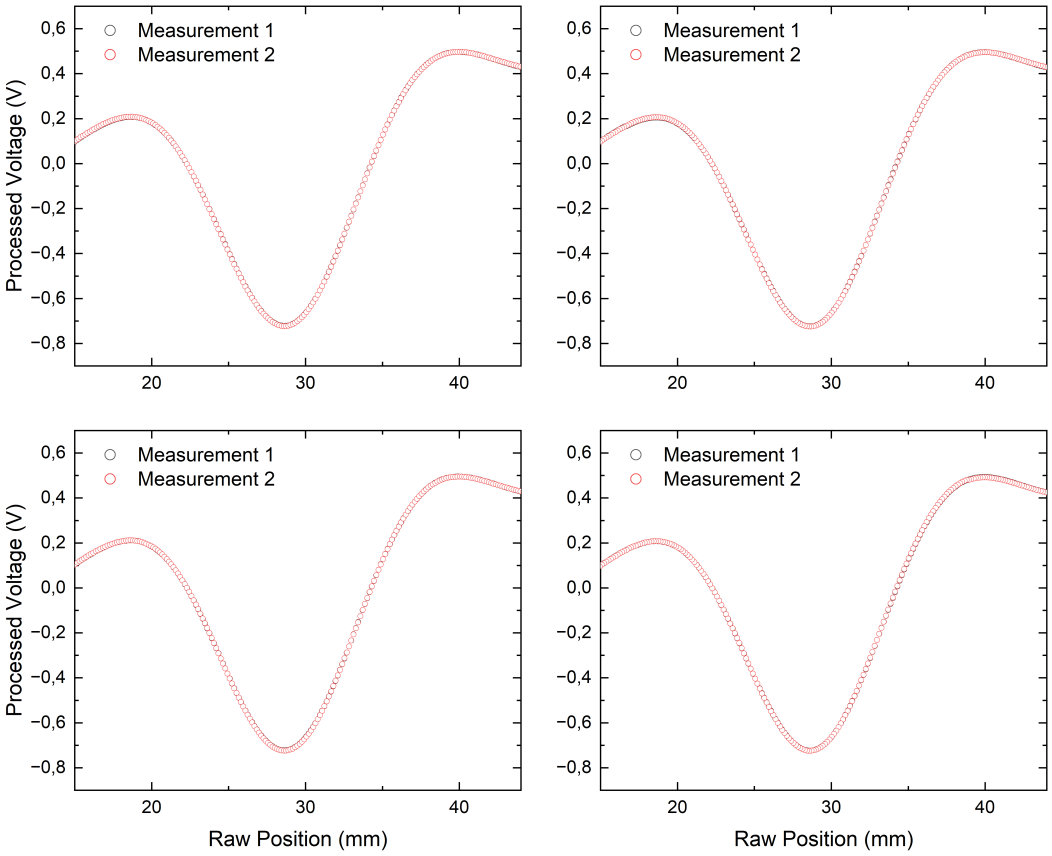


Figure A.4: Individual scans of two consecutive background measurements of the empty 3D-printed sample holder V3.1 at 300 K and 1 T, arranged as panels for direct assessment of scan-to-scan variation.

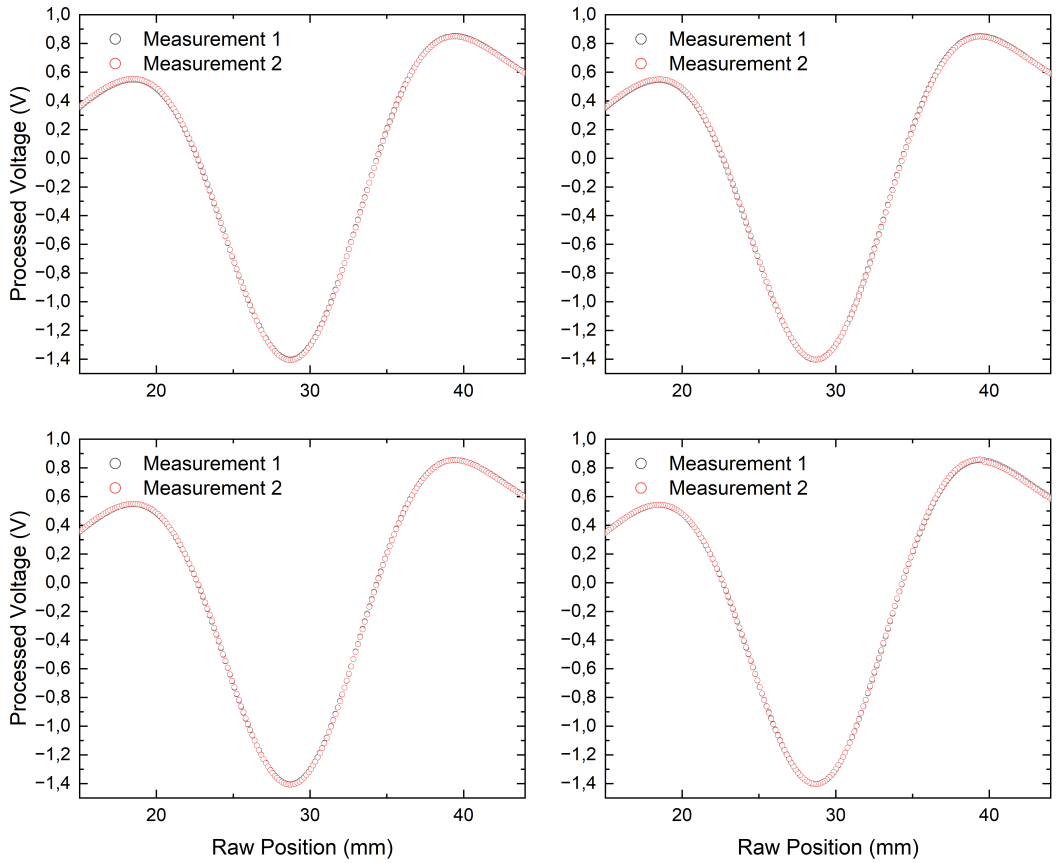


Figure A.5: Individual scans of two consecutive background measurements of the empty 3D-printed sample holder V3.1 at 300 K and 2 T, arranged as panels for direct assessment of scan-to-scan variation.

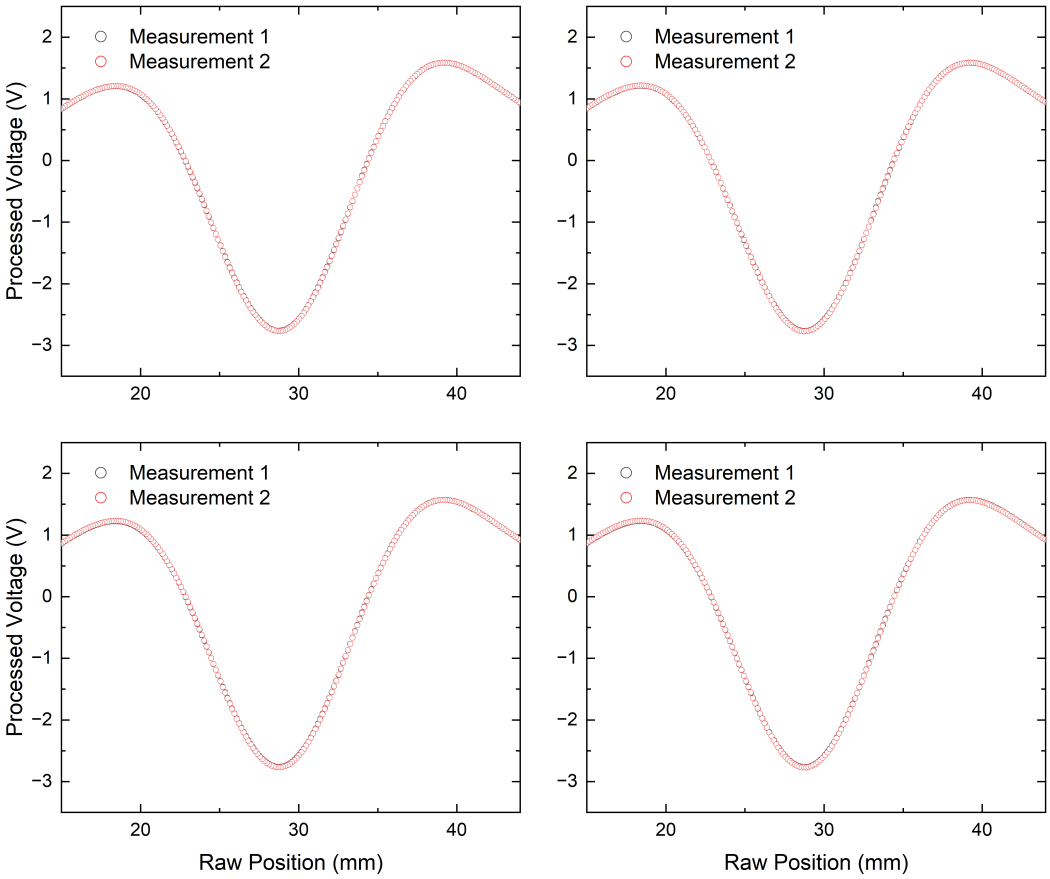


Figure A.6: Individual scans of two consecutive background measurements of the empty 3D-printed sample holder V3.1 at 300 K and 4 T, arranged as panels for direct assessment of scan-to-scan variation.

List of Figures

2.1 Magnetisation of an ensemble of non-interacting paramagnets as described by the Brillouin function for different total angular momentum quantum numbers J. Taken from [5]. 6

2.2 Temperature dependence of the susceptibility of an ensemble of non-interacting paramagnets described by the Curie law, shown as (a) χ vs. T, (b) $1/\chi$ vs. T, and (c) χT vs. T. Adapted from [5]. 8

2.3 Temperature dependence of the magnetic susceptibility of an ensemble of interacting magnetic moments according to the Curie–Weiss law (Equation (2.24)) represented as (a) magnetic susceptibility χ, (b) reciprocal susceptibility $1/\chi$, (c) susceptibility–temperature product χT. Taken from [11]. 12

2.4 Schematic illustration of antiferromagnetically coupled spins on an unfrustrated square lattice (a) and a geometrically frustrated triangular lattice (b). Adapted from [5]. 14

2.5 Schematic illustration of an induced ring current in an aromatic system in the presence of an applied magnetic field B_0. The applied field induces a circulation of π-electrons around the ring, resulting in a diamagnetic response. Adapted from [25]. 15

3.1 Illustration showing (a) a dc-SQUID with the superconducting loop containing two Josephson junctions, (b) the flux-locked loop feedback circuit for the dc-SQUID. Adapted from [27]. 19

3.2 Schematic illustration of the SQUID signal generation in an MPMS3, showing the second order gradiometer with a sample moving through it, the connection to the SQUID and the generated Signal. Adapted from [1]. 19

3.3 Representative static field SQUID scan measured using a MPMS3, together with a fit based on the dipole transfer function. The model accounts for the pickup coil geometry and sample position along the scan axis, enabling extraction of the magnetic moment. Taken from [28]. 20

3.4 Sample mounting options for the MPMS3. From top to bottom: brass sample holder (Quantum Design MPMS 3 Brass Trough Sample Holder, QDC-4500-608), plastic straw (Quantum Design Standard Sample Holder, QDC-8000-001) with straw adapter (Quantum Design ACMS II straw adapter assembly, QDC-4084-814), quartz sample holder (MPMS 3 Quartz Paddle Sample Holder, QDC-4500-604), and plastic capsule (Quantum Design VSM powder sample holder, 4096-388) used with the brass sample holder. Taken from [1, 29]. 22

3.5 Sample mounting and positioning tool supplied with the MPMS3, used for aligning samples for measurements. Taken from [1]. 23
3.6 Effect of a 1 mm positional offset between sample and background DC scans on the subtracted signal, which ideally represents the isolated sample moment. Results are shown for decreasing ratios of sample moment $p(T)$ to background moment $p(bkg)$ from left to right. Adapted from [30]. 24
3.7 Graphical user interface of the Quantum Design MPMS3 Sample Geometry Simulator used to determine the correction factor for the magnetic moment of samples with non-standard geometries. Taken from [32]. 25
3.8 Schematic of EPR spectroscopy for a single unpaired electron spin. (a) Zeeman splitting of the $m_s = \pm 1/2$ energy levels of a spin-1/2 system upon application of an external magnetic field. At the resonance field B_R, resonant absorption occurs, manifesting as an absorption peak shown in (b), together with its derivative, which is typically recorded in EPR measurements. Adapted from [33]. 26
3.9 Schematic representation of the SLA 3D-printing process., showing an UV laser selectively curing a liquid photopolymer resin layer by layer to form a solid 3D structure. Adapted from [37]. 28

4.1 Molecular structure of the investigated Fe(I) complex, showing (a) a view focussing on one HMB ligand, and (b) the overall sandwich-type coordination geometry. Colour scheme: Fe (orange), C (grey), H (white). 31
4.2 Molecular orbital diagram showing two possible electronic configurations of the Fe(I) ion in the Fe(I) complex. The two cases differ in the symmetry and occupation of the SOMO. The labels π^*, σ, δ, and π denote the bonding character of the molecular orbitals, while e_{1g}, e_{2g}, and a_{1g} indicate their symmetry. Adapted from [46]. 32
4.3 Anions used in Fe(I) samples, arranged in order of increasing size from (a) to (c). Colour scheme: F (yellow), P (orange), Al (dark grey), O (red), C (light grey), B (green), H (white). 33
4.4 Field-dependent isothermal magnetisation of $[Fe(HMB)_2][PF_6]$ measured between 0 T and 7 T at temperatures of 1.8 K (black), 3 K (blue), and 5 K (red), shown in units of μ_B per formula unit. (a) Magnetic moment M as a function of applied field B. (b) Magnetic moment with the field axis rescaled by temperature to highlight magnetic interactions. 36
4.5 Temperature dependence of the molar magnetic susceptibility $\chi(T)$ and inverse susceptibility $\chi^{-1}(T)$ of $[Fe(HMB)_2][PF_6]$ measured at applied fields of 0.1 T (blue) and 1 T (black). The solid green line represents a Curie–Weiss fit to $\chi^{-1}(T)$ in the high-temperature region. 37
4.6 Field-dependent isothermal magnetisation of $[Fe(HMB)_2][PF_6]$ measured between 0 T and 7 T at temperatures of 0.4 K (grey), 1.8 K (black), 3 K (blue), and 5 K (red), shown in units of μ_B per formula unit. (a) Magnetic moment M as a function of applied field B. (b) The same data plotted as a function of B/T to assess scaling behaviour and deviations indicative of magnetic interactions. 38

4.7 Isothermal magnetisation and its Derivative $\mathrm{d}M/\mathrm{d}B$ of $[Fe(HMB)_2][PF_6]$ measured at 0.4 K using the ^{3}He option. 39
4.8 Crystallographic planes of the solid state crystal structure of $[Fe(HMB)_2][PF_6]$, in which triangular lattice motifs were found. 40
4.9 Temperature dependence of the susceptibility $\chi(T)$ and inverse susceptibility $\chi^{-1}(T)$ of $[Fe(HMB)_2][PF_6]$ measured from 0.4 K to 4 K. 40
4.10 Field-dependent isothermal magnetisation of $[Fe(HMB)_2]$ $[Al(OR^F)_4]$ measured between 0 T and 7 T at temperatures of 1.8 K (black), 3 K (blue), and 5 K (red), shown in units of μ_B per formula unit. (a) Magnetic moment M as a function of applied field B. (b) Magnetic moment with the field axis rescaled by temperature. 41
4.11 Temperature dependence of the molar magnetic susceptibility $\chi(T)$ and inverse susceptibility $\chi^{-1}(T)$ of $[Fe(HMB)_2][Al(OR^F)_4]$ measured at an applied field of 1 T. The solid green line represents a Curie–Weiss fit to $\chi^{-1}(T)$ in the high-temperature region. 42
4.12 Field-dependent isothermal magnetisation of $[Fe(HMB)_2][B(Ar^F)_4]$ measured between 0 T and 7 T at temperatures of 1.8 K (black), 3 K (blue), and 5 K (red), shown in units of μ_B per formula unit. (a) Magnetic moment M as a function of applied field B. (b) Magnetic moment with the field axis rescaled by temperature 43
4.13 Temperature dependence of the molar magnetic susceptibility $\chi(T)$ and inverse susceptibility $\chi^{-1}(T)$ of $[Fe(HMB)_2][B(Ar^F)_4]$ measured at applied fields of 0.1 T (blue) and 1 T (black). The solid green line represents a Curie–Weiss fit to $\chi^{-1}(T)$ in the high-temperature region. 44
4.14 Field-dependent isothermal magnetisation of all samples with the field axis rescaled by temperature, including sub-Kelvin ^{3}He data for $[Fe(HMB)_2][PF_6]$. The dashed line indicates the saturation magnetisation expected for a spin-1/2 system with $g = 2$. 45
4.15 Temperature dependence of the molar magnetic susceptibility $\chi(T)$ and inverse susceptibility $\chi^{-1}(T)$ of all samples measured at 1 T. Curie–Weiss fits to $\chi^{-1}(T)$ in the high-temperature region are shown as green solid lines. . . 46
4.16 Temperature dependence of χT for all Fe(I) samples measured at 1 T. The pronounced maximum near 50 K is attributed to trace oxygen contamination. The grey region highlights the range in which this peak was observed across all three samples. 48

5.1 Schematic representation of a sample holder with a centrally positioned sample volume. Guide structures are symmetrically placed outside the measurement region to ensure reproducible radial centring of the sample holder. Taken from [57]. 52
5.2 Schematic representation of the 3D-model of sample holder V0.1 including dimensions (in mm), employed in initial tests to assess compatibility with the MPMS3 as well as manufacturing quality and dimensional accuracy. 53
5.3 Schematic representation of the 3D-model of sample holder design V0.2, including dimensions (in mm), illustrating both the assembled and disassembled states of the design, which is composed of three components. 54

5.4 Background measurement of the 3D-printed solid rod (V0.2) at 300 K and 1 T. (a) Processed voltage as a function of scan position. (b) The same data including a dipole fit to the signal of the threaded region. 55
5.5 DC scans of the 3D-printed sample holder (V0.2). The left panel shows raw scan data recorded at a constant applied magnetic field of 1 T at temperatures of 1.8 K, 100 K, and 300 K. The right panel shows measurements performed at 300 K at applied magnetic fields of 0.1 T, 1 T, and 7 T. 56
5.6 Schematic representation of the 3D-model of the sample holder V1.1, illustrating both the assembled and disassembled states. The three distinct parts of the main rod are shown in (a) from the top-down view, in (b) in the assembled state from the same view, and in (c) in the assembled state from the side view. Finally, (d) shows a 3D view of the assembled main rod and the lid to better visualise the snap fit mechanism. 57
5.7 DC-Scans of the 3D-printed sample holder, snap-fit design V(1.1) with cubic sample volume, at 300 K and 1 T. The marked positions indicate the sample volume (28.75 mm) and the thread (58.75 mm). 58
5.8 Schematic representation of the 3D-model of the sample holder V2.1, showing both the assembled (a) and disassembled (b) states of the design, with an additional focus on the central part containing the sample volume (c). . . . 59
5.9 DC scans of the 3D-printed sample holder V2.1 at 300 K and 1 T. The marked positions indicate the sample volume (28.75 mm) and the thread (58.75 mm). 59
5.10 Schematic representation of the 3D-model of sample holder V3.1, illustrating both the assembled (a) and disassembled states (b), (c) of the design. . . . 60
5.11 Detailed view of the central section of the sample holder V3.1, showing the dimensions of the sample volume, which is highlighted in blue. 61
5.12 DC scans of the 3D-printed sample holder V3.1 at 300 K and 1 T. The marked position indicates the position of the sample volume (29 mm). 62
5.13 Schematic representation of sample holder V3.2, illustrating both the assembled (a),(b) and disassembled (c) states of the design. 62
5.14 Raw SQUID DC scans of 3D-printed sample holders measured at 300 K and 1 T, comparing successive design iterations. (a) shows the measurement of Versions 0.2, 1.1 and 2.1, while (b) shows the measurements of Version 2.2 and 3.1. 63
5.15 Simulated MPMS3 second-order gradiometer response to a single point-like magnetic dipole located at the coil centre (dashed vertical line at 0 mm). The signal is normalised to its maximum absolute value. 65
5.16 Simplified three-dipole simulation of the sample holder response (black) compared with a measurement (red). The three dipoles represent the main sample region and the two threaded connection areas. 66
5.17 Three-dipole simulation including an additional linear background term (black) compared with the measurement (red). The linear contribution improves the agreement with the measured data relative to the model without it. 67
5.18 Three-dipole simulation including the linear term, showing the separated contribution of each dipole together with their sum. The individual responses superimpose to produce the total simulated signal. 67

5.19 Volume profile along the SQUID measurement axis of the 3D-printed sample holder V3.1, with the design above for reference. Shown are the contributions of the top part (blue), bottom part (green), and central outer shell (orange), together with their sum (black). 68
5.20 Final simulation (black) based on the volume profile along the SQUID measurement axis (blue) of the 3D-printed sample holder V3.1, in comparison to the measured data (red). 69
5.21 Individual scans of two consecutive background measurements of the empty 3D-printed sample holder V3.1 at 300 K and 0.1 T, arranged as panels for direct assessment of scan-to-scan variation. 70
5.22 Overlay of two consecutive background measurements of the empty 3D-printed sample holder V3.1 at 300 K and 0.1 T, demonstrating the reproducibility of the measured voltage profile. 71
5.23 Average background signal of the empty 3D-printed holder with standard deviation, measured at 300 K for applied fields of (a) 0.1 T, (b) 1 T, (c) 2 T, and (d) 4 T. Each average is taken over all scans from two consecutive measurements. The scan-to-scan consistency improves with increasing field. 72
5.24 Comparison of the background profiles of both empty holders, the QD capsule in th standard Quantum Design brass holder and the 3D-printed sample holder V3.1 developed in this work, at 300 K and 1 T. 73
5.25 Subtraction of the sample holder background for the (a) commercial Quantum Design capsule in the brass holder and (b) the 3D-printed sample holder V3.1. The corrected sample signal (blue) is obtained by subtracting the DC scan of the empty sample holder (black) from the scan of the sample within the sample holder (red). The scans were performed at 300 K and 1 T 74
5.26 Isothermal magnetisation of the GGG AC calibration reference measured using the 3D-printed sample holder (a) with and without background correction, and the standard brass holder (b). 76
5.27 Isothermal magnetisation at 300 K from -2 T to 2 T of the palladium reference sample measured in the brass holder (a) and the 3D-printed holder (b), with and without background subtraction. 77
5.28 Aromatic test samples used for validation of the 3D-printed sample holder. Both are polycyclic aromatic hydrocarbons composed of fused benzene rings, serving as representative weakly diamagnetic π-conjugated systems. 78
5.29 Isothermal molar magnetisation as a function of applied magnetic field measured from 0 T to 7 T for naphthalene (a) and anthracene (b) using the 3D-printed sample holder (Version 3.1). The experimental data are compared with literature values from [62]. 79
5.30 Rhenium(III) chloride complexes investigated as reference systems for probing metal-centred aromaticity: the mononuclear $ReCl_3$ (a) and the trinuclear Re_3Cl_9 (b). Colour scheme: Re (purple), Cl (green). 81
5.31 Corrections applied to the isothermal magnetisation $M(B)$ of $ReCl_3$ measured between 0 T and 7 T at 10 K (a) and 75 K (b). 83

5.32 Isothermal magnetisation of $ReCl_3$ measured from 0 T to 7 T at 10 K, 25 K, and 75 K. The 10 K and 75 K datasets have been corrected for the artefacts from the readout electronics. Linear fits ($M = \chi B + \chi_0$) to the data for $2\,\mathrm{T} \leq B \leq 7\,\mathrm{T}$ are shown, with the obtained susceptibilities indicated by the adjacent labels. 84
5.33 Temperature dependence of the magnetisation $M(T)$ of $ReCl_3$. (a) shows the isothermal magnetisation $M(T)$ measured between 1.8 K and 175 K with the horizontal line indicating the approached diamagnetic susceptibility at high temperatures and the vertical line marking the centre of the oxygen peak. (b) Shows a magnified view of the low-temperature region between 0 K and 15 K. 85
5.34 Isothermal magnetisation $M(B)$ of Re_3Cl_9 measured between 0 T and 7 T. (a) Displays all recorded temperatures between 1.8 K and 300 K, and (b) shows the magnetisation curves at 4 K and 150 K, the 4 K from which the temperature independent diamagnetic contribution was subtracted, and a Brillouin function fit to this corrected data. 86
5.35 Temperature dependence of the magnetisation $M(T)$ of Re_3Cl_9 measured from 1.8 K to 175 K in an applied field of 5 T. The vertical line at 52 K marks the contribution associated with oxygen, while the horizontal line at $-2.2 \times 10^{-4}\,\mathrm{erg\ G^{-2}\ mol^{-1}}$ marks the temperature-independent diamagnetic contribution. 87
5.36 Comparing the isothermal magnetisations of $ReCl_3$ and Re_3Cl_9. The data illustrate the field-dependent magnetic response of both compounds over the full applied field range. 88
5.37 Temperature-dependent molar susceptibility of $ReCl_3$ and Re_3Cl_9, highlighting differences in low-temperature behaviour and the presence of additional temperature-dependent contributions in the trimeric system. The horizontal lines indicate the susceptibility approached at high temperatures, and the vertical line indicates the centre of the oxygen peak. 89

A.1 Pictures taken of sample holder V3.1 in assembled state. 96
A.2 Pictures taken of sample holder V3.1 in disassembled state. 96
A.3 Pictures taken of sample holder V3.2 in assembled state. 96
A.4 Individual scans of two consecutive background measurements of the empty 3D-printed sample holder V3.1 at 300 K and 1 T, arranged as panels for direct assessment of scan-to-scan variation. 97
A.5 Individual scans of two consecutive background measurements of the empty 3D-printed sample holder V3.1 at 300 K and 2 T, arranged as panels for direct assessment of scan-to-scan variation. 98
A.6 Individual scans of two consecutive background measurements of the empty 3D-printed sample holder V3.1 at 300 K and 4 T, arranged as panels for direct assessment of scan-to-scan variation. 99

List of Tables

2.1 Pascal's constants and representative diamagnetic susceptibilities of the compounds analysed in this thesis. Adapted from [7]. 10

3.1 Summary of printing, washing and curing parameters, as well as the materials and devices used for fabrication of the sample holders. 30

4.1 Fe(I) complexes, counterions, and Fe–Fe distances derived from CIFs obtained through XRD measurements, including the nearest-neighbour distance and the average Fe–Fe separation. 33
4.2 Molar masses and sample masses of the investigated Fe(I) compounds used for SQUID magnetometry measurements. 34
4.3 Weiss temperatures Θ_W obtained from Curie–Weiss fits to the inverse susceptibility of $[Fe(HMB)_2][PF_6]$ using different fitting ranges. The reference fit range is 50 K to 250 K. 38
4.4 Comparison of the g-factors determined by X-band EPR spectroscopy and by SQUID magnetometry. The EPR values are given as the RMS average of the anisotropic g-tensor, while the magnetometry values are obtained from fits to the $M(B)$ and $M(T)$ data. 47

5.1 Average ratio of the standard deviation to the absolute voltage signal across all scans, for each applied field. 71
5.2 Molar magnetic susceptibility of the GGG reference sample determined from linear fits to the isothermal magnetisation data for different holder configurations, compared with the literature range. 75
5.3 Magnetic susceptibility of the palladium reference sample measured in the standard brass sample holder and the 3D-printed sample holder (V3.1), with and without background correction, compared with the theoretical value. . 77
5.4 Molar magnetic susceptibilities of naphthalene and anthracene determined from linear fits to the field-dependent molar magnetisation measured using the 3D-printed sample holder (Version 3.1), in comparison to literature values from [61]. 79
5.5 Summary of obtained susceptibilities for all reference samples in the 3D-printed holder, before and after background correction, ordered by decreasing susceptibility magnitude. 80
5.6 Masses and molar masses of the Re(III) samples used for SQUID magnetometry measurements. 82

5.7 Temperature-dependent molar magnetic susceptibility of $ReCl_3$ determined from linear fits to the $M(B)$ data. In the third column, the deviations from the Pascal diamagnetic estimate $\chi_{\mathrm{Pascal}} = -99 \times 10^{-6}\,\mathrm{erg\,G^{-2}\,mol^{-1}}$ is given by $\chi/\chi_{\mathrm{Pascal}}$. 83

Bibliography

[1] *MPMS3 SQUID Magnetometer User Manual*. Quantum Design. 2016.

[2] E. Beaumier, A. Pearce, X. See, and I. Tonks. "Modern applications of low-valent early transition metals in synthesis and catalysis". In: *Nature Reviews Chemistry* 3 (Nov. 2018). DOI: 10.1038/s41570-018-0059-x.

[3] L. Alvarado-Soto, R. Ramirez-Tagle, and R. Arratia-Pérez. "Spin–orbit Effects on the Aromaticity of the Re_3Cl_9 and Re_3Br_9 Clusters". In: *Chem. Phys. Lett.* 467 (2008), pp. 94–96.

[4] S. Mugiraneza and A. M. Hallas. "A beginner's guide to interpreting magnetic susceptibility data with the Curie-Weiss law". In: *Commun. Phys.* 5 (2022), p. 95. DOI: 10.1038/s42005-022-00853-y.

[5] S. J. Blundell. *Magnetism in Condensed Matter*. Oxford: Oxford University Press, 2001.

[6] R. L. Carlin. *Magnetochemistry*. Berlin, Heidelberg: Springer-Verlag, 1986.

[7] G. A. Bain and J. F. Berry. "Diamagnetic Corrections and Pascal's Constants". In: *J. Chem. Educ.* 85.4 (2008), pp. 532–536. DOI: 10.1021/ed085p532.

[8] P. W. Selwood. *Magnetochemistry*. New York: Interscience, 1956.

[9] O. Kahn. *Molecular Magnetism*. New York: Wiley-VCH, 1993.

[10] J. Clarke and A. I. Braginski, eds. *The SQUID Handbook: Fundamentals and Technology of SQUIDs and SQUID Systems*. Weinheim: Wiley-VCH, 2004.

[11] M. Bałanda and R. Pełka. "Magnetism". In: *Molecular Magnetic Materials*. John Wiley & Sons, Ltd, 2017. Chap. 1, pp. 1–28. DOI: 10.1002/9783527694228.ch1.

[12] N. D. Mermin and H. Wagner. "Absence of Ferromagnetism or Antiferromagnetism in One- or Two-Dimensional Isotropic Heisenberg Models". In: *Physical Review Letters* 17.22 (1966), pp. 1133–1136. DOI: 10.1103/PhysRevLett.17.1133.

[13] J. Martínez-Lillo, T. F. Mastropietro, E. Lhotel, C. Paulsen, J. Cano, G. De Munno, J. Faus, F. Lloret, M. Julve, S. Nellutla, and J. Krzystek. "Highly Anisotropic Rhenium(IV) Complexes: New Examples of Mononuclear Single-Molecule Magnets". In: *Journal of the American Chemical Society* 135.37 (2013). PMID: 23957361, pp. 13737–13748. DOI: 10.1021/ja403154z.

[14] C. Lacroix, P. Mendels, and F. Mila, eds. *Introduction to Frustrated Magnetism: Materials, Experiments, Theory*. Vol. 164. Springer Series in Solid-State Sciences. Berlin, Heidelberg: Springer, 2011. DOI: 10.1007/978-3-642-10589-0.

[15] IUPAC. *Aromaticity*. IUPAC Compendium of Chemical Terminology (the Gold Book). 2014.

[16] E. Hückel. "Quantentheoretische Beiträge zum Benzolproblem". In: *Z. Phys.* 70 (1931), pp. 204–286.

[17] P. von Ragué Schleyer, C. Maerker, A. Dransfeld, H. Jiao, and N. J. R. van E. Hommes. "Nucleus-Independent Chemical Shifts: A Simple and Efficient Aromaticity Probe". In: *Chem. Rev.* 96.3 (1996), pp. 1047–1070. DOI: 10.1021/cr940046r.

[18] A. I. Boldyrev and L.-S. Wang. "All-metal aromaticity and antiaromaticity". In: *Chem. Rev.* 105.10 (2005), pp. 3716–3757. DOI: 10.1021/cr0300851.

[19] X. Li, A. E. Kuznetsov, H.-F. Zhang, A. I. Boldyrev, and L.-S. Wang. "Observation of all-metal aromatic molecules". In: *Science* 291.5506 (2001), pp. 859–861. DOI: 10.1126/science.1056765.

[20] Z. Badri, S. Pathak, H. Fliegl, P. Rashidi-Ranjbar, R. Bast, R. Marek, C. Foroutan-Nejad, and K. Ruud. "All-Metal Aromaticity: Revisiting the Ring Current Model among Transition Metal Clusters". In: *Journal of Chemical Theory and Computation* 9.11 (2013), pp. 4789–4796. DOI: 10.1021/ct4007184.

[21] R. Gershoni-Poranne and A. Stanger. "Magnetic Criteria of Aromaticity". In: *Chemical Society Reviews* 44.18 (2015), pp. 6597–6615. DOI: 10.1039/C5CS00114E.

[22] M. Dimitrova and D. Sundholm. "Current Density, Current-Density Pathways, and Molecular Aromaticity". In: *Aromaticity: Modern Computational Methods and Applications*. Ed. by I. Fernández. Amsterdam: Elsevier, 2021, pp. 155–194. DOI: 10.1016/B978-0-12-822723-7.00005-4.

[23] M. Solà and A. Muñoz-Castro. "Aromaticity of All-Metal Clusters". In: *Chemical Communications* 61 (2025), pp. 14280–14291. DOI: 10.1039/D5CC03842A.

[24] M. Solà, F. Feixas, J. O. C. Jiménez-Halla, E. Matito, and J. Poater. "A Critical Assessment of the Performance of Magnetic and Electronic Indices of Aromaticity". In: *Symmetry* 2.2 (2010), pp. 1156–1179. DOI: 10.3390/sym2021156.

[25] S. Shaik, D. Danovich, and P. C. Hiberty. "On the Nature of the Chemical Bond in Valence Bond Theory". In: *J. Chem. Phys.* 157 (2022), p. 090901. DOI: 10.1063/5.0095953.

[26] B. D. Josephson. "Possible New Effects in Superconductive Tunnelling". In: *Physics Letters* 1.7 (1962), pp. 251–253. DOI: 10.1016/0031-9163(62)91369-0.

[27] R. Gross and A. Marx. *Applied Superconductivity: Josephson Effect and Superconducting Electronics*. Lecture manuscript, WS 2003/2004–2009/2010. Garching, 2010.

[28] Quantum Design. *Background Subtraction Using the MPMS3*. Tech. rep. Application Note 1500-023, Rev. A0. San Diego, CA, USA: Quantum Design, 2019.

[29] Quantum Design. *MPMS3 Improving Accuracy*. Technical presentation (Pharos Portal). Accessed via Quantum Design Pharos document repository. n.d.

[30] Quantum Design. *Sample Mounting Considerations*. Tech. rep. Application Note 1014-201. San Diego, CA, USA: Quantum Design, 2014.

[31] Quantum Design. *Palladium Reference Samples*. Application Note 1041-001, Rev. A1.

[32] Quantum Design. *Accuracy of Reported Sample Moment: Using the Sample Geometry Simulator*. Tech. rep. Application Note 1500-020, Rev. B0. San Diego, CA, USA: Quantum Design, 2021.

[33] J. A. Weil and J. R. Bolton. *Electron Paramagnetic Resonance: Elementary Theory and Practical Applications*. 2nd ed. Hoboken, NJ: Wiley-Interscience, 2007.

[34] S. Stoll and A. Schweiger. "EasySpin, a comprehensive software package for spectral simulation and analysis in EPR". In: *Journal of Magnetic Resonance* 178.1 (2006), pp. 42–55. DOI: 10.1016/j.jmr.2005.08.013.

[35] W. Gao, Y. Zhang, D. Ramanujan, K. Ramani, Y. Chen, C. B. Williams, C. C. L. Wang, Y. C. Shin, S. Zhang, and P. D. Zavattieri. "The status, challenges, and future of additive manufacturing in engineering". In: *Computer-Aided Design* 69 (2015), pp. 65–89. DOI: 10.1016/j.cad.2015.04.001.

[36] J. Huang, Q. Qin, and J. Wang. "A Review of Stereolithography: Processes and Systems". In: *Processes* 8.9 (2020), p. 1138. DOI: 10.3390/pr8091138.

[37] E. Wang, F. Yang, X. Shen, Z. Li, X. Yang, X. Zhang, and W. Peng. "Investigation and Optimization of the Impact of Printing Orientation on Mechanical Properties of Resin Sample in the Low-Force Stereolithography Additive Manufacturing". In: *Materials* 15.19 (2022), p. 6743. DOI: 10.3390/ma15196743.

[38] Formlabs, Inc. *Standard Material Data Sheet: Materials for High-Resolution Rapid Prototyping*. Rev. 01 (18 April 2017). Formlabs. 2017.

[39] "Comparative Insights Into the Degree of Conversion of a 3D-Printed Photopolymer Resin Fabricated by Stereolithography". In: *Macromolecular Materials and Engineering* (2025). DOI: 10.1002/mame.202500185.

[40] K. Anastasiou et al. "Effect of build orientation on mechanical properties and dimensional accuracy in stereolithography". In: *Additive Manufacturing* 36 (2020), p. 101506. DOI: 10.1016/j.addma.2020.101506.

[41] T. D. Ngo, A. Kashani, G. Imbalzano, K. T. Q. Nguyen, and D.-H. Hui. "Stereolithography and other photopolymer-based additive manufacturing processes". In: *Composites Part B: Engineering* 143 (2018), pp. 172–196. DOI: 10.1016/j.compositesb.2018.02.012.

[42] M. C. Wapler, J. Leupold, I. Dragonu, D. von Elverfeld, M. Zaitsev, and U. Wallrabe. "Magnetic properties of materials for MR engineering, micro-MR and beyond". In: *Journal of Magnetic Resonance* 242 (May 2014), pp. 233–242. DOI: 10.1016/j.jmr.2014.02.005.

[43] G. Wilkinson, M. Rosenblum, M. C. Whiting, and R. B. Woodward. "The Structure of Iron Bis-Cyclopentadienyl". In: *Journal of the American Chemical Society* 74.8 (1952), pp. 2125–2126. DOI: 10.1021/ja01128a527.

[44] E. O. Fischer and W. Pfab. "Zur Kristallstruktur der Di-Cyclopentadienyl-Verbindungen des zweiwertigen Eisens, Rutheniums und Osmiums". In: *Zeitschrift für Naturforschung B* 7.7 (1952), pp. 377–379. DOI: 10.1515/znb-1952-0701.

[45] B. Štíbr. "Reactions associated with arene replacement in bis-(arene) iron complexes". In: *Journal of Organometallic Chemistry* 716 (2012), pp. 1–5. DOI: https://doi.org/10.1016/j.jorganchem.2012.05.046.

[46] O. Townrow. *Private communication*. Karlsruhe Institute of Technology. 2025.

[47] Y. Freiman and H. Jodl. "Solid oxygen". In: *Physics Reports* 401.1 (2004), pp. 1–228. DOI: https://doi.org/10.1016/j.physrep.2004.06.002.

[48] J. R. Cooper, L. Forró, and A. Jánossy. *Uncertainties in experiments on strongly-coupled vacuum field modification of superconductivity and ferromagnetism in solids*. 2023. arXiv: 2303.00090 [cond-mat.supr-con].

[49] Quantum Design. *VSM Sample Mounting Techniques*. Tech. rep. Application Note 1096-306, Rev. B1. San Diego, CA, USA: Quantum Design, 2016.

[50] R. Khatiwada, L. Dennis, R. Kendrick, M. Khosravi, M. Peters, E. Smith, and W. M. Snow. "Materials with low DC magnetic susceptibility for sensitive magnetic measurements". In: *Measurement Science and Technology* 27.2 (Dec. 2015), p. 025902. DOI: 10.1088/0957-0233/27/2/025902.

[51] F. D. Doty, G. Entzminger, and Y. A. Yang. "Magnetism in high-resolution NMR probe design. I: General methods". In: *Concepts in Magnetic Resonance* 10.3 (1998), pp. 133–156. DOI: https://doi.org/10.1002/(SICI)1099-0534(1998)10:3<133::AID-CMR1>3.0.CO;2-Y.

[52] P. T. Keyser and S. R. Jefferts. "Magnetic susceptibility of some materials used for apparatus construction (at 295 K)". In: *Review of Scientific Instruments* 60.8 (Aug. 1989), pp. 2711–2714. DOI: 10.1063/1.1140646.

[53] M. J. Coak, C. Liu, D. M. Jarvis, S. Park, M. J. Cliffe, and P. A. Goddard. "SquidLab—A user-friendly program for background subtraction and fitting of magnetization data". In: *Review of Scientific Instruments* 91.2 (Feb. 2020), p. 023901. DOI: 10.1063/1.5137820.

[54] M. Sawicki, W. Stefanowicz, and A. Ney. "Sensitive SQUID magnetometry for studying nanomagnetism". In: *Semiconductor Science and Technology* 26 (2011), p. 064006. DOI: 10.1088/0268-1242/26/6/064006.

[55] K. Gas and M. Sawicki. "In Situ Compensation Method for Precise Integral SQUID Magnetometry of Miniscule Biological, Chemical, and Powder Specimens Requiring the Use of Capsules". In: *Materials* 15.2 (2022), p. 495. DOI: 10.3390/ma15020495.

[56] G. Morrison and H.-C. zur Loye. "Simple correction for the sample shape and radial offset effects on SQUID magnetometers: Magnetic measurements on Ln2O3 (Ln=Gd, Dy, Er) standards". In: *Journal of Solid State Chemistry* 221 (2015), pp. 334–337. DOI: https://doi.org/10.1016/j.jssc.2014.10.026.

[57] Quantum Design. *Sample Mounting Considerations*. Tech. rep. Application Note 1014-201. San Diego, CA, USA: Quantum Design, 2014.

[58] P. Stamenov and J. M. D. Coey. "Sample size, position, and structure effects on magnetization measurements using second-order gradiometer pickup coils". In: *Review of Scientific Instruments* 77.1 (Jan. 2006). DOI: 10.1063/1.2149190.

[59] Quantum Design. *ACDR Option for PPMS and DynaCool: Application Note*. Tech. rep. Calibration and use of GdGG (GGG) reference sample for AC susceptibility scaling. 2020.

[60] Quantum Design. *MPMS 3 User Manual and AC Susceptibility Technical Documentation*. Definition of AC susceptibility and calibration procedures using reference samples. 2016.

[61] P. W. Selwood. "Applications of magnetochemistry to polymers and polymerization". In: *Journal of research of the National Bureau of Standards* 41 (1948), p. 151.

[62] W. M. Haynes, ed. *CRC Handbook of Chemistry and Physics*. latest edition. CRC Press, latest edition.

[63] F. A. Cotton and J. T. Mague. "The Existence of the Re_3Cl_9 Cluster in Anhydrous Rhenium(III) Chloride and Its Persistence in Solutions of Rhenium(III) Chloride". In: *Inorganic Chemistry* 3.10 (1964), pp. 1402–1407. DOI: 10.1021/ic50020a013.

[64] B. E. Bursten, F. A. Cotton, J. C. Green, E. A. Seddon, and G. G. Stanley. "Electronic Structures and Photoelectron Spectra of the Metal Atom Cluster Species Re_3Cl_9, Re_3Br_9, and $[Re_3Cl_{12}]^{3-}$". In: *Journal of the American Chemical Society* 102.3 (1980), pp. 955–968. DOI: 10.1021/ja00523a011.

[65] Quantum Design. *Calibrating the Auto-Tracking Capabilities for a Custom Sample Holder Using the MPMS3*. Application Note 1500-026 Rev. A0. Quantum Design, Dec. 2019.

Acknowledgements

I would like to express my sincere gratitude to Prof. Klingeler for the opportunity to carry out this work in his research group, and for the support and guidance throughout.

I would also like to thank Prof. Dr. Ollefs for taking the time to act as second examiner for this thesis.

I am particularly grateful to Jan Arneth and Luca Bischof for their supervision, many helpful discussions, and their patience in answering my questions throughout the course of this work.

I would also like to thank all members of the Klingeler group for the welcoming and collaborative atmosphere, and for making the time in the lab and office enjoyable.

I am grateful to my family for their support throughout my studies, and for always encouraging me to pursue my interests.

Finally, my deepest thanks go to my fiancée Mia, whose unconditional support, patience, and encouragement have been a constant source of strength throughout this work.

Declaration

I hereby declare that I have written this thesis by myself, without the use of any but the sources and materials referred to in the text.

Ich versichere, dass ich diese Arbeit selbstständig verfasst und keine anderen als die angegebenen Quellen und Hilfsmittel benutzt habe.



Heidelberg, 01.07.2026

Thomas Kerschenbauer